Ultracold molecules for the masses: evaporative cooling and magneto-optical trapping

by

B. K. Stuhl

B.A., Cornell University, 2005

M.S., University of Colorado Boulder, 2010

A thesis submitted to the

Faculty of the Graduate School of the

University of Colorado in partial fulfillment

of the requirements for the degree of

Doctor of Philosophy

Department of Physics

2012

This thesis entitled:
Ultracold molecules for the masses: evaporative cooling and magneto-optical trapping
written by B. K. Stuhl
has been approved for the Department of Physics

_____

Jun Ye

_____

Eric Cornell

Date _____

The final copy of this thesis has been examined by the signatories, and we find that both the content and the form meet acceptable presentation standards of scholarly work in the above mentioned discipline.

Stuhl, B. K. (Ph. D., Physics)

Ultracold molecules for the masses: evaporative cooling and magneto-optical trapping

Thesis directed by Prof. Adj. Jun Ye

While cold molecule experiments are rapidly moving towards their promised benefits of precision spectroscopy, controllable chemistry, and novel condensed phases, heretofore the field has been greatly limited by a lack of methods to cool and compress chemically diverse species to temperatures below ten millikelvin. While in atomic physics these needs are fulfilled by laser cooling, magneto-optical trapping, and evaporative cooling, until now none of these techniques have been applicable to molecules. In this thesis, two major breakthroughs are reported. The first is the observation of evaporative cooling in magnetically trapped hydroxyl (OH) radicals, which potentially opens a path all the way to Bose-Einstein condensation of dipolar radicals, as well as allowing cold- and ultracold-chemistry studies of fundamental reaction mechanisms. Through the combination of an extremely high gradient magnetic quadrupole trap and the use of the OH Λ-doublet transition to enable highly selective forced evaporation, cooling by an order of magnitude in temperature was achieved and yielded a final temperature no higher than 5 mK. The second breakthrough is the successful application of laser cooling and magneto-optical trapping to molecules. Motivated by a proposal in this thesis, laser cooling of molecules is now known to be technically feasible in a select but substantial pool of diatomic molecules. The demonstration of not only Doppler cooling but also two-dimensional magneto-optical trapping in yttrium (II) oxide, YO, is expected to enable rapid growth in the availability of ultracold molecules—just as the invention of the atomic magneto-optical trap stimulated atomic physics twenty-five years ago.

to Deena

Acknowledgements

A doctoral degree is a long process, and is always a team effort. I want to thank Jun Ye for accepting me into his group: it's a great set of people, and I've had a lot of fun doing great science with all of you. I especially want to thank Brian Sawyer for his years of leadership on the collision experiments and for passing on his intuition for the machine he helped build. I also overlapped briefly with Eric Hudson and Benjamin Lev, who both helped at the very beginning to introduce me to the world of dipolar molecules.

More recently, I have had the pleasure of working with Mark Yeo, Matt Hummon, and Alejandra Collopy — and just this year, Hao Wu and David Reens. Mark has been here almost as long as I have, and he is a true lasers man: the YO laser-cooling experiment would not have gotten anywhere without him. Matt's leadership of the laser-cooling experiment has been exemplary, and I have been delighted to see my dream from 2008 be demonstrated under his watch. Alejandra has grown into a strong team member on YO in only a year, and I am sure that Hao and David will rapidly do the same as they take over the OH experiment.

Over the years, we have shared a very fruitful collaboration with the theory group of John Bohn. In particular, his former student Ed Meyer was an invaluable resource on molecular structure calculations, and his recently departed postdoc Goulven Quéméner's calculations of OH–OH scattering cross-sections were a major motivation in our undertaking the evaporative cooling experiment.

Our ability to perform experimental science at JILA is also strongly supported by the excellent technical staff, in both the instrument and electronics shops. I particularly want to thank Terry Brown and Carl Sauer in the electronics shop for their guidance in analog electronics and the vagaries of extremely high voltages, and Hans Green, Tracy Keep, and Todd Asnicar in the instrument shop for always having time to answer my design and machining questions.

Beyond JILA, I want to thank several people for their support during the many-year project that is a doctorate.

I want to thank my parents Sheila Kojm and Louis Stuhl for their encouragement of my love of science from a young age and for their more focused encouragement in recent years, even when laboratory progress seemed to be going backwards. Most of all, I want to thank my wife Deena Rosenberg for her love, her support, and her tolerance of the trials of being married to a graduate student!

Contents

List of Tables

Table

List of Figures

Figure

Symbols used

Roman Symbols

CP	charge-parity symmetry, that a system is invariant if the charges of all the particles are reversed and the system is put through an inversion transformation
PMT	photo-multiplier tube
Z	atomic number

Fundamental Constants

α	the fine structure constant, numerically $\sim 1/137$
c	the speed of light in a vacuum, 299 792 458 m/s
D	the Debye, a unit of electric dipole moment equal to 3.336×10^{-30} C·m
e	the charge of an electron, 1.602×10^{-19} C
k_B	Boltzmann's constant, 1.38×10^{-23} J/K
m_e	the mass of the electron, 9.109×10^{-31} kg
m_p	the mass of the proton, 1.673×10^{-27} kg
μ_B	the Bohr magneton, 9.274×10^{-24} J/T
μ_N	the nuclear magneton, 5.05×10^{-27} J/T

Angular Momenta

F total angular momentum vector (including rotational and nuclear angular momenta), with quantum number F and projection M_F

G coupled nuclear and electronic spin angular momentum vectors, with quantum number G and projection M_G

I nuclear spin angular momentum vector, with quantum number I and projection M_I

J total electronic angular momentum vector, with quantum number J and projection M

K the projection of **J** along the molecular symmetry axis in a symmetric top molecule

L total electronic orbital angular momentum vector, with quantum number L and projection Λ on the internuclear axis

N molecular total angular momentum minus electron spin vector, with quantum number N and projection M_N

R molecular rotational angular momentum vector, with quantum number R and projection M_R (for molecules with $\mathbf{L} = \mathbf{0}$, **R** and **N** are equivalent)

S total spin angular momentum vector, with quantum number S and projection Σ on the internuclear axis

Molecular Constants

A the spin-orbit splitting constant

B rotational constant

D quadratic rotational constant

d the total electric dipole moment of a molecule

m the molecular mass

ω_e equilibrium vibrational constant

$\omega_e x_e$ quadratic vibrational constant

Assorted Symbols

$\mathscr{H}$ a Hamiltonian

φ decelerator phase angle

Chapter 1

Introduction

1.1 Motivation

The current excitement over cold molecules is, in many ways, the natural progression from the past twenty-five years of cold atom physics. Just as the development of first Doppler cooling[1, 2] and then magneto-optical trapping[3] led to such diverse results as Bose-Einstein condensation[4, 5], exploration of the BEC-BCS crossover regime in degenerate Fermi gases[6, 7, 8, 9], the creation of strongly-coupled atom-cavity quantum optical systems[10, 11], measurements of parity non-conservation in Cs and its nuclear anapole moment[12, 13], and optical clocks[14, 15, 16, 17, 18, 19], so too are cooled molecular species expected to enable a new set of experimental frontiers. This section describes some of the major arenas which cold molecules are making possible.

In molecular physics, again as in atomic physics, experiments of interest can be loosely divided into two categories: those which care about the specific (chemical, isotopic, mass, etc.) nature of the particle under study, and those which do not. The former encompasses both the obvious studies of chemical or nuclear properties, but also — especially in molecules — those where some detail of the particle's specific structure enables or enhances the experiment. One example from atomic physics is the Cs anapole experiment, where the high Z number of Cs enhances the spectroscopic couplings[12] over the lighter alkali-metals. Another example is alkaline-earth optical clock experiments: here it is the electronic and hyperfine structure of the species which creates the clock transition, and there are great differences in character between the clock transitions in Sr[14, 17], Al^+[18, 19], and Yb[15, 16]. By contrast, there are also a great many experiments which could in principle be done with any atom providing a reasonable approximation of a generic two- or three-level system. While alkali metals, especially Rb, are commonly

used for these experiments, it is a choice of convenience rather than necessity. Some atomic examples of the latter category include strong-coupling experiments, electromagnetically-induced transparency (EIT) demonstrations, and vapor-cell squeezed light tests.

Chemical studies of atomic gases, however, face a profound limitation: two-body collisions of isolated atoms cannot undergo chemistry. Conservation of momentum requires a third partner in the interaction, and even then the only possible reaction is recombination (A + B + M $\rightarrow$ AB + M). (M is usually another atom, although a photon can also serve in excited-state collisions.) Molecules, by contrast, can undergo exchange (2AB $\rightarrow$ A_2 + B_2), abstraction (2AB $\rightarrow$ A_2B + B), or dissociation (2AB $\rightarrow$ AB + A + B) interactions in a simple two-body collision. Study of bond **breaking** as well as formation requires molecules. The first major motivation for cooling molecules is therefore chemistry: cold systems are clean (and more easily calculable) systems. Moreover, electric dipole moments, as well as possibly Feshbach resonances, enable **control** of the intermolecular potential surface and therefore control of chemistry as well — if the sample is cold enough that thermal averaging does not wash out the induced perturbation of the potential surface. One example of a possible route to electric-field-based control of chemistry can be seen in the abstraction reaction OH + H_2CO $\rightarrow$ H_2O + HCO [20], as illustrated in figure 1.1. The application of a static electric field opposes the relative reorientation required to form the reaction's transition state, and therefore enables control of the reaction rate. Another reaction which might be field-controllable is 2OH $\rightarrow$ H_2O + O. In this case the mechanism would be more subtle and is discussed in chapter 6. More generally, since electric fields couple together all states of opposite parity, including those of differing electronic configurations, they may be capable of controlling not only external chemical interactions, but even internal dynamics like conical intersections[21] and spin-dependent chemistry [22].

Beyond direct chemical studies of a molecular sample, there are many other experiments which require a specific species. One of the most well-known is the search for the electron's theoretical electric dipole moments (the *e*-EDM). Even in the Standard Model of particle physics, the fact that weak interactions do not preserve charge-parity (*CP*) symmetry means that the electron's charge distribution is not precisely spherical: it has a nonzero electric dipole moment. Extensions to the Standard Model, including both supersymmetric theories and technicolor, in general imply a much larger and potentially experimentally observable *e*-EDM.

Of course, since the electron itself is charged, it is impossible to simply hold it still, apply an electric field,

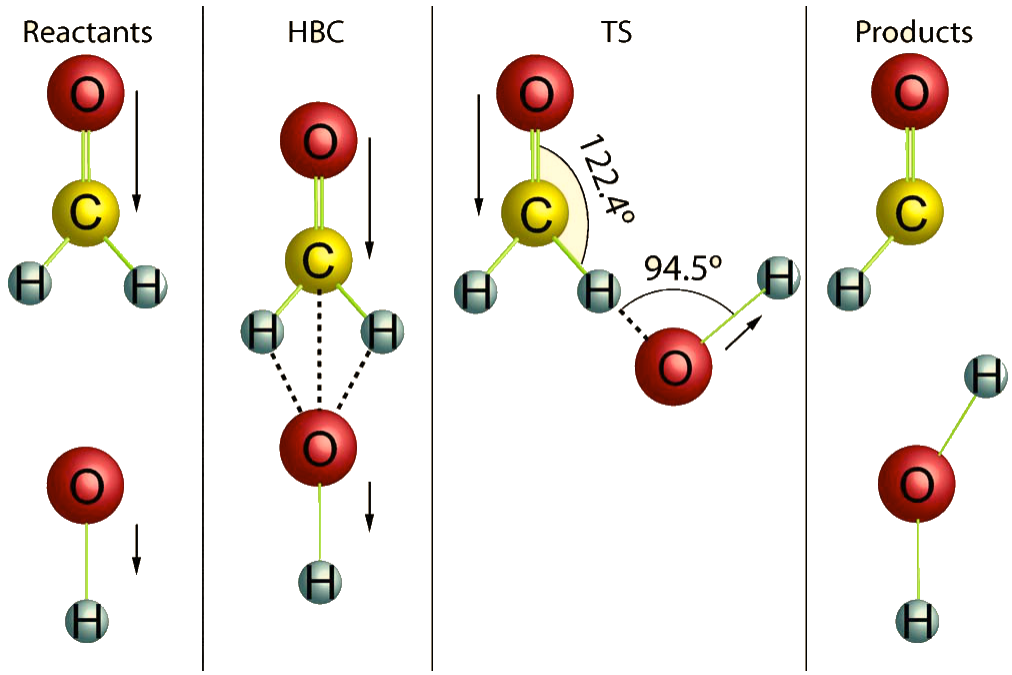

Figure 1.1: **Electrostatic control of chemistry in the OH–H_2CO hydrogen abstraction reaction.** In order for the reaction to proceed, the reactants must align to form the transition state **TS**. This state has the two molecular dipole moments (indicated by the arrows in the diagram) at an angle of greater than 90°. In the presence of a polarizing electric field, this orientation is disfavored by the Stark shift of the OH molecule as it attempts to anti-align to the electric field. As the reaction may be otherwise barrierless, even small changes in the energy cost of state **TS** could enable large changes in the ultracold reaction rate. Figure reproduced from [20].

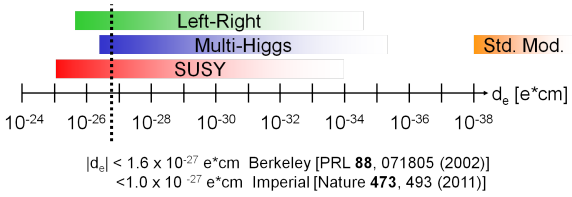

Figure 1.2: **Comparison of the theoretically predicted versus experimentally testable ranges of the e-EDM .** (Courtesy of D. Gresh.)

and look for a change in the spin-flip transition frequency. Instead, one must probe an electron confined to a neutral system, an atom or a molecule. Until less than two years ago, the best limit on the e-EDM was set by an experiment done in atomic Tl[23]. Now, however, an experiment in a warm YbF beam[24] has beat that limit by a factor of two. Moreover, in the coming years, several experiments in ThO[25], HfF^+[26], WC[27], and YbF are expected to improve the detection sensitivity by over an order of magnitude and directly probe e-EDMs of the size predicted by supersymmetry.

This vast improvement in sensitivity is due entirely to using molecules rather than atoms as the test systems. Specifically, by using polar molecules with a high-Z atom, polarizing the molecule in the laboratory from also applies an enormous (tens of GV/cm, far larger than the hundreds of kV/cm directly achievable in the lab) effective electric field to a valence electron. Moreover, a careful choice of electronic state provides direct cancellation of some of the most important sources of systematic errors.

Another area where molecules can provide much higher sensitivity than atoms lies in tests of fundamental constants. Some theories of cosmic inflation, for instance, suggest that the fine-structure constant α or the proton-to-electron mass ratio m_p/m_e might vary in time or space. The Λ-doublet transition of the OH radical provides strong rejection of systematic errors in cosmological hunts for $\dot{\alpha}$, since the main ($\Delta F = 0$) and satellite ($\Delta F = \pm 1$) line transition frequencies have very different dependencies on α[28, 29]. This means that observers can use one set of lines to determine the red-shift (i. e., the distance) to an astrophysical source, and then use the other set to determine the value of α when the source emitted the radiation. Since OH Λ-doublet lines are radiated by OH mega-masers[30, 31], there are very bright sources available at substantial red-shifts.

Alongside $\dot{\alpha}$, molecular vibrations enable very direct time-constancy tests for m_e/m_p. A simple long-term comparison of an atomic optical clock (whose frequency, being an electronic transition, depends mostly on α) with a molecular vibrational clock allows testing the stability of both α and m_e/m_p. While molecular vibrational spectroscopy does not intrinsically require **cold** molecules, it is only the advent of optical lattice-based atomic clocks which has provided sufficiently high precision to make the atomic side of such a comparison feasible, and so some similarly low temperature is needed for the molecular side as well.

A final area of measurement enabled by molecules is the nuclear weak charge or anapole moments of a substantial breadth of elements. While the anapole moment of Cs was measured directly, no other atom has been so

measured: it was only the extreme sensitivity of the parity non-conservation measurement in laser-cooled Cs which enabled its detection. However, the availability of closely-spaced, opposite-parity levels in dipolar molecules is expected to greatly enhance the sensitivity of these measurements[32]. A reasonably diverse set of anapole moment measurements would provide a much-needed test of nuclear structure theories.

Parallel to the chemical nature of molecules, there is also great interest in them as approximately "atoms with an electric dipole moment." While atom-atom interactions are almost purely isotropic, the dipole moment's intrinsic p-wave character[33, 34, 35] is expected to create fascinating and in some cases entirely novel phases of matter[36, 37, 38, 39] like the so-called "checkerboard lattice" [40, 41], as well as potentially never-before-seen Cooper-pairing symmetries in fermionic species[42]. Atoms, of course, may have magnetic dipole moments, but these moments are relatively weak compared to molecular electric dipole moments. For scale, the interaction energy (which scales as μ^2/r^3 for a generic dipole moment μ and distance r) is roughly 1000X stronger for a 1 D electric dipole moment than for a 1 μ_B magnetic moment at a given distance r. Atomic magnetic dipole moments max out at $10\mu_B$ (in Tb and Dy), while molecular electric dipole moments go up to roughly 10 D. Moreover, the atomic magnetic moment is **fixed**, while the molecular electric moment can be tuned by an externally applied field. While the molecular moment is generally referred to as "permanent," molecules in the absence of an electric field are in eigenstates of parity and therefore have zero net electric dipole moment. Application of a field of increasing strength mixes molecular states of opposite parity to reveal more and more of the full dipole moment. Varying the electric field strength thus tunes the dipole moment.

The dipole moment's strength and tunability also have led to suggestions of using molecules as qubits in quantum information applications. Dipole-dipole collisions provide a long-range way of coupling qubit-molecules, while a spatially-varying Stark shift enables spectroscopic addressing of individual qubits[43].

Given all these exciting applications for cold molecules, why does the field seem to be roughly twenty years behind its atomic analogue? While it may seem a touch glib to say, the truth is just that molecules really are that much harder to work with. Until roughly a decade ago, the coldest molecules available were limited by the reach of cryogenic helium dilution refrigerators — many orders of magnitude hotter than laser-cooled atoms. This thesis is primarily about several breakthroughs in applying cold atom techniques to molecules.

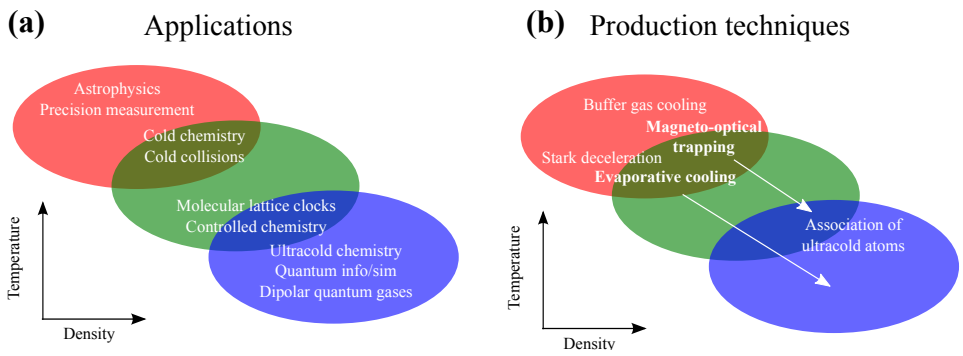

Figure 1.3: **Temperature and density ranges relevant to cold and ultracold molecule experiments.** The *x*-axes are density in a loosely logarithmic scale from 10^4 cm^{-3} to 10^{13} cm^{-3} and the *y*-axes are temperature in a similar scale from 10 K at the top to 1 nK at the bottom. (a) Temperatures and densities necessary for some of the experiments discussed in section §1.1. (b) Temperatures and densities available from the major known techniques to produce cold and ultracold molecules. Until the developments of molecular laser cooling and evaporative cooling (described in part in this thesis) there were no techniques available to bridge the green region and thereby produce chemically diverse ultracold molecules: as of this writing, RbK remains the only heteronuclear molecule available at high densities from ultracold atomic association techniques.

1.2 History

When I first joined the group of Jun Ye in early 2006, cold molecules still felt like a backwater within AMO physics, and Stark deceleration in particular still had an air of novelty to it. At that point, there were only a handful of techniques known for producing molecular gases at temperatures below 4 K, and only two of them (Stark deceleration and buffer-gas cooling) had demonstrated any reasonable final density of cold molecules. While the concept of Stark deceleration was proposed over forty-five years before[44, 45], the first functioning demonstration had only been made in 1999[46]. As far as I know, in 2006 there were only two labs in the whole world with operational decelerators[46, 47, 48]. The Ye group had two: the original machine was being used to finish a precision spectroscopy project on the OH Λ-doublet line[28, 29], while the second had recently demonstrated slowing of formaldehyde[20] and was currently working on a detailed study of deceleration dynamics[49] in preparation for a drive towards magnetic trapping of OH molecules. (The first trapping experiments are discussed more fully in chapter 4.)

Since then, working with molecules has become much less fringe, if not yet truly mainstream. The availability of near-quantum-degenerate dipolar RbK molecules[50, 51] made it clear that there was hope for experimental tests of dipolar Fermi gas and lattice physics. Our proposal for the practical laser cooling of selected molecules (chapter 8) has been demonstrated in SrF[52] at Yale and in YO in this group[53]. Most recently, we have observed evaporative

cooling of magnetically trapped OH molecules. Since evaporation is the single technique which enabled BEC in atomic systems, its availability in molecules is potentially revolutionary. At a broader level, many more groups around the world have taken up molecule projects since 2006, and our sessions at the annual Division of Atomic, Molecular, and Optical Physics conference are now much better attended!

1.3 Side note: on moving an experiment

The work described in this thesis also faced an additional complication: the entire experiment was moved in January 2012 from its original location in JILA S-1B05 (now the corridor connecting the S- and X-wings) to X-1B10. While the hiatus this imposed was not appreciated, the move did have its positive points. The new space in X-1B10 is a substantial improvement over the old lab: it has more **space** in general, more storage space in particular, and the X-wing service corridor is a great thing. Moreover, the move offered an opportunity to finally correct some long-standing defects in the experimental layout.

The Stark decelerator is not a small system: the vacuum chamber is roughly 1.5 m long and over 1 m wide (at its widest point); it also has no less than five turbomolecular pumps on it, plus the rough vacuum system backing those pumps. In S-1B05, the entire system was installed sitting on the optics table. While this made optical access simple, it also ruined both the vibration and electrical properties of the table for anything else. The turbopumps drive high-frequency vibrations, and the decelerator switches tens of kilovolts at roughly ten kilohertz; the switching drives enough electronic noise onto the high-voltage ground as to contaminate any nearby signals. (To combat this noise, all sensitive cables are shielded by an extra electrically-isolated layer of ground braid.)

When the experiment was moved to X-1B10, several changes were made. The first is that the decelerator is now mounted on a free-standing support frame. This both eliminates the coupling of turbopump vibration to the optical table and also vastly improves access to the side of the decelerator facing the optics table. (When the decelerator was on the table, it was an exercise in contortionism to access the rough vacuum lines and the feed-throughs for the negative polarity decelerator rods, but no longer!) In combination with the mechanical decoupling, the control system was audited for connections between the decelerator's high-voltage ground and the controls' signal grounds. By isolating the two, the experiment is now able to take advantage of the star-ground system built into the X-wing. The high-voltage ground is tied to one of the building star-ground panels, while the general signal ground is tied to

a different panel. Putting the two grounds on different branches of the star has vastly reduced the pickup from the decelerator switching.

Another area in which the setup in X-1B10 is a major improvement is cable routing. Cable (and in many labs, optical) routing is the bane of any lab's existence: cables are added for "a quick test" and never removed; a new instrument needs a connection, and it is added by the path that the cable will **reach**, rather than a path that is reasonably unobstructing. In the X-wing, we have made an investment for the future: we installed a set of proper cable trays and arranged a reasonable routing of all of the signals needed to run the current experiment. At least for now, the clutter is contained.

The new space is not an unblemished improvement, however: there were and are some "teething troubles." The most egregious problem was definitely the chilled-water system incidents. While the exact details will never be known, Facilities Management somehow managed to sufficiently overpressure the system as to mechanically break things – twice! Most likely, they accidentally induced a water hammer effect while adjusting valves and pumps. The temperature stability of the labs has for the most part been excellent, but there remains some work to be done to smooth out the switch-over between building heating and cooling in the spring and fall.

Chapter 2

Background

2.1 Molecular structure

The pioneering atomic physicist Arthur Schalow once defined a diatomic molecule as being a molecule with one atom too many. To a person who is used to the simple, discrete spectra of isolated atoms, this may be true. Both the richness and the difficulties of molecular physics arise from the distributed nature of molecules. Even if one thinks of a diatomic molecule as simply two atoms magically held on opposite ends of a stick, it is immediately obvious that there is now a rotational degree of freedom which neither atom posessed separately. Taking the model one step closer to reality, by changing the stick into a spring with a finite elastic modulus, makes a vibrational mode evident. The recognition that the equilibrium length and spring constant of the interatomic bond is set by the electronic configuration of the system makes it clear that electronic transitions can change the rotational and vibrational state of a molecule as well; such transitions are referred to as **rovibronic**.

At the most rigorous level, molecular structure requires the full power of quantum field theory, as electrons may acquire relativisitic speeds near high-Z nuclei[54]. However, in the context of this thesis, several major simplifications may be made. The first is that for relatively light nuclei relativistic effects can be treated perturbatively, adding the electronic and nuclear spins and their couplings to each other and to the motion-generated currents to the effective Hamiltonian by hand. This simplifies the problem to a form

$$\mathscr{H}_{\text{molecule}} = \sum_{\text{nuclei}} \frac{1}{2m_i}\left(\hat{p}_i + \frac{e}{c}\hat{A}\right)^2 + \sum_{\text{electrons}} \frac{1}{2m_e}\left(\hat{p}_i - \frac{e}{c}\hat{A}\right)^2 + \mathscr{H}_{\text{relativistic}}$$

where $\hat{p}_i$ is the momentum operator of the i'th particle and $\hat{A}$ is the electromagnetic vector potential operator. A further vast simplification comes from the Born-Oppenheimer approximation, in which it is assumed that the electronic and

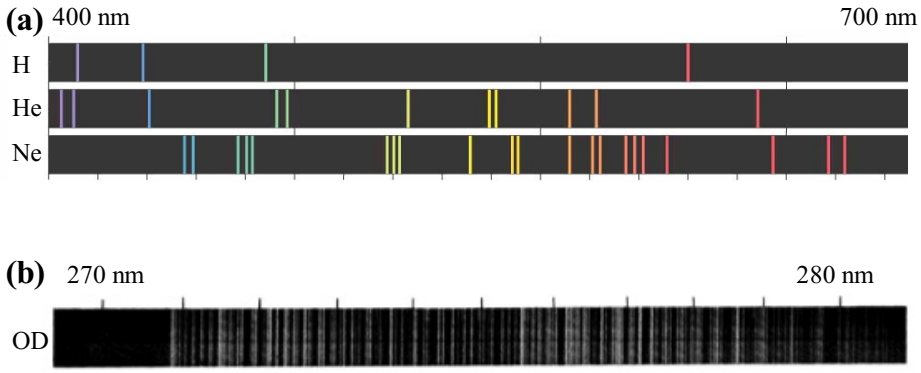

Figure 2.1: **A comparison of atomic line spectra versus molecular band structures.** (a) Atomic spectra of H, He, and Ne. (b) One vibronic band in the spectrum of OD. Note the difference in wavelength scales between (a) and (b).

nuclear parts of the wavefunction are separable,

$$|\Psi_{\text{molecule}}\rangle = |\Phi_{\text{nuclear}}\rangle \otimes |\Psi_{\text{electronic}}\rangle$$

, and moreover that the electronic wavefunction depends only on the positions of the nuclei. This results in the nuclear part acquiring an effective internuclear potential, while the electronic part consists of discrete configurations which each yield a **different** internuclear potential. Separation of the nuclear motion into components parallel and perpendicular to the internuclear axis then yields an approximate Hamiltonian

$$\mathscr{H}_{\text{molecule}} \approx \mathscr{H}_{\text{elec}} + \mathscr{H}_{\text{vib}} + \mathscr{H}_{\text{rot}}$$

where the electron terms and relativistic corrections have been combined into the effective electronic Hamiltonian $\mathscr{H}_{\text{elec}}$.

To first order, $\mathscr{H}_{\text{vib}}$ and $\mathscr{H}_{\text{rot}}$ are both conceptually simple:

$$\mathscr{H}^0_{\text{vib}} = \frac{1}{2}k\hat{r}^2 = \omega_e\left(v+\frac{1}{2}\right)$$
$$\mathscr{H}^0_{\text{rot}} = \frac{1}{2\mathscr{I}}\hbar^2\mathbf{N}^2 = BN(N+1)$$

. $\mathscr{H}_{\text{vib}}$ is a harmonic oscillator, where k is the effective spring constant due to the electronic configuration and $\hat{r}$ is the radial position operator; $\mathscr{H}_{\text{rot}}$ is the rotation perpendicular to the internuclear axis with an effective moment of inertia $\mathscr{I}$. By convention, molecular theory and spectroscopy work with the simplified parameters

$$\omega_e = \frac{1}{hc}\cdot\hbar\sqrt{\frac{k}{m_{\text{red}}}}$$
$$B = \frac{1}{hc}\cdot\frac{\hbar^2}{2\mathscr{I}}$$

which are generally reported in cm^{-1}. Of course; the parallel and perpendicular motions are not truly separable: B may be perturbatively expanded in powers of $\left(v+\frac{1}{2}\right)$ to account for the change in mean bond length with increasing vibrational excitation; there also exist higher order terms like

$$\mathscr{H}^1_{\text{vib}} = -\omega_e x_e\left(v+\frac{1}{2}\right)^2$$
$$\mathscr{H}^1_{\text{rot}} = -D\left[N(N+1)\right]^2$$

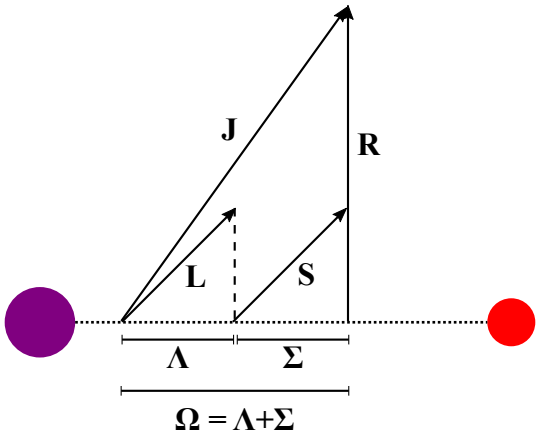

Figure 2.2: **Vector diagram for Hund's case *a*.** The electronic spin and orbital angular momenta, **S** and **L**, are strongly coupled to the internuclear axis by spin-orbit and electrostatic interactions respectively. Their projections along the internuclear axis, Σ and Λ, couple to form Ω which is the projection of the total angular momentum $\mathbf{J} = \mathbf{R} + \Omega$.

to account for the anharmonicity in the molecular potential. With sufficient signal-to-noise ration, molecular spectra may be fitted with coefficients out to third or fourth order in powers of $\left(v+\frac{1}{2}\right)$, $J(J+1)$, or a mix of the two. However, that level of spectroscopic detail is only relevant when attempting to describe the structure of an entire set of molecular bands. For the purposes of this work, it suffices to know the positions of only a few low-J, low-v states in any given molecule, and therefore the second-order expansions are more than sufficient.

2.2 Angular momenta and Hund's cases

While the previous section treated the rotation of the molecule as though it were the only source of angular momentum in the system, for general molecules that is untrue. Molecules may posess net electronic orbital angular momentum **L**, net electron spin **S**, and nuclear spin **I** as well as rotational angular momentum. Since all of these angular momenta posess magnetic moments, they all can interact. The relative strength of the various couplings lead to several qualitatitively distinct spectral forms, known as the five **Hund's cases**[55, 56]. Each case is characterized by a specific hierarchy of levels (e. g. many rotational levels within an apparent spin-orbit manifold for case *a*); the rotational Hamiltonian has a different natural expression in each case.

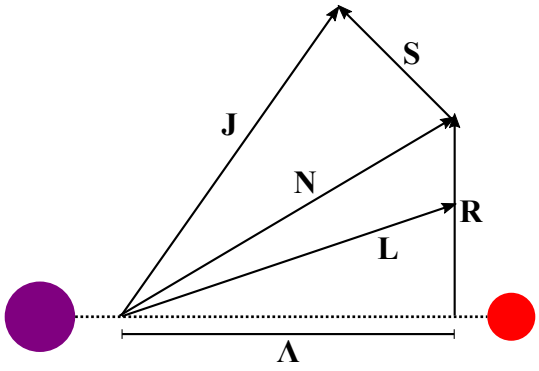

Figure 2.3: **Vector diagram for Hund's case *b*.** The electronic spin **S** has weak or zero coupling to the internucear axis; it instead couples to the intermediate vector $\mathbf{N} = \mathbf{R} + \mathbf{L}$ to form **J**, where **R** is the rotational angular momentum. If $\mathbf{L} = \mathbf{0}$, **N** and **R** are equivalent.

2.2.1 Hund's case *a*

Case *a* (figure 2.2) occurs when spin-orbit interactions are much weaker than the electrostatic interactions which split different electronic states, but are much stronger than the spin-rotation or orbit-rotation interactions, that is when $E_{\text{elec}} \gg A\Lambda \gg BJ$. This results in a hierarchy where widely-separated electronic levels are split into a set of spin-orbit manifolds, each of which contains many closely-spaced rotational levels. This commonly occurs in molecules with relatively low Z and non-zero electronic angular momentum. The natural expression of the rotational Hamiltonian is

$$\mathscr{H}^0_{\text{rot}} = B(R)\,(\mathbf{J} - \mathbf{L} - \mathbf{S})^2$$

where $B(R)$ emphasizes the dependance of B on the internuclear spacing. This form makes it clear that **N** is not a good quantum number in this case.

2.2.2 Hund's case *b*

If the spin-orbit coupling is weak or nonexistant (most commonly, $\mathbf{L} = 0$ for close-shell molecules), low-Z molecules are generally in case *b*. In this case (figure 2.3), electronic levels directly contain a manifold of rotational levels, each of which may be broken into a small spin-orbit multiplet. The rotational Hamiltonian

$$\mathscr{H}_{\text{rot}} = B(R)\,(\mathbf{N} - \mathbf{L})^2$$

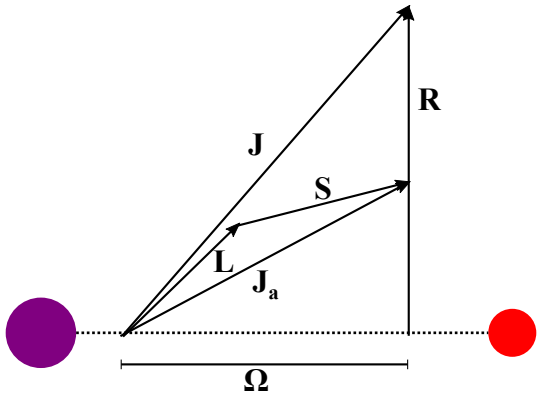

Figure 2.4: **Vector diagram for Hund's case *c*.** Neither **L** nor **S** are coupled to the internuclear axis, but spin-orbit interactions couple the two together to form the total spin-orbit angular momentum $\mathbf{J_a}$ with projection Ω along the internuclear axis. $\mathbf{J_a}$ couples with the rotational angular momentum **R** to form **J**.

has a simple first-order form if orbit-rotation couplings are ignored:

$$\mathscr{H}_{\rm rot} = B(R)\left[N(N+1) - \Lambda^2\right]$$

. Case *b* is appropriate when $E_{\rm elec} \gg BJ \gg A\Lambda$.

2.2.3 Hund's case *c*

The last common case for non-Rydberg molecules is case *c*, which occurs in molecules with high-*Z* nuclei and is an analog to *jj*-coupling in atomic spectra[57]. In this case, the spin-orbit interactions are sufficiently strong as to necessitate their incorporation into $\mathscr{H}_{\rm elec}$, and neither **L** nor **S** are well-defined (figure 2.4). Instead, there occur electronic levels (which now fully include the spin-orbit character of the level, rather than forming a multiplet as in case *a*) with well-defined total electronic angular momentum $\mathbf{J}_a$ and its projection along the internuclear axis Ω. The rotational Hamiltonian in this case is similar to that of case *a*,

$$\begin{aligned}\mathscr{H}^0_{\rm rot} &= B(R)\left(\mathbf{J}-\mathbf{L}-\mathbf{S}\right)^2 \\ &= B(R)\left[\mathbf{J}^2 - 2\mathbf{J}\cdot\mathbf{J}_a + \mathbf{J}_a^2\right]\end{aligned}$$

where the $\mathbf{J}\cdot\mathbf{J}_a$ term couples together states of different electronic configurations and $\Delta\Omega = 1$. This case is appropriate for $A\Lambda \gtrapprox E_{\rm elec} \gg BJ$.

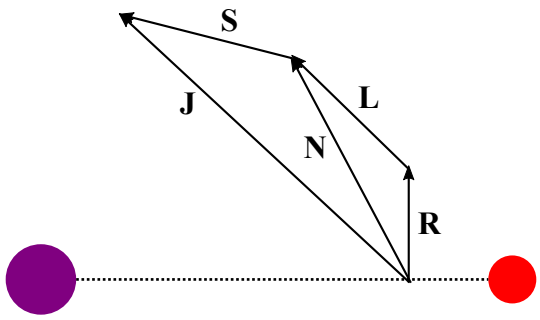

Figure 2.5: **Vector diagram for Hund's case *d*. L** is more strongly coupled to the rotation **R** than to **S**, and so forms the intermediate vector **N**. **N** then couples to the spin **S** to form **J**.

2.2.4 Hund's cases *d* and *e*

Cases *d* and *e* (figures 2.5 and 2.6) are much less common—in fact, they almost never occur outside of Rydberg systems, where the valence electron is almost completely decoupled from the ion core[56]. Case *d* is an analog to case *b*, where spin-orbit coupling is weak but the rotational splitting is much larger than the splittings between adjaced Rydberg levels—that is, $BJ \gg E_{\text{elec}}$. Case *e* is analagous to case *c*, where the spin-orbit couplings are stronger than the electrostatic level splittings, and so the effective hierarchy is $A\Lambda \gg BJ \gg E_{\text{elec}}$. (Note that Λ is not a good quantum number in case *e*, merely a statement that there is nonzero spin-orbit coupling.)

2.3 Molecules in external fields: Stark and Zeeman effects

In general, the interaction between a dipole moment $\vec{\mu}$ and an external field $\vec{\mathscr{F}}$ generates interaction matrix elements of the form $\mathscr{H}_i = -\vec{\mu} \cdot \vec{\mathscr{F}}$ (where $\vec{\mathscr{F}}$ represents either a magnetic field $\vec{B}$ or an electric field $\vec{E}$). In order to evaluate these moments it may be necessary to transform between the molecule-fixed frame in which the appropriate dipole moment $\vec{\mu}$ is defined and the laboratory frame in which $\vec{\mathscr{F}}$ is defined. The correct form for this transformation depends on the Hund's case character of the molecule in question. For instance, in ground-state OH, both the electric and magnetic dipole moments are approximately constrained to follow the internuclear axis in a Hund's case *a* configuration, at least for very low J. By contrast, ground-state YO has a $\Lambda = 0$ and therefore case *b* structure. This means that the magnetic moment due to the coupled electron and nuclear spins is free to align directly in the laboratory frame and therefore YO's magnetic moment does not require any coordinate transformation.

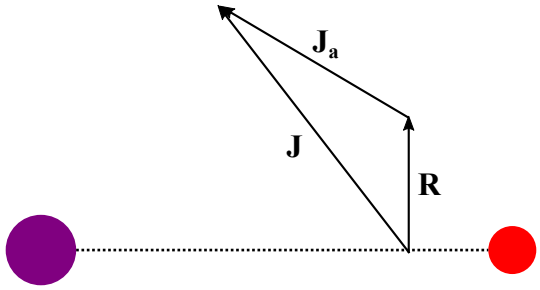

Figure 2.6: **Vector diagram for Hund's case *e*. L** and **S** are very strongly mixed to from $\mathbf{J_a}$which is coupled to the rotation **R** to form **J**.

For molecules which require transformations, we follow Lara et al. [58] and use the Wigner rotation matrix elements[59] $\mathscr{D}^{1*}_{qk}(\omega)$ to write

$$\mathscr{H}_i = -\vec{\mu}\cdot\vec{\mathscr{F}} = -\sum_q (-1)^q \left(\sum_k \mathscr{D}^{1*}_{qk}(\omega)\,\mu_k\right)\mathscr{F}_{-q}.$$

While OH is not fully a Hund's case *a* molecule, its $J=\frac{3}{2}$ state is nonetheless close enough that both the electric and magnetic dipole moments may be considered to lie along the internuclear axis and so H_i simplifies to

$$\mathscr{H}_i = -\sum_q (-1)^q\,\mathscr{D}^{1*}_{q0}(\omega)\,\mu_{k=0}\mathscr{F}_{-q}.$$

If $\vec{B}$ and $\vec{E}$ are not parallel, it is further necessary to rotate the laboratory fields to a combined frame. Without loss of generality, we take the laboratory Z axis to be along $\vec{B}$ and transform $\vec{E}$ using the reduced rotation matrix elements $d^{1*}_{qk}(\theta_{EB})$ to write

$$\mathscr{H}_i = -\mathscr{D}^{1*}_{00}(\omega)\,\mu^{(B)}_{k=0}|B| - \sum_q \mathscr{D}^{1*}_{q0}(\omega)\,\mu^{(E)}_{k=0} d^{1*}_{-q0}(\theta_{EB})\,|E|\,.$$

Using Lara et al.'s results for the $\left|JM\bar{\Omega}\varepsilon\right\rangle$ parity basis yields the matrix elements

$$\begin{aligned}\left\langle JM\bar{\Omega}\varepsilon\right|\mathscr{H}_i\left|J'M'\bar{\Omega}'\varepsilon'\right\rangle &= \sqrt{2J+1}\sqrt{2J'+1}\begin{pmatrix} J & 1 & J' \\ -\bar{\Omega} & 0 & \bar{\Omega}' \end{pmatrix}(-1)^{M-\bar{\Omega}} \\ &\times\left\{\left(\frac{1+\varepsilon\varepsilon'(-1)^{J+J'+2\bar{\Omega}}}{2}\right)\begin{pmatrix} J & 1 & J' \\ -M & 0 & M' \end{pmatrix}\mu_B B(\Lambda+g_e\Sigma)\right. \\ &\left.+\left(\frac{1-\varepsilon\varepsilon'(-1)^{J+J'+2\bar{\Omega}}}{2}\right)\sum_q\begin{pmatrix} J & 1 & J' \\ -M & q & M' \end{pmatrix}d^{1*}_{-q0}(\theta_{EB})\mu_e E\right\}\end{aligned}$$

where g_e is the electron Landé g-factor and μ_e is the molecular electric dipole moment.

Evaluating the matrix elements described previously for the OH $\left|J=\frac{3}{2},M,\bar{\Omega}=\frac{3}{2},\varepsilon\right\rangle$ ground state manifold yields an 8×8 matrix which can be diagonalized to find the Stark-Zeeman spectrum of OH for an combination of fields sufficiently large that hyperfine structure does not appreciably contribute. From left-to-right and top-to-bottom, the state ordering used to defined the matrix begins with $\left|e;-\frac{3}{2}\right\rangle$ and increases first M and then ε:

$$\begin{pmatrix}
-\frac{\Delta}{2}-\frac{6}{5}\mu_B B & 0 & 0 & 0 & \frac{3}{5}\mu_e E\cos\theta_{EB} & -\frac{\sqrt{3}}{5}\mu_e E\sin\theta_{EB} & 0 & 0 \\
0 & -\frac{\Delta}{2}-\frac{2}{5}\mu_B B & 0 & 0 & -\frac{\sqrt{3}}{5}\mu_e E\sin\theta_{EB} & \frac{1}{5}\mu_e E\cos\theta_{EB} & -\frac{2}{5}\mu_e E\sin\theta_{EB} & 0 \\
0 & 0 & -\frac{\Delta}{2}+\frac{2}{5}\mu_B B & 0 & 0 & -\frac{2}{5}\mu_e E\sin\theta_{EB} & -\frac{1}{5}\mu_e E\cos\theta_{EB} & -\frac{\sqrt{3}}{5}\mu_e E\sin\theta_{EB} \\
0 & 0 & 0 & -\frac{\Delta}{2}+\frac{6}{5}\mu_B B & 0 & 0 & -\frac{\sqrt{3}}{5}\mu_e E\sin\theta_{EB} & -\frac{3}{5}\mu_e E\cos\theta_{EB} \\
\frac{3}{5}\mu_e E\cos\theta_{EB} & -\frac{\sqrt{3}}{5}\mu_e E\sin\theta_{EB} & 0 & 0 & \frac{\Delta}{2}-\frac{6}{5}\mu_B B & 0 & 0 & 0 \\
-\frac{\sqrt{3}}{5}\mu_e E\sin\theta_{EB} & \frac{1}{5}\mu_e E\cos\theta_{EB} & -\frac{2}{5}\mu_e E\sin\theta_{EB} & 0 & 0 & \frac{\Delta}{2}-\frac{2}{5}\mu_B B & 0 & 0 \\
0 & -\frac{2}{5}\mu_e E\sin\theta_{EB} & -\frac{1}{5}\mu_e E\cos\theta_{EB} & -\frac{\sqrt{3}}{5}\mu_e E\sin\theta_{EB} & 0 & 0 & \frac{\Delta}{2}+\frac{2}{5}\mu_B B & 0 \\
0 & 0 & -\frac{\sqrt{3}}{5}\mu_e E\sin\theta_{EB} & -\frac{3}{5}\mu_e E\cos\theta_{EB} & 0 & 0 & 0 & \frac{\Delta}{2}+\frac{6}{5}\mu_B B
\end{pmatrix}$$

2.4 Detection techniques

Due to their lack of cycling transitions, most molecules are substantially harder to detect than the commonly-used atoms. (Laser-coolable molecules, such as YO, SrF, and TiO, are exceptions to this statement.) The lack of optical cycling means that fluorescence generally yields at most a few photons per molecule—independent of exposure duration—while absorption techniques rapidly bleach the sample. Moreover, just as many atoms are rarely used due to the inconvenience of the laser wavelengths required for their spectroscopy, so too do many molecules only have deep-UV transitions. The difference is that the choice of molecule for an experiment is generally set by considerations other than simplicity of the laser system (e.g. the mass-to-dipole-moment ratio is a major motivation for using OH), and so one makes whatever sacrifices of convenience are required to get the necessary light.

In practice, there are four major families of detection techniques used in our experiments. The first, and most trivial, is the resonance fluorescence imaging used in the YO laser cooling experiment and illustrated in figure 2.7(a).

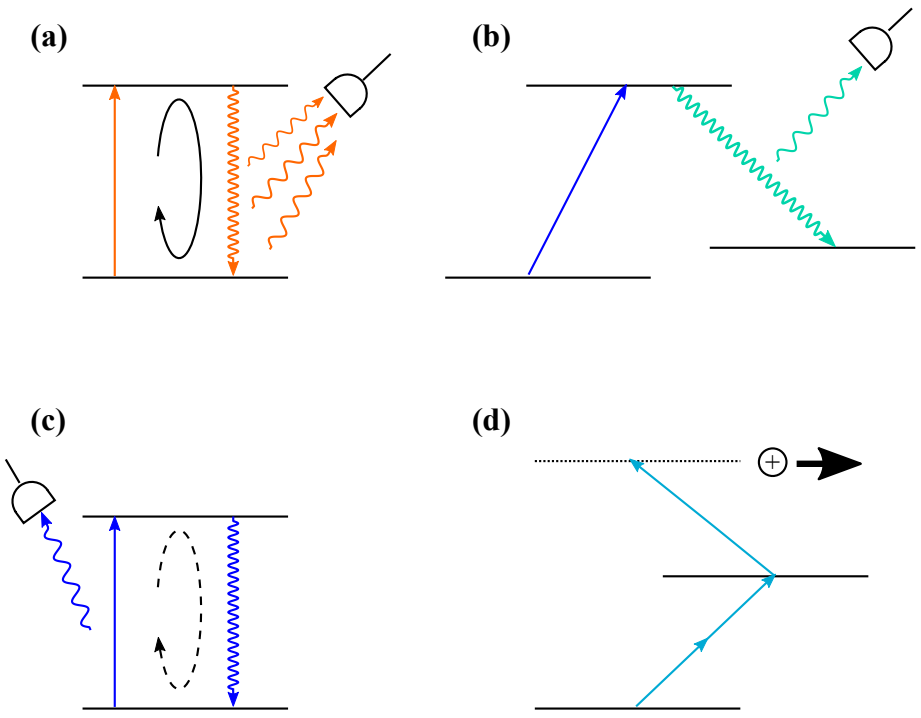

Figure 2.7: **Illustration of molecular detection techniques.** (a) Resonance fluorescence, where a single molecule scatters many photons which are directly detected. (b) Frequency-resolved single-photon laser-induced fluorescence, where only one photon is scattered per molecule but a Stokes shift enables efficient rejection of laser background photons. (c) Absorption detection, where the fractional loss of photons from the pumping laser is detected rather than the fluorescence photons. Optical cycling enhances the sensitivity but is not required. (d) Resonance-enhanced multi-photon ionization (REMPI), where the molecule is photo-ionized through a resonant intermediate level and the daughter ion is detected.

Since each molecule can scatter hundreds or thousands of photons, simply illuminating the sample with a resonant laser produces a bright enough image to directly record it with a CCD camera.

The second technique, used for some YO spectroscopy and for detection of OH, is single-photon, frequency-shifted, laser-induced fluorescence. Just as before, a laser excites a transition in the molecule. However, in this case the molecule fluoresces on a different transition and wavelength than the excitation laser, as schematically shown in figure 2.7(b). While this necessarily means that the molecule is now dark to the exciting laser, a sharp optical filter can be used to descriminate between the excitation light and the fluorescence. In combination with temporal gating and a single-photon-sensitive PMT, this technique allows extremely low backgrounds for the detection of small samples. It is, however, difficult to calibrate. Not only the fluorescence-collection efficiency, but also (when using a pulsed laser) the excitation volume are hard to calculate.

The third possibility, shown in figure 2.7(c), is absorption detection. As in the previous two techniques, a laser is tuned to a molecular resonance; however, instead of detecting the scattered photons, the signal here is the **loss** of photons from the laser beam. The fractional loss can be immediately converted into an optical depth, and if the optical absorption cross-section is known the optical depth can then be converted into an absolute (mean) column density. For true density measurements, absorption is the gold standard. Unfortunately, it is a libright-background technique: the absorption dip is a small change on a large baseline. If photon shot-noise is the only limit, absorption can be quite sensitive—but in the hostile environment of the Stark decelerator technical noise can be a severe issue. As of this writing, there is effort underway to demonstrate absorption detection of the magnetically trapped OH molecules, but the laser stability requirements are substantial.

The last family is photo-ionization, in the form of resonance-enhanced multi-photon ionization (REMPI). REMPI (figure 2.7(d)) comes in many forms, depending on how many photons and how many laser wavelengths are used. In the OH–ND_3 collision experiments, we used single-color 2+1 REMPI to determine the density of our cold ND_3 beam. This means that two laser photons combined to drive a two-photon transition to an intermediate level, and then a third laser photon ionized the excited molecule. Once ions are created, they can be extracted by an electric field and detected with a multi-channel plate (MCP). The MCP has near-unit detection efficiency, and so REMPI can be extremely sensitive.

The sensitivity of REMPI, however, does not make it any easier to determine an absolute density calibration.

Similar to pulsed-laser LIF, there is a large uncertainty associated with the ionization volume and the ion extraction efficiency. Moreover, since the ionization is a nonlinear process, perturbations in the laser mode structure are amplified in the effective mode volume.

Chapter 3

Stark deceleration and magnetic trapping

All of results reported in this thesis, other than laser-cooling, were achieved using a Stark decelerator[46, 47, 20] and magnetic trap[60, 61] machine. The premise of the system is simple: supersonic expansions yield gas packets which are very cold (~ 10 K) in their co-moving frame, but have a laboratory center-of-mass velocity of ~ 300–1000 m/s. If there was some way to collectively slow that packet down, the supersonic expansion would be an excellent source of relatively cold molecular samples. This slowing is what the Stark decelerator provides. Moreover, the Stark decelerator is capable of bringing a packet all the way to rest, so that the packet can then be captured in a magnetostatic (or electrostatic[62], or in principle microwave[63] or optical) trap.

3.1 Creating a supersonic beam

No Stark decelerator has colder or denser output than the beam source from which it is fed. Since the deceleration is a conservative (rather than dissipative) process, this statement is rigorously true, and therefore implies that it is potentially worth spending a great deal of effort to develop a high-brightness, low-temperature initial source. Unfortunately, while there is a large body of both research and theory on the behavior of supersonic expansion sources, the actual development of any real source continues to be a substantially empirical endeavor. (Consider, for instance, that the title of the **chapter** on source development in the thesis of E. Hudson[64] is "Sourcery.")

A basic picture of a supersonic expansion is shown in figure 3.1. The gas begins at some initial temperature T_0 and pressure P_0, with a very small mean velocity. Driven by the differential between P_0 and the external background

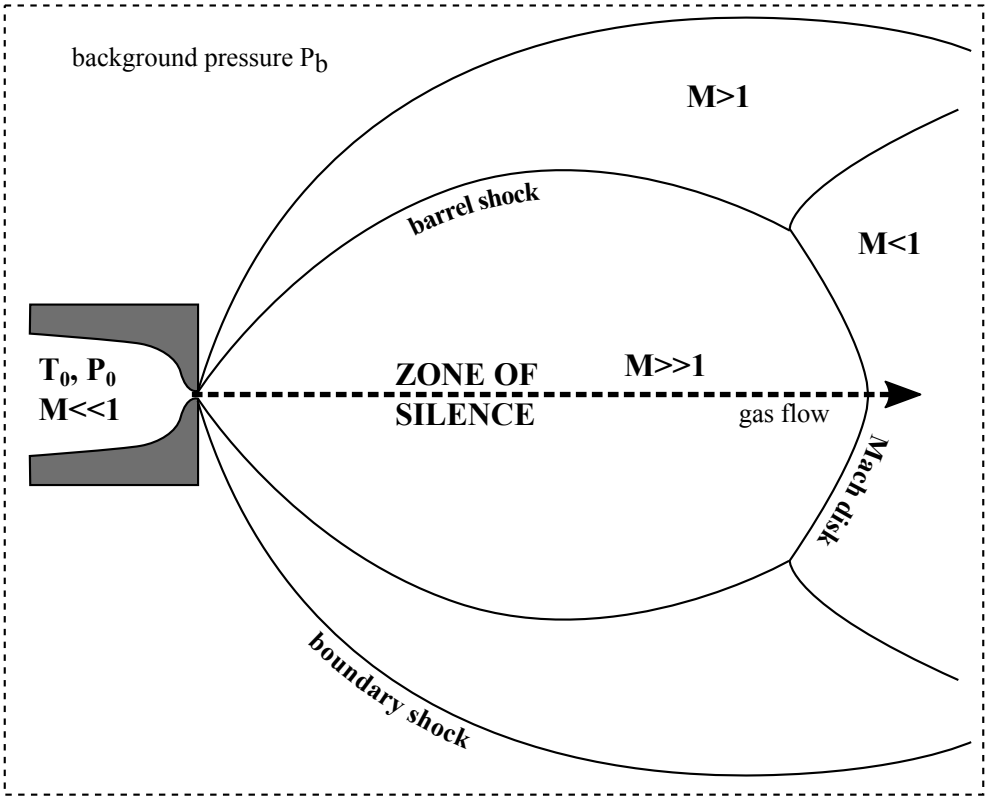

Figure 3.1: **Schematic view of a supersonic expansion.** Gas expands from the reservoir at left through the converging nozzle, then reaches supersonic speeds throught the zone of silence. Styled after Fig. 2.1 of [65].

pressure P_b, the gas flows out the nozzle of the expansion. If the pressure ratio exceeds a critical value

$$\frac{P_0}{P_b} > G \equiv \left(\frac{\gamma+1}{2}\right)^{\gamma/(\gamma-1)}$$

where $\gamma = c_P/c_V$ is the ratio of the gas's heat capacity at constant pressure to that at constant volume, the flow will reach sonic velocity (Mach number $M = 1$) at the nozzle's narrowest point. (Note that $\gamma = 5/3$ for an ideal monatomic gas and is less than 2.1 for all gases.) In this case, the pressure at the throat becomes independent of P_b and is equal to P_0/G. Since there still exists a pressure differential between the gas exiting the throat and P_b, the gas expands supersonically. This expansion means that any given parcel of gas performs isentropic work on the parcels downstream of it, and so the gas continues to both cool and accelerate away from the nozzle. Information cannot propagate upstream against the supersonic flow, so within the expansion the dynamics are independent of any boundary conditions, like the vacuum chamber walls. Of course, the expansion cannot propagate forever, so it is eventually terminated by a set of shocks. The region inside all of the shocks, where the expansion is unhindered, is sometimes called the "zone of silence" — referring to the fact that disturbances cannot propagate against the supersonic flow[65]. The expanding gas can reach transverse and rotational temperatures below 10 K with forward velocities of hundreds of m/s.

To acquire a cold beam from the supersonic expansion, it is necessary to somehow extract a region of the gas without permitting it to be slowed by any shocks. The usual way of doing this is to use a skimmer projected into the zone of silence. The skimmer is sharp-edged and carefully shaped so that it does not form a shock across its aperture, but rather allows the cold, expanded gas to transit through into a region of vacuum sufficiently high as to permit ballistic travel for the packet. In our machine, the skimmer has a 3 mm diameter aperture and is located 12 cm downstream from the valve nozzle. Once the packet has been skimmed, it is focused by an electrostatic hexapole into the first stage of the Stark decelerator.

3.2 Stark deceleration

The high-level description of Stark deceleration is simple, and illustrated in figure 3.2: a particle in a weak-field-seeking state feels a repulsion from a region of increasing electric field, and therefore slows down as it flies into one. If the field is turned off while the particle is inside it, the Stark potential energy that the molecule possessed is permanently removed from the system. Since this is a purely single-body effect and is independent of the initial

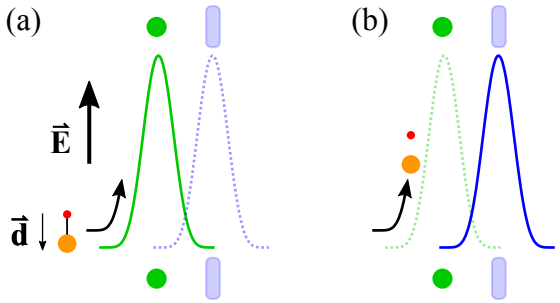

Figure 3.2: **Stark deceleration.** (a) A molecule in a weak-field-seeking state (dipole moment opposing $\vec{E}$) flies into a region of large electric field $\vec{E}$. The increase in the molecule's Stark potential energy U results in a reduction of its kinetic energy and therefore its forward velocity. (b) When the molecule has converted a selected amount of kinetic energy into potential, the electric field is turned off. This permanently removes U from the molecule, leaving it moving slower than it started. This cycle may be repeated by many stages in a linear decelerator.

velocity of the particle, it is a conservative process.

In principle, with a large enough electric field, a single stage of Stark deceleration can suffice to stop any molecular packet. In practice, however, laboratory fields are limited to a few hundreds of kV/cm, and so multiple stages of deceleration must be used. (For scale, our machine can remove a maximum of $\sim 1\ \mathrm{cm}^{-1}$ of kinetic energy per stage, and has 143 stages.)

In a multi-stage decelerator, the total degree of slowing is commonly quantified by the "phase-angle" φ, which is defined as

$$\varphi = \frac{Z_{\mathrm{switch}}}{2 l_{\mathrm{stage}}} \cdot 180^{\circ}$$

where Z_{switch} is the nominal position of the "synchronous molecule" (the notional molecule for which the switch timings are designed) at the time of switching and l_{stage} is the distance between adjacent rod pairs (i. e., a "stage" of the decelerator). Switching at 0°, or when the molecule is at the electric-field minimum directly between a pair of grounded rods, leads to pure bunching: molecules which are ahead of the the synchronous molecule are decelerated and molecules which are behind are accelerated, leading to spatial confinement of a distributed packet. Switching at 90°, when the molecules are at the field maximum between a pair of charged rods, removes the maximal amount of energy from the synchronous molecule but provides no bunching. The advantage of using the phase angle, rather than the switching time or position, is that it enables comparison of different decelerator geometries and is independent of the current speed of the packet.

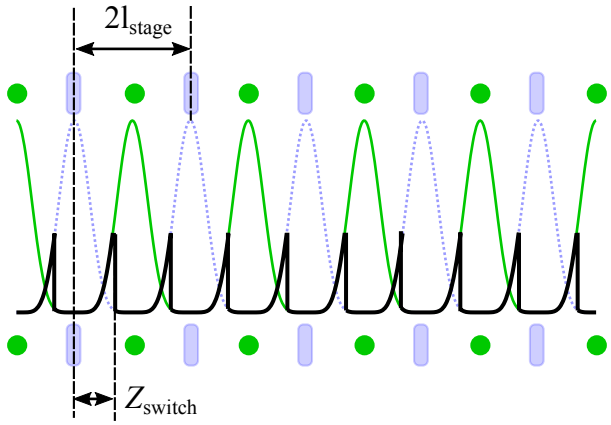

Figure 3.3: **Phase angle in a multi-stage decelerator.** The solid green and dashed blue curves indicate the approximate shape of the Stark potential for the two alternate switching states; the heavy black curve shows the Stark energy of the synchronous particle as it traverses the decelerator. (The total kinetic-plus-Stark energy decreases stepwise at each switching point.) The phase angle is defined as $\varphi = Z_{\text{switch}}/2l_{\text{stage}} \cdot 180^\circ$ so that maximal slowing occurs at $\varphi = 90^\circ$.

The use of multiple stages substantially complicates the dynamics in a real decelerator. Since molecules experience repeated, quasi-periodic kicks in both the longitudinal and transverse dimensions, resonances may be excited[49, 66]. These resonances, and the longitudinal/transverse couplings needed to understand them, are treated fully in the theses of E. Hudson[64] and B. Sawyer[67].

3.3 Magnetic trapping: a story in $2\frac{1}{2}$ acts

There are many reasons to seek to **magnetically** trap molecules. Electrostatic trapping[68] is, in many ways, less challenging since it enables extremely deep traps—but theory predicts that polar molecules will invariably suffer rapid inelastic losses in the large electric fields required to trap molecules at 50 mK temperatures[69]. (Our own observations of electric-field-induced inelastic collisions are discussed in chapter 6.) Optical trapping of polar molecules has been demonstrated at microkelvin temperatures for molecules created from laser-cooled atoms[51], but the kilowatt-scale optical powers required to confine molecules at 10 mK have so far precluded the use of optical trapping on molecules directly cooled from room temperature.

3.3.1 Version 1.0: the electromagnet trap

The first magnetic trap for OH molecules was a electromagnet-created magnetostatic quadrupole[60], shown schematically in figure 3.4. Each trap magnet consisted of four turns of hollow, Kapton-insulated square wire, through which cooling water was circulated. The laser for LIF propagated longitudinally through the magnets and up the decelerator, and fluorescence was imaged out the side. A set of six large rod electrodes permitted the application of either a homogeneous or quadrupole electric field to the trapped molecule sample.

Trap loading was accomplished magnetically (figure 3.5): as the molecules exited the decelerator and flew into the trap region, only the downstream magnet was turned on. The half of the molecules in a magnetic weak-field seeking state[1] were stopped by the magnetic field, and then the front magnet coil was also turned on to create the quadrupole trapping potential.

In order to achieve magnetic fields of sufficient strength with magnets of only four turns, exceedingly high currents of up to 2000 A were required. The molecular packet was slowed to 20 m/s, at a phase angle $\varphi = 47.45°$.

[1] The Stark decelerator slows molecules in the $\left|f;\pm\frac{3}{2}\right\rangle$ states, but only the $\left|f;\frac{3}{2}\right\rangle$ state is magnetically trappable.

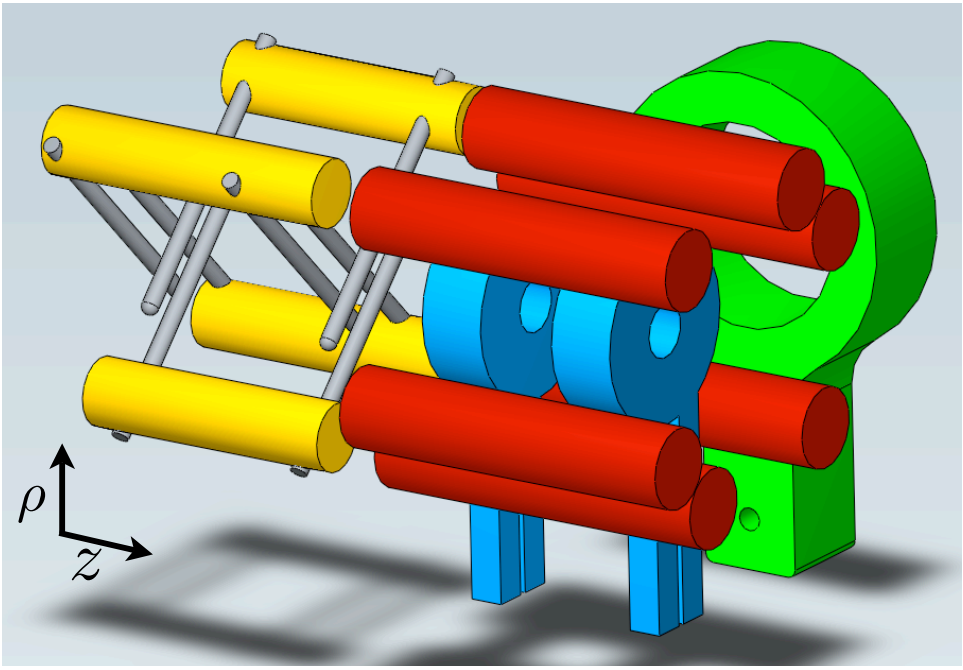

Figure 3.4: **The electromagnet trap.** The molecules exit the Stark decelerator (yellow and gray rods) and then fly into the trap region between the electromagnets (blue rings). The electric field rods (red) permit the application of electric fields with either uniform or quadrupole geometry. Fluorescence is collected out the side by a lens held in the green lens mount.

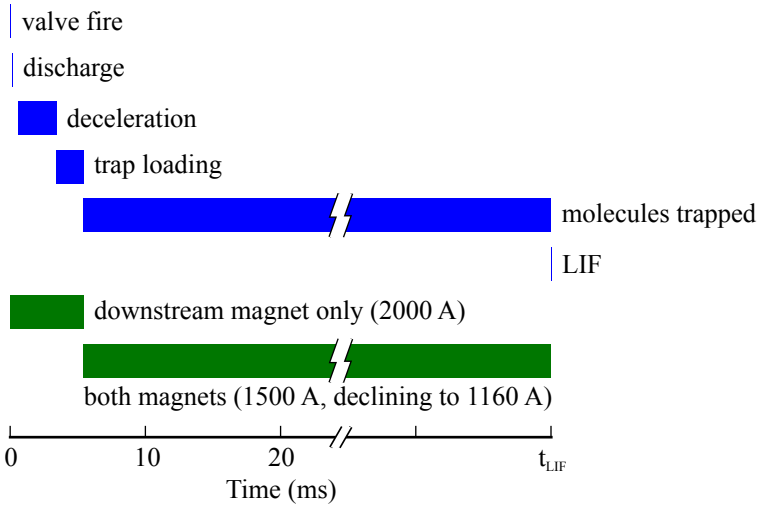

Figure 3.5: **Loading sequence for the electromagnet trap.** Molecules entered the trap after Stark deceleration with only the downstream magnet powered; after the molecules were stopped by the magnetic field gradient, the upstream magnet was powered up to create the confining quadrupole potential.

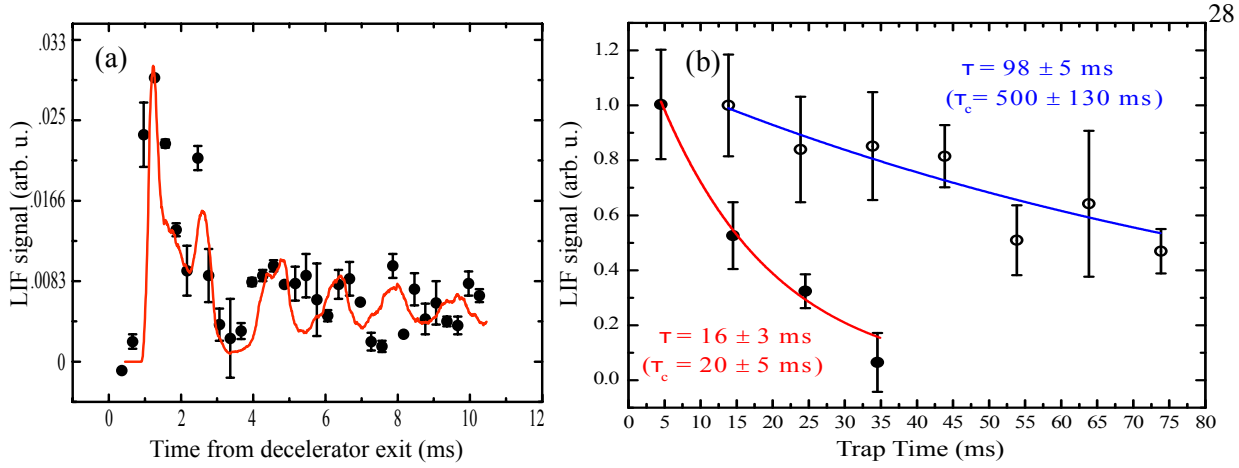

Figure 3.6: **Performance of the electromagnet trap.** (a) Fluorescence versus time curve showing the loading of the trap. The red line is a Monte Carlo simulation of the loading dynamics. (b) Lifetime measurements in the electromagnet trap. Solid points were taken with a background pressure of 1×10^{-6} torr of N_2, while open points had 4×10^{-8} Torr.

The downstream coil was driven with 2000 A, yielding a maximum stopping velocity of 22 m/s. Switching on the upstream coil (in series with the downstream coil) to close the trap reduced the current to 1500 A over 800 μs due to the increase in resistance; the current then decayed at a rate of 2000 A/s down to a steady-state level of 1160 A due to the high-current supplies' internal regulation circuitry. At 1500 A, the trap operated with a 6700 G/cm gradient with a center-to-center magnet spacing of 1.5 cm.

Some typical results from the electromagnet trap are shown in figure 3.6. A fluorescence versus time curve (often referred to as a time-of-flight trace) of the trap loading is shown in figure 3.6(a). The first peak shows the packet's flight through the trap center before it is stopped, while the second reveals the pile-up of the stopped molecules. The sharp decrease in mean number between the second peak and the later steady-state is due in large part to the fast 25% reduction in the total trap current. figure 3.6(b) shows two measurements of the one-body-loss limited lifetime of molecules confined in the trap. The red and blue fitted lines yield lifetimes of 16 and 98 ms, respectively. Deconvolving out the losses due to the ramping of the trap current from 1500 down to 1160 A yields background-gas-limited lifetimes of 20 and 500 ms.

Driving the electromagnet coils presented serious technical difficulties. At the high currents used, ordinary #00-gauge welding cable is insufficient: we used water-cooled cables usually sold for robotic arc-welding equipment. The currents were supplied by a pair of 500 A programmable supplies operating in parallel. Fast coil turn-off was achieved

by the use of a hockey-puck-sized 6000 A high-power diode, although this in turn created large dI/dt voltages due to the inductance of the magnet coils. Safely switching these currents required a water-cooled bank of high-current MOSFETs and a custom board to drive the gate of each MOSFET individually. (The circuit diagram for this board may be found in [67].)

3.3.2 Version 2.0: switching to permanent magnets

Given both the technical difficulties of handling 2000 A and the low densities achieved using electromagnets, after the initial demonstration our focus rapidly turned to searching for a new trap design. The low trap density (then estimated at 10^3 cm^{-3}, but possibly as high as 10^6 cm^{-3} given the densities implied by chapter 7) had three obvious causes. The first was the volumetric mismatch between the decelerator packet and the quadrupole geometry. The decelerator has a rod-to-rod stage spacing of 5.461 mm; at a phase angle on the order of 45°, that implies a 2.5 mm longitudinal length of the packet at the last switch of the decelerator. The transverse size is likewise set by the decelerator dimensions, in this case the 2 mm × 2 mm square profile created by the alternating rod pairs. The second cause builds upon the first: the packet freely expands as it traverses the distance from the last stage to the trap. This means that there is great value in getting the trap as close to the decelerator as mechanics and high-voltage considerations allow. The third cause is the trap loading velocity. Lower loading velocities hurt twice, first from the rapid drop in decelerator efficiency as velocities go below about 50 m/s, and then a second time because slow velocities mean more time for the packet to expand before it enters the trap.

These three issues clearly motivate the design criteria for an optimal magnetic trap. The ideal trap would be as close to the decelerator exit as possible, tightly confining with a size matched to the packet's own size at trap loading, and would be able to stop and confine a very fast packet. Since it took 2000 A to stop a 20 m/s packet using electromagnets, magnetic stopping did not seem to be a promising avenue — although the use of high-field, short-pulse magnets was considered. The coupled issues of the size of the trapped packet and the size of the trap magnets (the latter setting how close the trap can get to the decelerator) implied a need for extremely large field gradients, typically achievable only through either permanent magnets or superconductors. The latter would pose tremendous technical challenges, and so we focused on permanent magnets.

The key insight of the permanent magnet trap was that the stopping potential, to load the trap, could still be

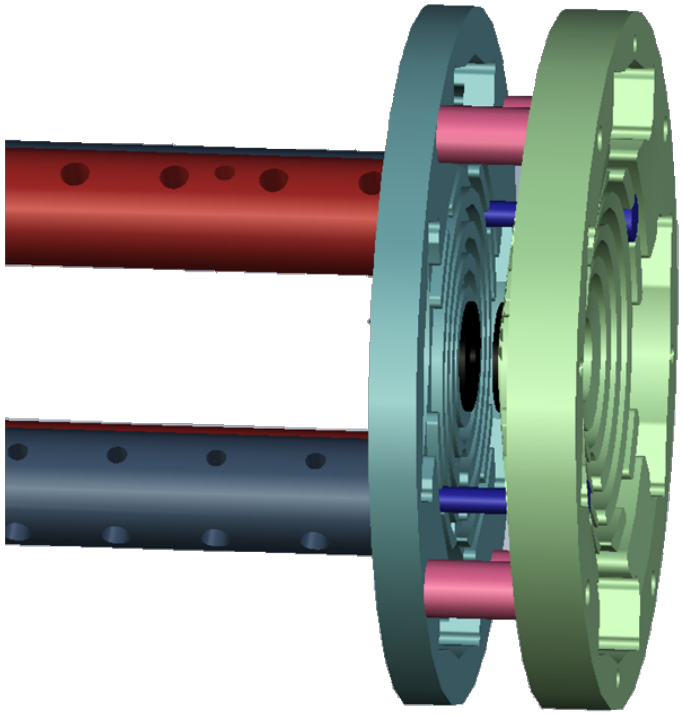

Figure 3.7: **The first-generation permanent magnet trap.** Molecules exit the Stark decelerator from the left, and are loaded into the trap between the two magnets (small black rings at center of the larger green and cyan mounting fixtures). The mounting fixtures also provide a slot which holds a lens mount (not shown) for fluorescence collection.

electrostatic (i. e., Stark stopping) if we used the surface plating of the magnets as electrodes. The strongest permanent magnets available are of neodymium-iron-boron (NdFeB) composition, and can provide remnant magnetizations B_r of up to 1.48 T (grade N52) at temperatures up to 80° C [70], or slightly less at higher temperatures. The magnets, however, are vulnerable to rapid corrosion by water vapor and so are almost always encased in some non-permeable coating. The most common surface coating is a three-layer stack of electroplated nickel, copper, and then nickel again. Electric fields do not affect the magnetic properties of the material, and testing indicated that the nickel plating is sufficiently clean and smooth as to support high voltages in a vacuum, so the combination of a permanent magnet quadrupole with electrostatic stopping became our design target.

The actual design process consisted of two parallel tracks. The first was the optimization of the magnet geometry. In order to maximize the optical (or molecular-beam) access to the trap, we decided on a ring magnet geometry with the Stark-decelerated packet entering through the bore of one magnet. In addition to providing 360° optical access, this ensured that the longitudinal velocity width of the packet (expected to be substantially larger than the transverse width) would be matched by the stronger confinement direction of the trap. (Magnetic quadrupoles have twice the gradient and depth in their longitudinal direction as in the transverse.) Moreover, the electric field generated between the decelerator and the upstream magnet during the trap loading is mildly focusing in the transverse direction, which may provide a further enhancement to the loading efficiency.

The actual geometry optimization was an iterative process, alternating between calculating field geometries for a given magnet shape using a finite-element package (COMSOL) and estimating the resulting trap's loading efficiency using Monte-Carlo dynamics simulations. The final choice consisted of two identical magnets of Grade N42SH material ($B_r = 1.24$ T with a maximum temperature of 150° C to allow baking the vacuum chamber), arranged anti-Helmholtz with a 3 mm gap between the magnets. Each magnet is a square cross-sectioned ring, with an ID of 4 mm, an OD of 12 mm, and a thickness of 4 mm. This geometry appears to provide the maximum effective trap depth, limited by the shoulder of the trap on the surface of each magnet facing the gap as can be seen in figure 3.8(a). The shoulder appears because of the hole in the center of the magnet: field lines can either exit through the bore **or** out the sides, and so a secondary, toroidal minimum appears between the faces of the magnets in addition to the 3-D quadrupole at the center of the trap. This toroidal minimum runs into the surface of the magnets at a lower field magnitude than either the longitudinal or transverse saddle points.

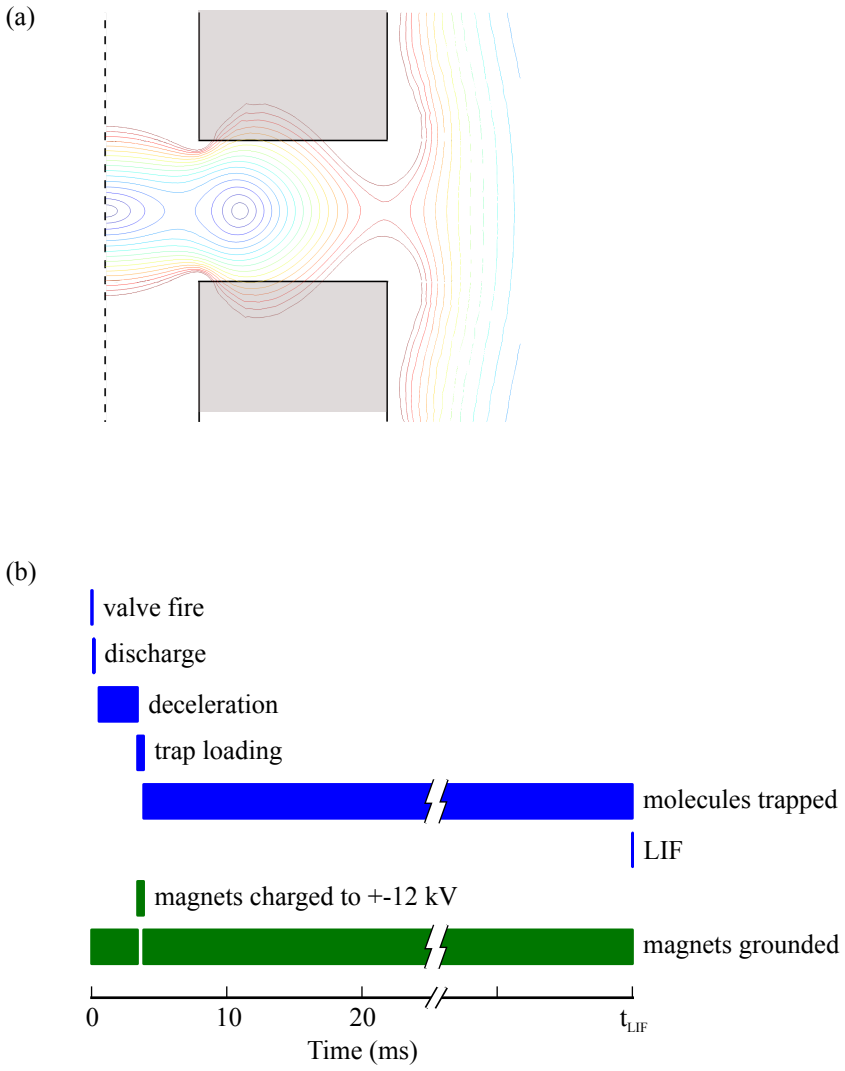

Figure 3.8: **Details of the permanent magnet trap.** (a) Contours of equal B (spaced by 25 mT), showing the geometry of the trapping potential created by a pair of permanent ring magnets. (b) The electrostatic stopping sequence used to load the permanent magnet trap.

The second track in the trap design focused on the mechanical mounting of the magnets. While the magnets are strong and mounted in a repulsive orientation, the forces between them are not that large — no more than 10 N or so. However, the magnets need to be able to support a 30 kV potential difference between them, and also be safely isolated from the ± 12.5 kV on the Stark decelerator rods. This requirement is in direct conflict with the desire to get the trap center as close to the end of the Stark decelerator as possible. In addition, the trap needs to be very accurately registered to the decelerator: the magnets must both be parallel and coaxial to the decelerator bore. The obvious way to achieve this is to mount the trap directly to the decelerator, and so we designed a set of dielectric holders for the magnets, machined from Ultem polyetherimide plastic. The holders are illustrated in figure 3.7: the upstream mount was as thin as possible, allowing the trap center to be only 10 mm from the center of the last decelerator rod. The downstream mount, however, had a truncated-conical structure so that the supports between the two mounts could be lengthened to reduce surface currents between the magnets[71]. The upstream mount was attached directly to the decelerator, with precision-machined seats to reference it to the four large decelerator support rods and holes so that it could be screwed onto the tapped holes available in two of those rods. The magnets were seated so that their repulsion would push them further into their seats, and high-voltage connections were made through a set-screw also used to anchor the magnets.

We originally electropolished the magnet plating using currents of a few amps for roughly 45 seconds, but determined over the course of the experiment that such polishing was at best unnecessary and possible detrimental to the actual voltage-handling performance of the magnets. Certainly the risk of scratching the magnet plating outweighs the gain from the polishing. However, while the magnets themselves show excellent high-voltage characteristics, the same cannot be said for the hardware used to connect the high-voltage feed wires. We use Kapton-insulated wire, mainly for its convenience: the Kapton is not thick enough to provide any insulation above a kilovolt or so. (Kapton-wrapped wire with a rating of 10 kV is commercially available, but the thickness of the insulation makes the wire unmanageably stiff.) As long as the wire maintains a clearance of ~ 5 mm from any other conductor, there are no issues. If the wire brushes the vacuum chamber wall, however, it **will** short out in operation. Moreover, since the magnets are only 3 mm apart, so too are the connectors — which would not work. To mitigate this issue, we oriented the connectors so that the upstream magnet's connector is on top, while the down-stream one is on the bottom. Isolation of the decelerator rods was also initially an issue due to surface-currents across the Ultem, but that was fixed by the

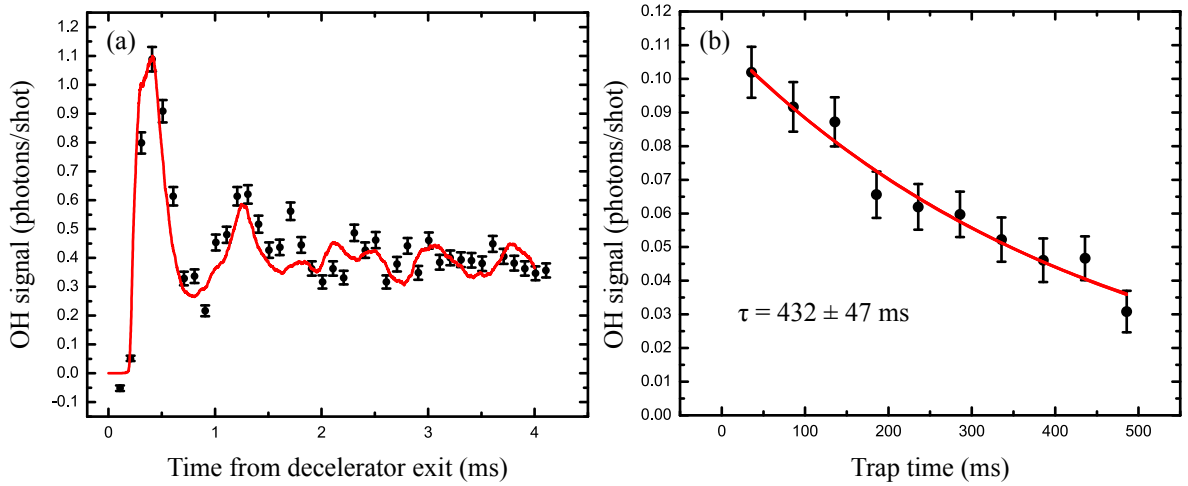

Figure 3.9: **Performance of the permanent magnet trap.** (a) Fluorescence versus time curve showing the loading of the trap. The solid red line is a Monte Carlo simulation of the loading dynamics. (b) Lifetime measurement in the permanent magnet trap demonstrating vacuum-limited lifetimes of almost half a second.

insertion of $\frac{1}{16}$ in. ceramic (Macor) caps on the ends of the decelerator support rods. The ceramic has surface-current properties which are so much better than the plastic that even such a tiny thickness was enough to completely end the surface-tracking issues.

The performance of the permanent magnet trap is shown in figure 3.9. While the fluorescence-collection geometry is somewhat different (the permanent magnet trap slotted a lens into the trap mounts, allowing a $f = 5\,\mathrm{cm}$ lens to be mounted 5 cm from the trap center), the difference in scale between figures 3.9 and 3.6 is illustrative. The permanent magnet trap provides OH densities at least two orders of magnitude larger than the electromagnet. Moreover, without the current-sag issues described in section 3.3.1, only a bake-out to 100° C was required to achieve a 400+ ms trap lifetime.

Loading of the trap used voltages of $\pm 12\,\mathrm{kV}$ to stop a 36 m/s packet from a decelerator phase angle $\varphi = 50.352°$.

3.3.3 Versions 2.2 and 2.5: Variations on a theme of fixturing

The great success of the original permanent magnet trap has meant that we have not yet made any further changes to the magnetic field geometry or the choice of magnets. Indeed, the trap described in the previous section was used almost unchanged for three years during the experiments described in chapter 4. However, more recently we

have experimented with changes to the magnet support structures in pursuit of several goals.

The first variation in trap mounting was the "cryogenic trap," shown in figure 3.10. This mounting design had two goals. The first was to permit the application of a microwave field across the trapped molecules, to enable control of their Λ-doublet state and thus permit collision studies with $|e\rangle$-state molecules. (See chapters 5 and 7.) The second design goal was an attempt to improve the vacuum-limited trap lifetime by using the trap itself as a cryopump to remove background krypton gas from the supersonic expansion. We have known since the electromagnet trap that, once the residual water vapor has been remove by either a 100° C bake-out or simply enough pumping time, the vacuum is dominated by diffuse, 300 K krypton. The clearest demonstration of this fact is that the OH lifetime varies inversely with the experiment repetition rate: at a 5 Hz rate, the lifetime is twice as long as at 10 Hz. By lowering the repetition rate to 1 Hz, we have observed lifetimes of over a second.

Since longer lifetimes would provide improved signal-to-noise at a fixed repetition rate, we decided to try to reduce the background krypton density. We were unable to design a support fixture which mounted directly to the decelerator **and** had a large enough thermal resistance to enable cooling to 77 K, so this fixture was free-standing on the bottom ConFlat flange of our 6-inch cube chamber. The fixture consisted of first a thermal-break stage made of Macor machinable ceramic, to minimize heat flow from the vacuum wall, and then an electrically insulating but thermally conductive alumina block which provided the thermal contact between the liquid nitrogen flow line and the 316L stainless steel arms which held the magnets. (316L was chosen due to it having a lower rate of acquiring ferromagnetic lattice impurities than 304SS when cooled to cryogenic temperatures.) Each arm was referenced to the precision-ground alumina block by a shallow, three-sided rectangular cup on the end of the arm; connection force was provided by a gold-plated screw which penetrated a clearance hole in the alumina and anchored into a tapped hole in the end of the arm.

The magnets in this fixturing system were in blind cups, with a thin stainless-steel plate facing the trap center. The concept was that a well-electropolished steel surface might permit higher stopping voltages than the magnet plating. However, on the first installation of the trap, a problem with this mounting design became immediately obvious: the magnets' mutual repulsion actually pushed them out of the fixture. Originally, the magnets had been held in by a single set-screw; after this problem became clear, the arms were modified to take a thin retainer plate affixed by two screws, to keep the magnets confined.

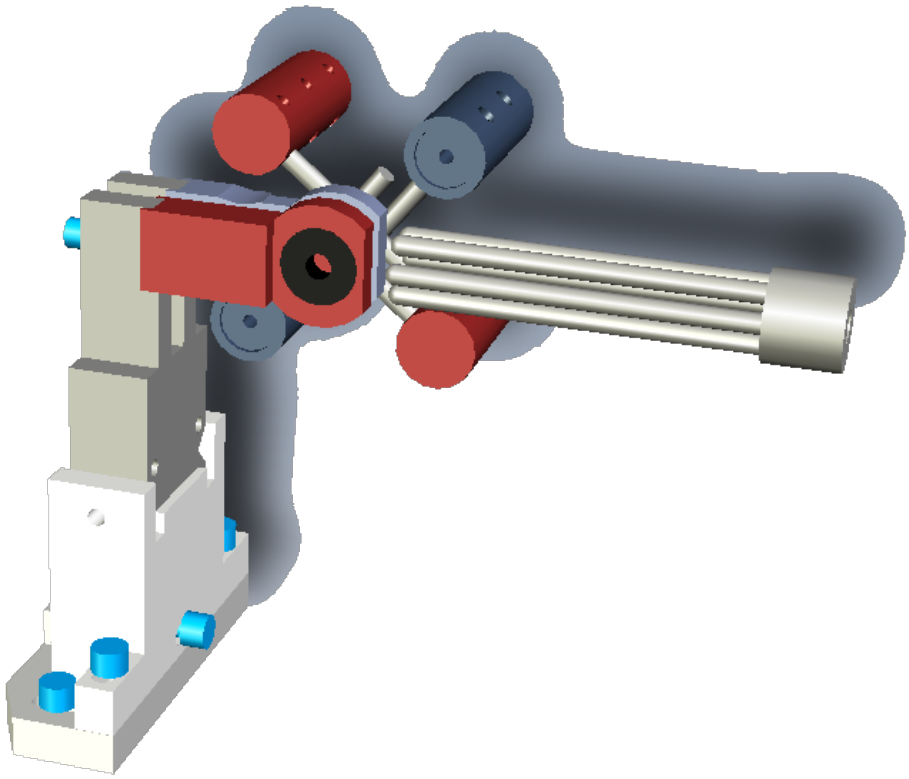

Figure 3.10: **The cryogenic permanent magnet trap.** The trap magnets (black rings) are supported by thermally conductive stainless steel arms, which are in turn supported by a complex mounting stack. From the bottom, the stack consists of a steel base-plate, a thermally and electrically insulating Macor ceramic fixture (white), and a thermally conductive but electrically insulating alumina standoff (gray). The alumina standoff allows the steel arms and trap magnets to be cooled to 80 K by a liquid nitrogen cooling loop (not shown). The steel mounting arms also provide a transmission-line geometry to permit coupling microwave fields across the trapped molecules.

The goal of applying microwaves to the trap was accomplished easily. The actual circuitry is described in chapter 5; the in-vacuum transmission line feeds were attached to the gold-plated screw, so that microwaves could propagate down the fixture's arms in a continuation of the transmission line geometry. Measurements using an ultra-high-speed oscilloscope indicated that microwave fields of several V/cm (across the 3 mm gap) were easily attainable using only $\sim +15$ dBm of applied power.

The goal of cryopumping krypton, however, was a total failure. No difference in either vacuum gauge readings or trap lifetime was observable when the trap was cooled to 77 K with flowing liquid nitrogen. The equilibrium vapor pressure of krypton at 80 K is still 5 mbar[72], so any pumping would have to occur as result of surface cryosorption. The binding energy of krypton on clean, polished steel or copper is presumably low, so the lack of pumping is not entirely surprising. It remains possible that krypton could be pumped using a high-surface-area charcoal or zeolite cryosorption system, but this trap fixture did not contain any.

One other difficulty of this fixturing system was alignment. The original system mechanically referenced the magnets directly to the decelerator, and the fluorescence collection lens to the magnets. (The second lens which focuses the fluorescence through the iris has always been free-standing, however.) With this new system, however, the entire stack had to be aligned by hand to the decelerator. The system was designed with three axes of translational adjustment and one axis of rotation (vertical), so that a set of feeler tools and centering pins could be used to achieve proper alignment. This process was slow, and apparently trouble-prone: after the initial alignment and several months of use, on a subsequent vacuum break the magnets appeared to be rotationally misaligned by possibly as much as 15°.

The fluorescence lens alignment also proved to be challenging. With the lens now supported from a 2.75" CF flange at the base of the cube, the tip-tilt alignment of the lens appears to be responsible for at least factor-of-three variations in the fluorescence collection efficiency. The solution I used is that the flange was originally connected using the minimum compression of its copper gasket needed to achieve a seal. Then, with the system operational, the bolts were selectively tightened to maximize the fluorescence signal on the bunching peak. This may not have been the truly optimal solution, either, since the narrow time structure of the bunched peak is convolved with the optimal longitudinal position of the focal point. In hindsight, optimization using the trapped signal would have been better — but the 20X reduction in signal-to-noise between bunching and trapping would have made the process much slower still.

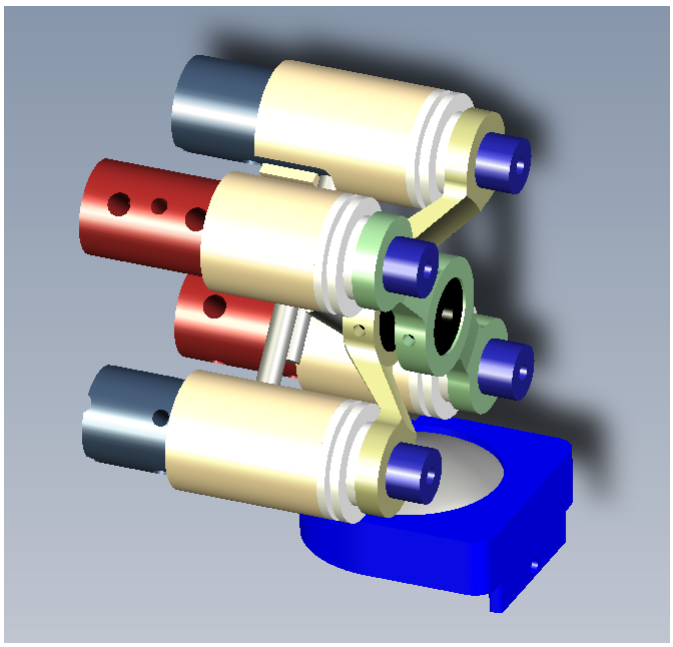

Figure 3.11: **The present permanent magnet trap.**

The final trap variation described in this thesis (figure 3.11) is in many ways a rejection of the cryogenic design. Instead, it is a return to the original fixturing method with some major optimizations. The goals for this newest system were a return to mechanically referencing the trap directly to the Stark decelerator, a continuation of the easy application of microwave fields, and a continuation of the previous trap's success in using only metals and ceramics for its construction (rather than the plastic used in the original mount). The resulting design is simple and elegant: each magnet is held in a steel bar supported diagonally by two of the four decelerator rods. In order to provide the electrical isolation between the decelerator rods and the trap supports, a Macor stand-off is used. The fastening of the stand-off to the decelerator support rod is the true elegance of this system. A titanium sleeve fits over the end of each rod, and has an L-slot which locks over the last decelerator rod. The sleeve has a shallow, internally-threaded cup on its end, into which the Macor stand-off is screwed. The stand-off then has a blind, tapped hole in its center, which is used to anchor the magnet support.

Applying the lessons of the previous mount, the magnets are again inserted so that their plated surfaces face the trap center and their mutual repulsion serves to keep them seated. The microwave transmission line is now connected horizontally to each mount by a titanium set-screw. The set-screw was drilled out, and a rigid copper wire soldered into it using vacuum-compatible Ag-Sn solder, with a ring-terminal soldered to the other end of the wire. The wires were hand-bent to create the transmission-line geometry, with several rounds of iteration required to get a nice, parallel, symmetric geometry and a good fit. As with the original trap, one high-voltage feed is connected at the top of the upstream mount, and one is on the bottom of the downstream mount. The fluorescence-collection lens, however, remains supported from the vacuum flange.

Chapter 4

Cold beam-trap collisions

Following the achievement of magnetically trapping OH, one immediately obvious use for a trapped sample is the study of molecule-atom and molecule-molecule collision cross-sections. The long trap lifetime allows for even a very weak source of collision-partner particles to be used, since loss may be integrated over hundreds of milliseconds. The signal of interest is the **fractional** loss of trapped OH molecules, so an absolute density calibration of the trap is not needed. However, to determine true, absolute collision cross-sections, the velocity and density of the impinging probe beam are needed. Since these two quantities are generally much harder to measure than the loss of OH molecules, their systematic uncertainties therefore dominate the overall uncertainty of the measured cross-sections. The fractional loss of trapped molecules χ may be considered as effective "absorption" by the colliding beam, and so the Beer-Lambert law says

$$\chi = e^{-n\sigma v\tau}$$

where n is the density of the collision partner, v is its velocity, τ is the duration of the collision packet, and σ is the effective cross-section.

It is important to emphasize that the observed σ in a beam-trap experiment is only an **effective** cross-section[73]. Specifically, it is the "cross-section for any scattering process which causes disappearance of fluorescence." In the case of OH, this means that it includes inelastic scattering to the $|e\rangle$-state (since LIF is state-sensitive), inelastic scattering to lower, untrapped levels of the $|f\rangle$ manifold, and any collision which transfers enough momentum to eject the OH molecule from the trap. Unfortunately, the last type of collision may only be a fraction of the total elastic cross-section, particularly in the presence of strongly anisotropic scattering. This leads to a greater reliance on theoretical calculations to back out the true, total elastic cross-section than might otherwise be desired.

4.1 OH–He and OH–D_2 collisions at 77 K

The great success of the first permanent magnet trap (described in section 3.3.2) prompted an immediate desire to use it for real measurements[61]. An ongoing theme in our study of OH has been its relevance to astrophysics, and its collisional properties are no exception. Astrophysical masers emitting on the OH Λ-doublet transitions have been attributed to collisional pumping by H_2[74, 75]. However, molecule-molecule collisions remain substantially intractable to calculate using *ab initio* methods, prompting theorists to try to approximate the cross-section using OH–He calculations. As there was no scattering data available at the temperatures of interest below the lowest OH rotational excitation, these properties were a prime target for a demonstration of the power of beam/trapped-molecule collision experiments. Unfortunately, our turbomolecular pumps do not efficiently remove H_2 from our vacuum system due to its exceptionally low mass. Therefore, we chose to compare OH–He collisions to OH–D_2 instead, since the pumps are equally effective upon the two gases. While the different mass and rotational constant of D_2 as opposed to H_2 may give it substantively different scattering properties, if OH–D_2 collisions are noticeably different from OH–He it is likely that OH–H_2 collisions are as well.

4.1.1 Cryogenic supersonic expansions for tunable-velocity He and D_2 beams

The apparatus used for this first collision experiment was extremely simple. A stainless solenoid valve (General Valve Series 99) was outfitted with a custom Kel-F poppet tip, with the material chosen so that the valve would continue to seal down to cryogenic temperatures[76]. The valve was driven with a high-voltage supply (generally 140-300 V), enabling a very fast opening time. The switching circuit (figure 4.2(a)) is single-ended, with a transient-voltage suppressor (TVS) connected to ground. When the supply switch was opened, the reactive voltage from the solenoid's inductance is above the TVS's clamping level, and so it becomes conducting and very rapidly drains the current from the coil to achieve a fast shut-off of the solenoid. The valve's true closing speed, however, is not set by the solenoid but by a spring mechanically pushing the poppet into place to seal. The high opening forces from the fast solenoid turn-on cause the poppet holder to have enough momentum that the poppet bounces several times before the valve fully seals. To prevent the bounces, we fired a second, shorter current pulse through the solenoid to act as a brake against the spring forces slamming it closed, as illustrated in figure 4.2(b). With a two-pulse sequence, we were able

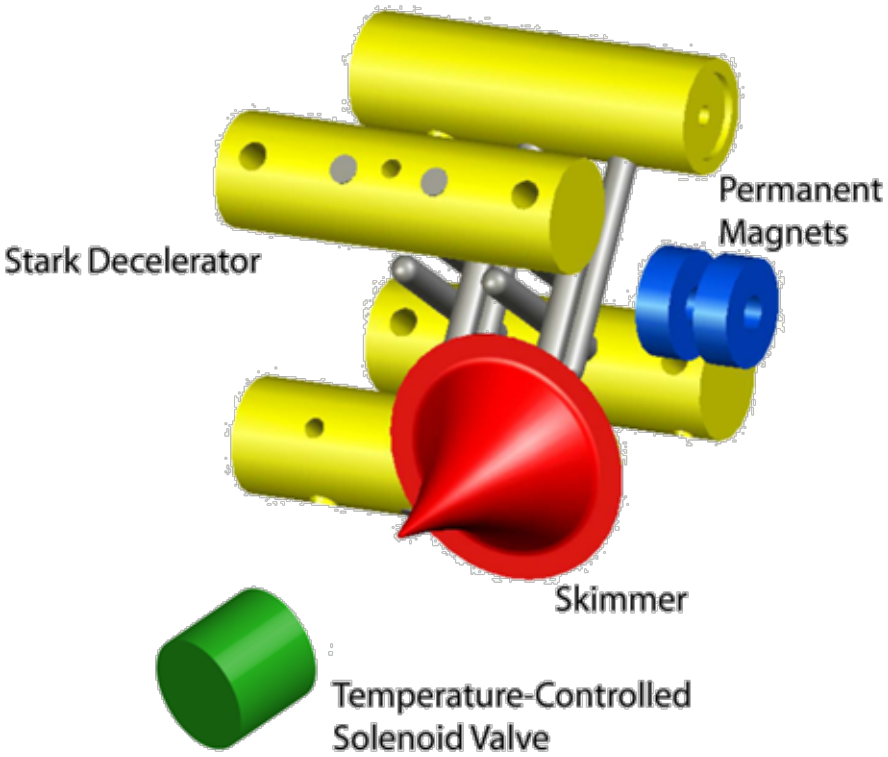

Figure 4.1: **Experimental system for OH–He and OH–D_2 collision experiments.** OH molecules exit the decelerator (yellow, rear-left) and are electrostatically stopped and loaded into the permanent magnet trap (blue rings). The molecules are allowed to settle before a supersonic pulse of collision gas (He or D_2) is fired from the solenoid valve (green cylinder) through the trapped cloud.

to achieve gas pulses as short as 160 μs FWHM (figure 4.2(c)).

In order to achieve the desired low collision energies, the entire solenoid valve was immersed in liquid N_2, in a custom vacuum-insulated vessel designed to mate with the vacuum feed-through system used by the fast pulsed valves sold by Jordan TOF Products, Inc. A custom nozzle flange was made for the solenoid valve which was wrapped with 25 turns of manganin wire to allow control of the nozzle temperature between 77 and 330 K, as measured by a cryogenic silicon diode. The resulting supersonic beam velocities were measured by a two-position time-of-flight technique, and showed that the velocity scaled smoothly as $T^{1/2}$ as shown in figure 4.3(a). The valve nozzle was 1 mm in diameter, and opened in a 40° cone to enhance the beam brightness. The valve was operated with a 2.0 bar backing pressure for He and 2.7 bar for D_2; this enabled minimum center-of-mass collision energies of$\sim 60\,\mathrm{cm}^{-1}$ and $\sim 145\,\mathrm{cm}^{-1}$ respectively. We observed an 8% velocity width in the He beam, implying an energy resolution of $9\,\mathrm{cm}^{-1}$ at the lowest collision energy. The beam density was also temperature-dependent, but easy to calibrate using a fast ionization gauge as shown in 4.3(b).

4.1.2 Collision results

The experimental sequence for this experiment (figure 4.4) was as simple as the equipment: OH molecules were decelerated and trapped, allowed to settle for 24 ms, and then the pulsed valve was fired. The fluorescence signal was measured alternately before and after the gas packet had flown through the trap, to determine the fractional scattering. Determination of the total cross-section for collisions which cause trap loss then required knowledge of the gas pulse's density n and velocity v.

It is easy to determine the velocity of a gas pulse: simply record its arrival time at two distinct positions and divide the distance between them by the difference in times. Density, while more complex, was not a major difficulty either. We took advantage of the temperature control available on the valve to measure the OH–He collision cross-section near a collision energy of $250\,\mathrm{cm}^{-1}$ twice: once using a velocity-tuned packet from the valve, and a second time using thermal, 298 K helium leaked into the chamber. The latter experiment allowed the helium density to be measured using a calibrated ionization gauge, and the OH–He cross-section to be determined from the OH molecules' lifetime in the magnetic trap. In combination, these two measurements established an absolute scale for the measured cross-sections; relative measurements of the beam density at each temperature using a fast ionization gauge then enabled the

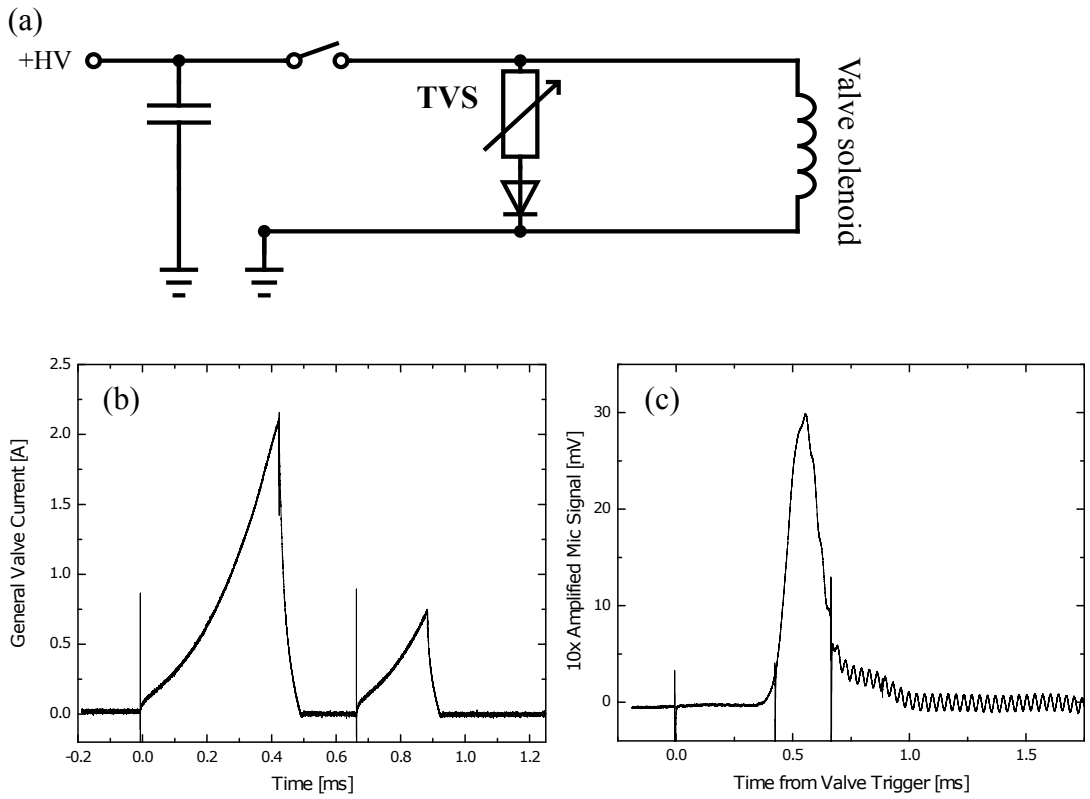

Figure 4.2: **Cryogenic solenoid valve circuit and performance.** (a) Circuit diagram of the single-ended solenoid drive circuit, including the transient voltage suppressor (TVS) used to achieve fast turn-off. (b) Solenoid current profile achieved using the circuit of (a), including the two-pulse time structure described in the text. (c) Pressure versus time recorded from impact of the supersonic beam on a miniature microphone mounted in line-of-sight with the skimmed helium beam, showing a 155 μs FWHM gas pulse.

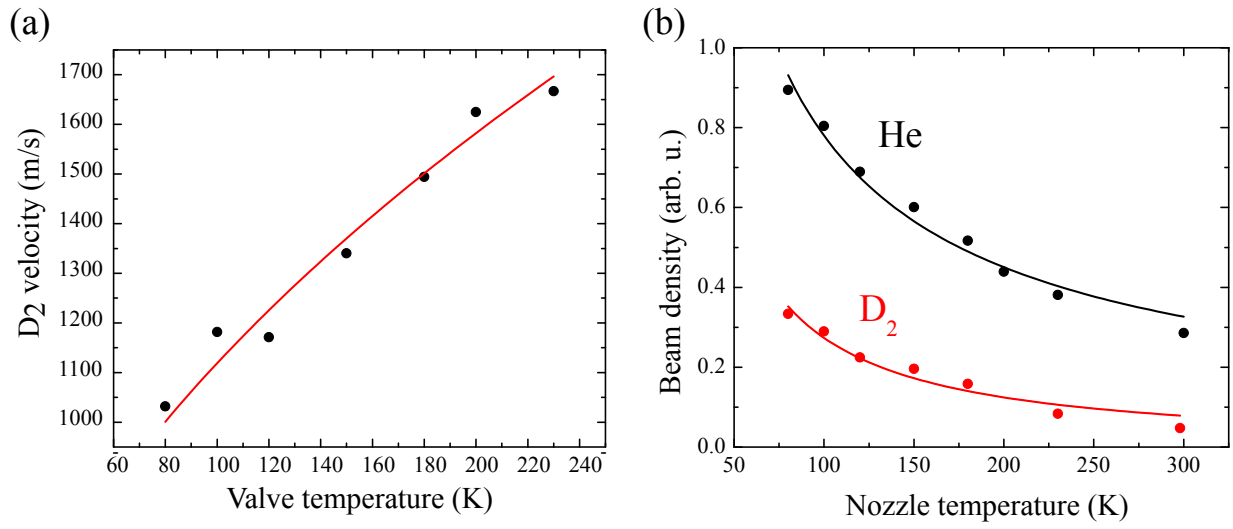

Figure 4.3: **Supersonic expansion performance of the cryogenic solenoid valve.** (a) Beam velocity versus valve temperature for D_2. (b) Relative density versus valve temperature for pulsed He and D_2 supersonic expansions.

transfer of that absolute scale to all other measurements. The resulting calibration is that the OH–He cross-section is 127 ± 18^2 at 250 K; all other cross-sections may be interpreted relative to this value. It should be emphasized that this sort of absolute calibration was only possible because the OH molecules were trapped.

A sample time-of-flight trace of the He packet's impact upon the trapped OH sample is shown in figure 4.5. There is a rapid loss of trapped OH over roughly a millisecond — longer than the He pulse's intrinsic duration, but only slightly more than a single trap oscillation period — and then the OH population remains effectively constant over the remainder of the time plotted. Even with the added gas load from the solenoid valve we observed trap lifetimes of over 50 ms, and so the prompt loss can safely be considered to be truly beam-trap collisions rather than loss due to multiply-scattered He or D_2 particles.

The results of these experiments are shown in figure 4.6, and prompt several conclusions. The strong drop in both the OH–He and OH–D_2 cross-sections below 90 cm^{-1} is suggestive of the closing of the $\left|J = \frac{5}{2}\right\rangle \leftarrow \left|J = \frac{3}{2}\right\rangle$ rotational-excitation channel in OH at 84 cm^{-1}. It should be noted that the absolute magnitude of the He–OH cross-section is more than a factor of 5 smaller than that of OH–D_2: we attribute this in part to the quadrupole moment possessed by $J = 1$ orthohydrogen, whose population is frozen into the supersonic expansion at roughly the room temperature 3:1 ratio with $J = 0$ parahydrogen. The quadrupole moment can interact with the OH dipole moment and therefore adds both strength and anisotropy to the scattering interaction.

There is also the apparent peak in the OH–D_2 cross-section near 305 cm^{-1} to consider. It is difficult to attribute a cause to it without substantial theoretical work, but it is suggestively located near the 300 cm^{-1} $J = 3 \leftarrow J = 1$ excitation in orthohydrogen.

4.2 OH–ND_3 collisions at 4 K

Prompted by the success of the OH–He/D_2 collision experiment and the impressive results then being demonstrated by buffer-gas cooling[77, 78], we began a collaboration with the group of John Doyle at Harvard University, and particularly with Dave Patterson. The goal of this collaboration was to use a buffer-gas cooled beam of deuterated ammonia, ND_3, to look for **dipolar** OH–ND_3 interactions at a 4 K collision energy[79, 67].

Figure 4.7 shows a sketch of the experimental setup for this experiment. OH molecules were decelerated and trapped as before — Stark deceleration is now a tool, rather than a research project. The new ingredients are the

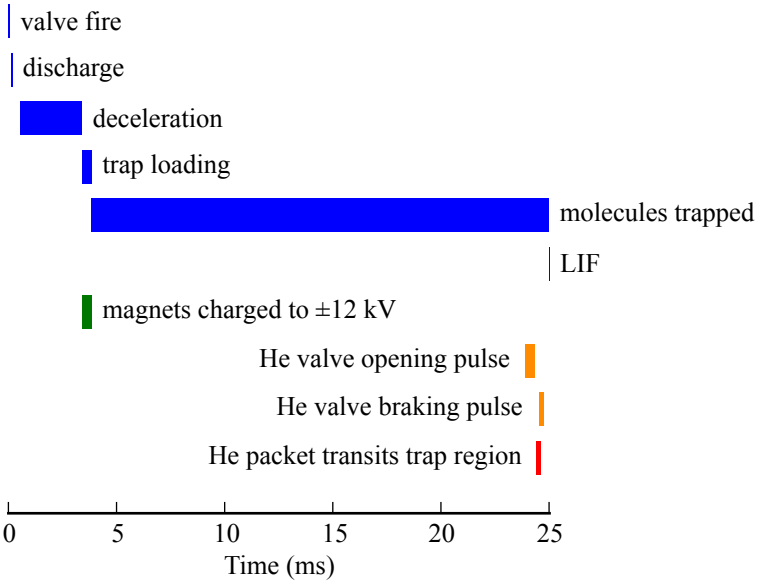

Figure 4.4: **Experimental sequence for OH–He and OH–D_2 collision experiments.**

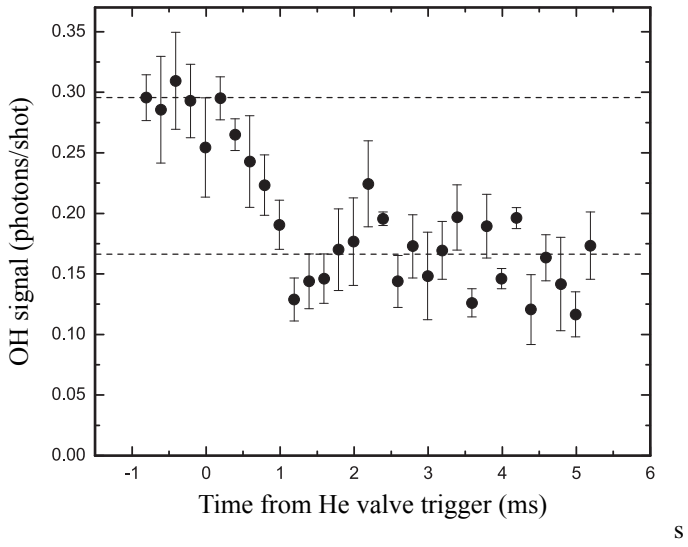

s

Figure 4.5: **OH fluorescence versus time showing the impact of a helium packet.** The collision promptly removes $\sim$47% of the trapped molecules, but there is no visible change in the background-gas collisional loss rate after the helium packet completes its transit through the trap.

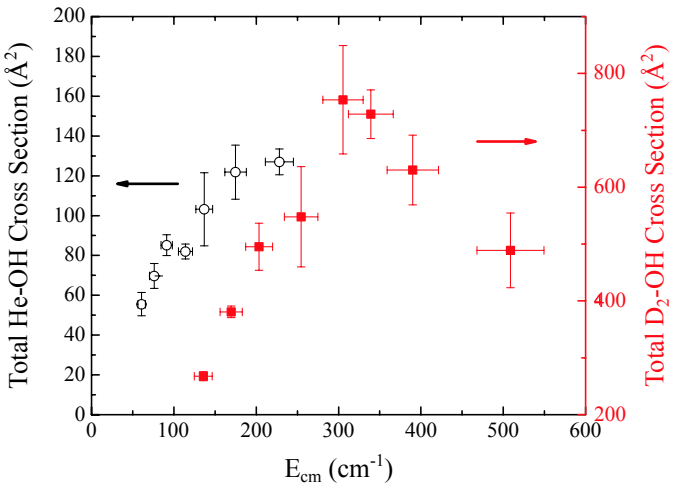

Figure 4.6: **Absolute OH–He and OH–D_2 trap-loss cross-sections versus collision energy.** Note that the *y*-axis scales differ between the two cases. Error bars are one standard error.

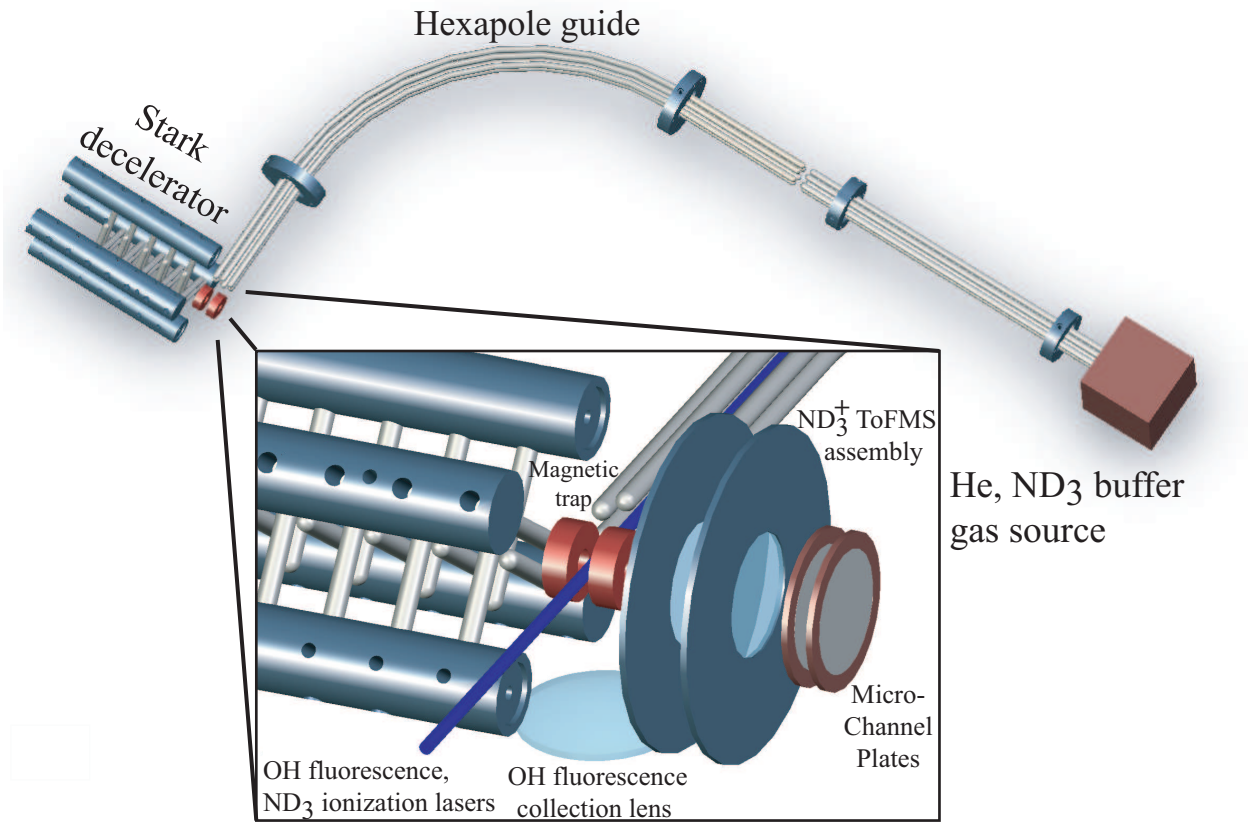

Figure 4.7: **Experimental system for OH–ND_3 collision experiment.** OH molecules are Stark-decelerated and loaded into the magnetic quadrupole trap, and then illuminated by the 4 K ND_3 molecular beam. This beam is formed by a capillary-filled buffer-gas cell, and then electrostatically guided around a 90° bend to separate it from the helium carrier gas and to provide a rapid turn-on/turn-off capability. The relative OH density in the trap is detected by laser-induced fluorescence; the absolute ND_3 beam density is determined by resonance-enhanced multiphoton ionization, calibrated against a hot-cathode ion gauge.

buffer-gas source producing a 4 K ND_3 beam and the REMPI detection system to measure the ND_3 beam density.

4.2.1 An introduction to buffer-gas cooling

The basic principle of buffer-gas cooling sounds trivial: cold, 4 K helium gas is mixed with some warm species X in a cell to produce a 4 K sample of X. If the cell has an opening in it, a beam of X in a helium carrier comes out (figure 4.8). Of course, the actual implementation has substantially more subtleties. In the limit of low helium density, the "beam" exits the cell effusively: there is no actual beam, just a flux of particles escaping with a thermal, isotropic momentum distribution. The downside is that since the X particles are transported diffusively, the fraction of the initial sample which actually exits the cell is very small. This fraction, usually termed the extraction efficiency, is just the ratio of the exit aperture area to the cell's total internal surface area — usually on the order of 0.1–1 percent.

At much higher helium densities, there exists a substantial pressure differential between the cell and the vacuum space outside it. In this case, the helium hydrodynamically entrains the X particles, and pulls a large fraction of them out the aperture. However, the trade-off is that the helium undergoes multiple collisions as it exits the cell, and forms a supersonic expansion. While this can yield internal state distributions even colder than the cell temperature, it also gives the beam a mean center-of-mass velocity on the order of 150 m/s.

In between the effusive and supersonic regimes, there exists a crossover region commonly referred to as the hydrodynamic regime. In this part of parameter space, there is enough helium density to entrain the X particles, but the density is low enough that the gas only undergoes a couple of collisions as it exits the cell. The result is a beam with a much smaller center-of-mass boost, but still good extraction efficiency.

4.2.2 Buffer-gas-cooled ND_3 and the challenges thereof

The ND_3 system operated most likely in the hydrodynamic regime. The helium flow rate of 3.5 sccm (that is, atm.-cm^3/minute; 1 sccm$= 4.4 \times 10^{17}$ molecules/s) is considered relatively low, while the cell aperture's large 6 mm diameter reduced the pressure differential. The mean velocity of the ND_3 beam after the bent-hexapole guide was 110 m/s (see figure 4.10). The forward velocity acceptance of the guide can be calculated using the guided species' maximum Stark shift and the guide's radius of curvature. For this guide with ± 5 kV and ND_3in its $|J = 1, K = 1\rangle$ state, we predicted a cutoff velocity of 150 m/s.

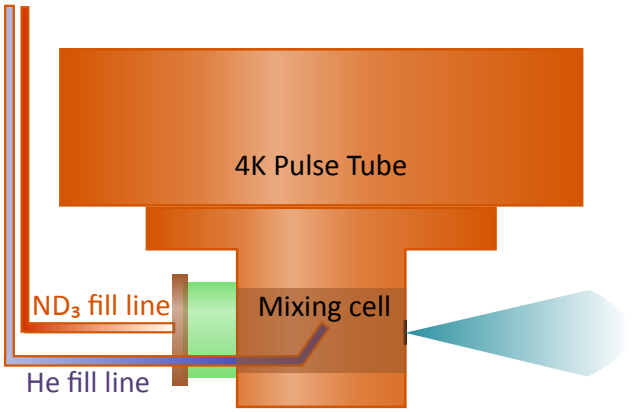

Figure 4.8: **Buffer-gas-cooled 4 K ND_3 beam source.** Warm (200–250 K) ND_3 gas flows down the central capillary fill line, and is mixed with 4 K helium to produce a beam of 4 K ND_3. The beam is guided by a hexapole (see figure 4.7) to separate the ND_3 from the helium carrier gas. The ND_3 fill line enters the cell through a G-10 fiberglass thermal standoff, allowing the line to be maintained at 250 K using only 200 mW of heater power. The fiberglass standoff is designed to maximize the path length from any 4 K surface to the tip of the ND_3 line and therefore maximize the run time available before an ice bridge is formed.

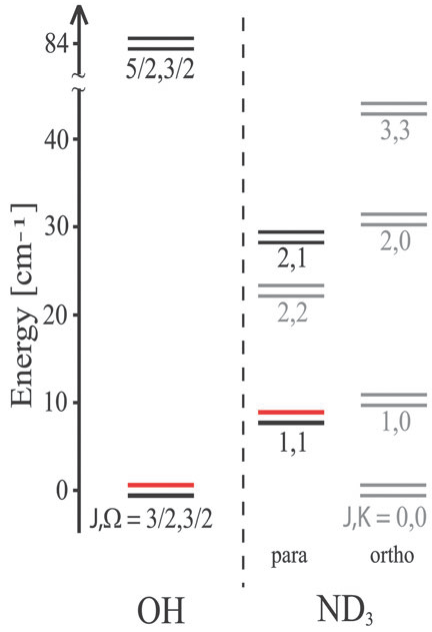

Figure 4.9: **The rotational and parity spectra of OH and ND_3.** The parity splittings are exaggerated for clarity. The red-highlighted parity states are those used for the collisions described in this section.

The Stark shift spectrum of ND_3 is qualitatively very similar to that of OH; both are shown in figure 4.9. ND_3 possesses a 1.5 D dipole moment, and a low-energy parity doubling of 1.5 GHz due to the so-called "umbrella-mode" inversion vibration. (The N atom can be either above or below the three D atoms, so the ground state consists of symmetric and antisymmetric combinations of the two possibilities. The splitting is set by the tunneling rate between the two possibilities — in NH_3, with its 2x lighter H atoms and exponentially higher tunneling rate, the splitting is 23.8 GHz.) As a symmetric-top molecule, ND_3 is characterized by three rotational quantum numbers, J, K, and M. J is the total angular momentum and M its projection on a laboratory space-fixed axis, as before. New, however, is the fact that ND_3 possesses two distinct moments of inertia. We define B as the rotational constant associated with rotation transverse to the 3-fold symmetry axis and C as the constant associated with rotation about the symmetry axis. This produces the rotational Hamiltonian

$$\begin{aligned}\mathscr{H}_{\text{rot}} &= B(\hat{J}_x^2+\hat{J}_y^2)+C\hat{J}_z^2 \\ &= B\mathbf{J}^2+(C-B)\hat{J}_z^2 \\ &= BJ(J+1)+(C-B)K^2\end{aligned}$$

where we define K as the projection quantum number of $\mathbf{J}$ along the three-fold symmetry axis of the ND_3 molecule.

Formally, the inversion doublet is the symmetric and antisymmetric combinations of $K=|K|$ and $K=-|K|$; $K=0$ states have no doublet. Since the rotational averaging term for symmetric top molecules for a dipole moment μ is

$$\mu_{\text{eff}}=\mu\frac{MK}{J(J+1)}$$

and K and M both vary between $-J$ and J, molecules in high-JK states are guided even more effectively than low-J molecules by an electrostatic guide. To separate the ND_3 from its He carrier and also to permit switching the beam on and off, we used a two-segment electrostatic hexapole guide. The first segment was a simple straight hexapole, consisting of six 3 mm diameter electropolished stainless steel rods with an inner diameter of 6 mm and running from 2 mm after the buffer-gas cell exit to a gate valve 20 cm away. The gate valve allowed the pulse tube cryostat to be isolated so that the helium released from the cryosorption pumps when the system warmed up did not contaminate the trap and decelerator vacua. The gate valve was custom built for us by the JILA instrument shop, and enabled us to minimize the gap between between the first and second hexapoles to only 3 mm. The second hexapole contained a 90°

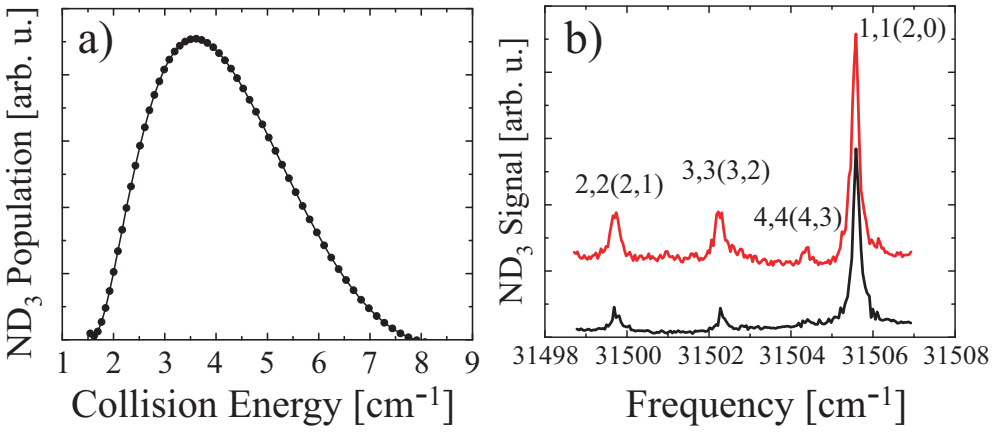

Figure 4.10: **ND_3 beam parameters.** (a) Relative density versus velocity, quoted as OH–ND_3 collision energy. (b) Rotational state distribution for two different buffer-gas flow rates: (upper, red) 2.0 sccm He and 2.5 sccm ND_3 and (lower, black) 3.5 sccm He and 1.0 sccm ND_3. The unparenthesized labels indicate the J and K quantum numbers of the ground rotational state probed by each line, while the parenthesized labels indicate (J, K) for the intermediate rotational state in the excited $\tilde{B}(v' = 5)$ level. Due to their lesser confinement within the hexapole guide, states with $K < J$ are not observed.

bend with a 13.5 cm radius of curvature and terminated 1 cm away from the center of the magnetic trap. This bend is what accomplished both the separation of the ND_3 from the buffer gas and the gating of the ND_3 beam.

Since the buffer-gas cell is fed by long, narrow gas lines, turning off the gas flows outside of the cryostat does not immediately cut off the molecular beam. Instead, the beam decays on a timescale of tens of seconds. However, without the electrostatic guide, effectively no ND_3 molecules are able to enter the trap chamber. With the guide off, there is no ND_3 to the sensitivity limit of our REMPI detection, and even with both the helium and ND_3 gas flows on there is no detectable change in the OH trap lifetime versus the pure background vacuum level.

The temporal gating ability of the hexapole guides allowed us to characterize the forward velocity distribution of the guided ND_3 beam. The guide was turned on for increasing lengths of time and the peak signal was measured. The derivative of this density-versus-guidance time curve yields the velocity profile of the beam, which is plotted in figure 4.10(a). (For computational simplicity, the measured curve was fit with a 6^{th} order polynomial, whose derivative is plotted here.) The rotational temperature of the beam was determined using REMPI spectroscopy. The relative strengths of the different rovibronic lines can be calculated using the Hönl-London factors; dividing the line strengths out yields the relative densities of the different ground rotational states and hence the rotational temperature. We found that the rotational temperature varied strongly with the gas flow rates. Unfortunately, the flow rates with

the highest absolute beam densities also possessed the highest rotational temperatures. Spectra of two different sets of flow rates, are plotted in figure 4.10(b). The final choice of a 1.0 sccm flow rate for ND_3 and 3.5 sccm for He was a compromise yielding a rotational temperature of 5.4 K and an acceptable beam intensity.

The majority of the technical effort involved in the OH–ND_3 experiment was spent on developing a **stable** buffer-gas source. While it took longer than expected to observe any hexapole-guided ND_3, a further fourteen months elapsed between the first guided signal and the beginning of the actual collision experiment. Those six months were spent trying to get the source to work for more than five minutes at a time.

The symptom we observed was that after some short period of running, there would occur a simultaneous spike in the cell temperature and in the ND_3 signal in both REMPI and on the residual-gas analyzer (RGA). As the RGA does not have a line-of-sight view of the guided beam, a pressure jump on it indicates a very large flux of unguided, warm ND_3. We went through several theories involving temperature/pressure oscillations in the helium fill line, insufficient cryosorption pumping speed, or poor thermalization of the helium to the cell, before this problem was solved. The true issue lies in the fact that ND_3 freezes at 195 K. Our original cells were simply too small: the cell filled with ammonia ice, and when the ice growth reached the (warm) ammonia fill line the ice flash-evaporated. This spiked the cell temperature, and released the observed large puff of both ammonia and helium. Moreover, if enough helium was released to thermally connect the 40 K radiation shield to the 4 K cryosorption pump plates, it is possible to get thermal runaway. The 'sorbs release their adsorbed helium as they warm up, which further increases the thermal conduction to the 40 K shield—a positive feedback loop which is only broken once the 'sorbs have released their entire helium load.

The solution to this icing problem is simple once it is understood: just make the cell bigger! While there are limits due to the in-cell gas dynamics (as described in section 4.2.1), up to a point increases in cell volume can be compensated by increasing the exit aperture size. Since there is no substantial loss to having the cell aperture match the hexapole guide aperture, we arrived at a 6 mm aperture and a cell with approximately 1 cm of free space on all sides of the ND_3 fill line.

4.2.3 Collision results and ND_3 density calibration

Once the properties of the ND_3 beam were understood, the actual collision experiment was undertaken. The sequence for each shot (illustrated in figure 4.11) was similar to that of the OH–He experiment. OH molecules

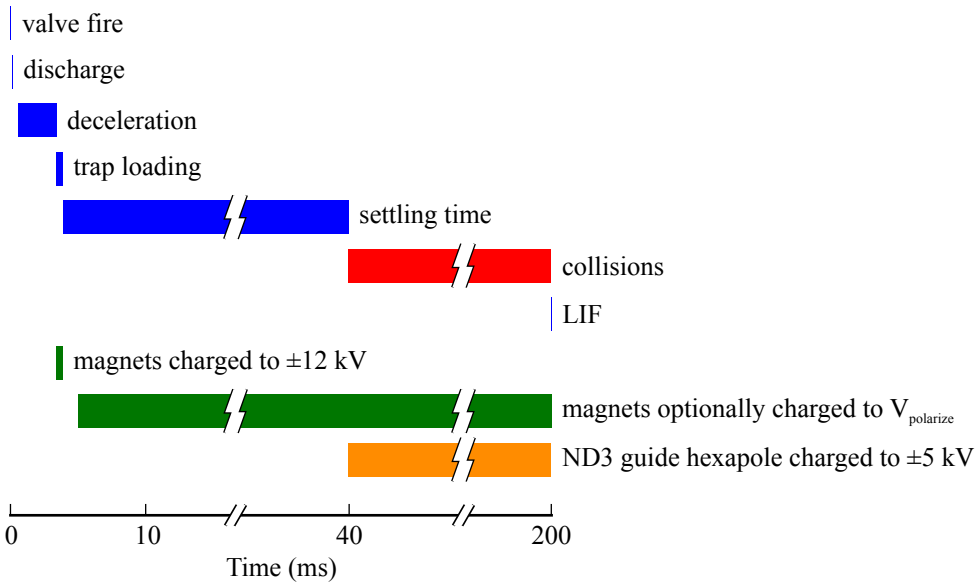

Figure 4.11: **Experimental sequence for OH–ND_3 collision experiment.**

were Stark decelerated and trapped, then allowed to settle. If a polarizing field was applied, it was turned on at the beginning of the settling period, as well. After ~ 25 ms of settling time, the ND_3 guide was turned on for durations of up to 160 ms and the relative OH population was measured as a function of time to yield a one-body loss rate Γ_{on}. The difference between Γ_{on} and the loss rate with the ND_3 beam turned off (Γ_{off}) gives the collisional loss rate due to OH–ND_3 scattering. Each experimental shot measured the relative number after a single period of ND_3 bombardment; many shots were averaged together and the bombardment duration was varied shot-to-shot to build op the number-versus-time curve. A fresh baseline (ND_3 off) curve was taken each day, since the vacuum quality appears to vary on timescales of a day or two. A typical pair of lifetime curves with the ND_3 beam off and on is shown in figure 4.12

While the OH-ND_3 collision **rate** is easy to measure, it is much more complicated to convert that to a true cross-section. Just as with the OH–He experiment, a method to determine the true density of the impinging ND_3 beam is required. Since REMPI has large systematic uncertainties related to laser mode shape, absolute ionization efficiency, and ion extraction and detection efficiency, REMPI ion signals must be calibrated against some standard. For this experiment, we again turned to an ionization gauge as the reference standard.

The scheme for calibrating the ND_3 beam density is shown schematically in figure 4.13. Each day, a pair of ND_3 off and ND_3 on collision measurements were performed, with the pulsed dye laser using Rhodamine 6G dye and tuned to 282 nm for laser-induced fluorescence detection of OH. Then, working quickly so that the buffer-gas cell did not accumulate too much ice before the density could be calibrated, we swapped a different set of dye cuvettes into the laser (this time using DCM Special, a functionalized variant of the normal DCM with increased solubility in methanol) and retuned the laser to produce 317 nm light for REMPI. An $f = 30$ cm final focus lens was inserted into the beam path and the laser was realigned to go through the magnetic trap.

Extracting ions across the enormous magnetic field gradients in the permanent magnet trap required large acceleration voltages so that the ion cyclotron period of $\sim 1\,\mu$s was much longer than the time required for the ions to escape the trap region. We applied a +950 V voltage pulse to the decelerator-side magnet (while keeping the the downstream magnet grounded) to push ND_3^+ ions out of the trap and into a time-of-flight mass spectrometer (TOFMS). The TOFMS consisted of a pair of grids held at a uniform potential of -1.1 kV to create a 2 cm free drift region, before the ions are detected on a pair of chevron-oriented microchannel plates. To block stray electric fields (due to charging of dielectric surfaces by electrons or ions emitted by the Stark decelerator), the drift region was fully enclosed in

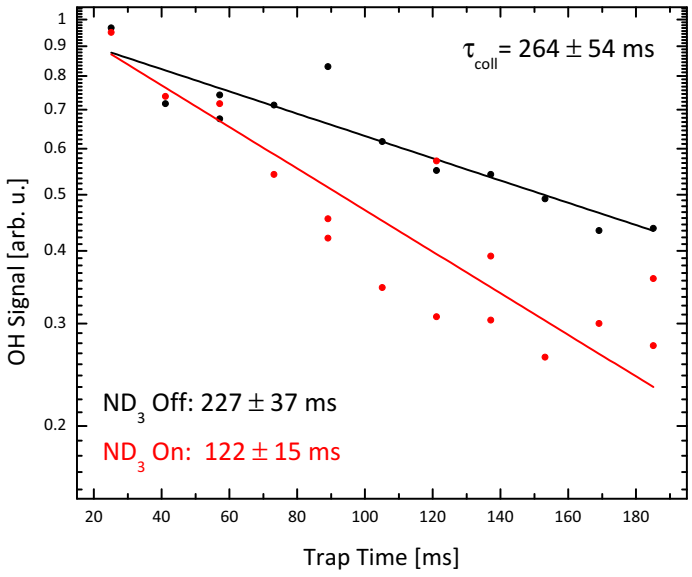

Figure 4.12: **OH fluorescence versus time showing the effect of the ND_3 beam.** The black points are a plot of number versus time with no impinging ND_3, while the red points are with the ND_3 beam illuminating the trapped OH molecules. Solid lines are one-body loss-rate fits to the data; quoted uncertainties are one standard error.

a metal tube; a metal ground shield was also mounted to the (plastic) support part for the downstream magnet, and electrically tied to that magnet. The +950 V extraction voltage was only pulsed on **after** the laser ionization step, so that the ionization would occur with parity being a good quantum number. Since the $\tilde{B}$ state in ammonia possesses planar symmetry, its **vibrational** levels alternate in parity. Therefore, in the absence of an electric field, the two ground-state umbrella-mode parity states connect to different, spectroscopically-resolved $\tilde{B}$, v' levels. We wanted to measure the density of only one parity level, so it was important to ensure that there was no contamination by the opposite parity due to an electric field. (The ND_3 guide hexapole was also turned off immediately prior to the ionization laser trigger.)

Once the laser was aligned, the ion signal due to the cold ND_3 beam was measured. The gate valve was then closed, and a precision leak valve was used to back-fill the trap chamber to achieve an equal ion signal. It took several tens of minutes for the ND_3 density to stabilize, since the gas needed to re-passivate the chamber walls versus proton exchange (which converts ND_3 to ND_xH_{3-x}); a similar passivation was performed every day on the buffer-gas cell before cooling it to 4 K. When the ND_3 density as measured by the RGA was stable and the ion signal level was well-matched to that recorded from the buffer-gas-cooled beam, a series of measurements of the exact RGA reading and ion signals were taken; these measurements were used to determine the local calibration between ion signal and RGA-measured density. It was important to only perform this calibration using very similar ion currents, because the multichannel plate is susceptible to both ion saturation and gain shifts due to the background pressure.

While REMPI is a spectroscopically-selective technique, at room temperature the REMPI spectrum of ND_3 suffers a great deal of spectral confusion as can be seen in figure 4.14. At a 5 K rotational temperature, it is certain that the entire ion signal from the buffer-gas-cooled beam is due to the population in the $|J = 1, K = 1\rangle$ state. At 295 K, however, that is not true. Spectral simulations (detailed in chapter 4 of [67]) indicate that only 16% of the 295 K ion signal is due to the $|1, 1\rangle$ state. Correcting for this line-strength factor and using the Boltzmann distribution to determine the the relative fraction in the weak-field-seeking $|1, 1\rangle$ state then gives the final density calibration factor.

The final results of the collision experiments are shown in figure 4.15. Two sets of cross-section measurements were taken: electric-field-free, and with an electric field large enough to polarize both OH and ND_3. The polarizing case consists of two different electric field configurations: one with the magnets themselves charged, and one where the ground-screen behind the downstream magnet mount had electrically disconnected and was therefore floating at a substantial voltage. (This was determined by the appearance of strong-field-seeker lines in the buffer-gas-cooled beam

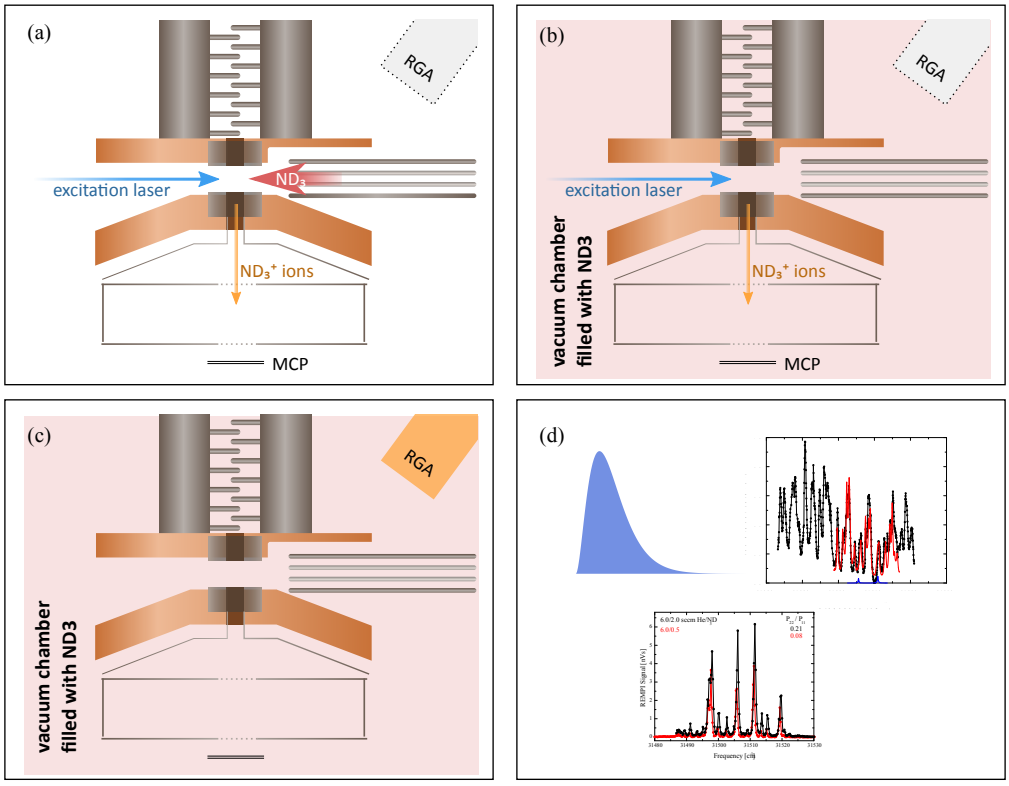

Figure 4.13: **ND_3 density calibration sequence.** (a) The REMPI ion signal of the guided 4 K beam is measured. (b) The guide is turned off, and the chamber is filled with room-temperature ND_3 gas to a sufficient density as to reproduce the REMPI ion signal. (c) The density of the room-temperature ND_3 gas is measured using a residual gas analyzer calibrated against a Bayard-Alpert type ionization gauge. (d) The true density of the guided beam is calculated using the results of (a)–(c) combined with calculated spectroscopic overlap factors, the RGA gas-correction factor, and the Boltzmann distribution.

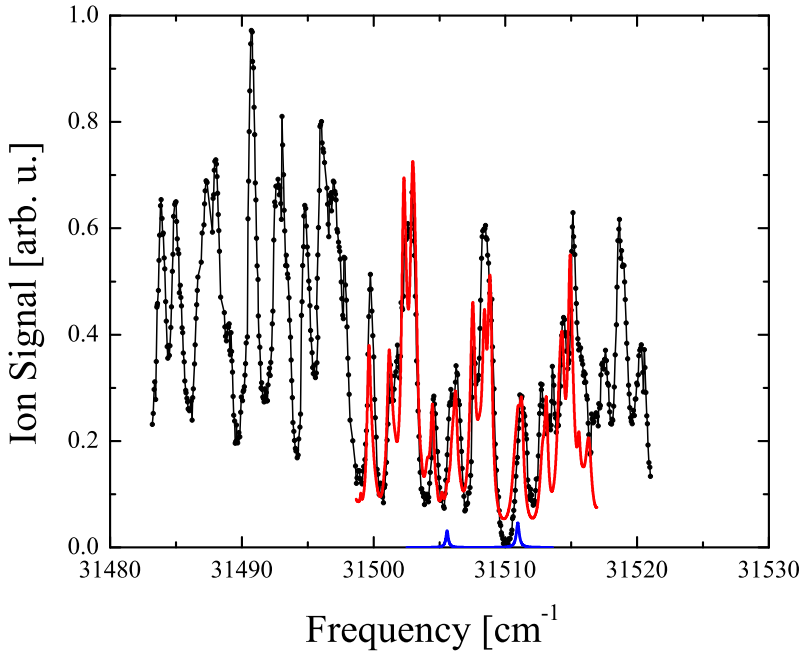

Figure 4.14: **The REMPI spectrum of ND_3 at 295 K.** Solid red line is a model fit from [79, 67]. Solid blue line denotes the calculated contribution to the line strength from the $|J, K\rangle = |1, 1\rangle$ state used in the collision experiments.

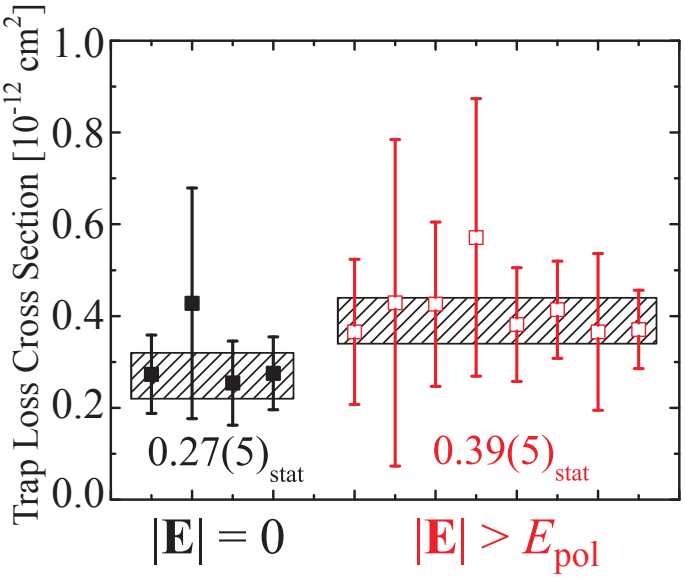

Figure 4.15: **OH–ND_3 trap loss cross-sections without and with a polarizing electric field.** The combined average cross-sections are stated in black (unpolarized) and red (polarized) text below their respective data points.

spectrum. Since the hexapole efficiently rejects strong-field-seeking molecules, any ionization through those line must be due to an electric field breaking parity symmetry. With a correction due to the different Franck-Condon factors for the different $\tilde{B}, v'$ levels, the relative strengths of the strong- and weak-field-seeking $|J', K'\rangle \leftarrow |J'', K''\rangle$ lines indicate the fractional parity state mixing and therefore the actual electric field.)

The two different electrically polarized conditions yield cross-sections in excellent agreement with each other, while the unpolarized case is 2σ (stat) lower. The absolute magnitudes of the cross-sections are in reasonable agreement with theory[79], although the corrections required to determine the (measurable) trap-loss cross-section from the true differential elastic and inelastic cross-sections are large.

Chapter 5

Microwave manipulation of trapped OH

The success of the OH–ND_3 collision experiment prompted us to turn our attention to taking control of the internal state of the trapped OH molecules. In particular, a look at a pure Zeeman spectrum of OH suggests that just as the $\left|f;\frac{3}{2}\right\rangle$ state is magnetically trappable, so too should be the $\left|e;\frac{3}{2}\right\rangle$ state. The collisions of section §4.2 were performed with OH in $\left|f;\frac{3}{2}\right\rangle$ and ND_3 in the weak-field-seeking parity of its $|J,K\rangle = |1,1\rangle$ inversion doublet. The OH Λ-doublet is split by 1.67 GHz, while the ND_3 inversion doublet is split by 1.5 GHz. This near-resonance suggests that the collision of OH and ND_3 molecules in opposite parity states could have a substantial resonant enhancement, due to the near-elasticity of the parity-swap (i. e. flip both parities) channel.

Since 1.67 GHz is a easy frequency to generate, the obvious way of controlling the OH state is to directly drive the electric-dipole-allowed Λ-doublet transition. While some technical ingenuity was required (see section §5.3) to couple the microwaves to the molecules, this can be made to work very well. Unfortunately, the trap dynamics of $\left|e;\frac{3}{2}\right\rangle$ molecules are much less simple than suggested above when electric fields are added to the magnetic trapping field — as one would wish to do to enable dipolar collisions, for instance.

5.1 Avoided crossings in mixed electric and magnetic fields

While the combination of electric and magnetic dipoles enables fascinating new phenomena, it also comes with substantial complications. In particular, simple linear Zeeman spectra are converted to tangles of interwoven avoided crossings by the application of transverse electric fields, even at strengths much smaller than the full polarizing field. In this chapter, I report the experimental observation of these crossings in the polar radical OH and their dramatic impact on dynamics in a magnetic trap. In its $^2\Pi_{3/2}$ ground electronic state, stationary OH has a magnetic dipole

moment of $2\mu_B$ (where μ_B is the Bohr magneton) and an electric moment of 1.67 D (0.65 a. u.); rotational averaging reduces each of these in the laboratory frame to $\mu_i^{(eff)} = \mu_i \frac{M\bar{\Omega}}{J(J+1)}$, where J is the total angular momentum, M is its lab-fixed projection, and $\bar{\Omega}$ is the magnitude of J's projection on the internuclear axis. Each rotational level of OH contains two Zeeman manifolds of opposite parity, $|e;M\rangle$ and $|f;M\rangle$; with no applied fields, these states are split by a Λ-doublet coupling of 1.667 GHz. In an applied electric field, $|e\rangle$ and $|f\rangle$ are not strictly good quantum numbers. However, they are still useful as labels of a state's Stark character: $|e\rangle$ states are strong-electric-field-seeking while $|f\rangle$ states are weak-field-seeking.

A representative Hamiltonian for Λ-doublet molecules in mixed electric and magnetic fields has been derived in [58] and was presented in section §2.3. While realistic systems must be solved numerically, the basic structure of the combined $H_{total} = H_{zero-field} + H_{Stark} + H_{Zeeman}$ Hamiltonian is simple: the zero-field part generates diagonal matrix elements in a suitable basis (e. g. the Hund's case a fine-structure plus parity basis $\left|JM\bar{\Omega}\varepsilon\right\rangle$ for OH, where $\varepsilon = e$ or f is the J-relative parity label), as does the Zeeman part if one takes the space-fixed Z axis to lie along the magnetic field $\vec{B}$. The off-diagonal elements are then purely from the Stark portion. The component of the electric field $\vec{E}$ parallel to $\vec{B}$ generates matrix elements which preserve M and change the parity ε, while the transverse components change M by ± 1 as well as ε. As can be seen in the Zeeman spectrum of OH (Fig. 5.1(a)), all states in the lower parity manifold except for the absolute ground state have Zeeman-induced crossings with one or more of the upper parity states: in an E-field, these real crossings are coupled by the off-diagonal Stark elements and become avoided. Working in the perturbative limit, the crossings X_M of Fig. 5.1 have widths $\delta_{+1/2} \propto |E \sin\theta_{EB}|$, $\delta_{-1/2} \propto \left|E^3 \sin^2\theta_{EB}\cos\theta_{EB}\right|$, and $\delta_{-3/2} \propto \left|E^3 \sin^3\theta_{EB}\right|$, where θ_{EB} is the angle between $\vec{E}$ and $\vec{B}$. Since the off-diagonal elements only couple states of opposite parity, the total perturbation theory order must be *odd*: crossings with total ΔM *even* such as $X_{-1/2}$ require one extra $\Delta M = 0$ coupling order so that the total coupling changes ε as it must. M-changing couplings have a $\sin\theta_{EB}$ dependence, while M-preserving couplings go as $\cos\theta_{EB}$, so this leads to a $(\sin\theta_{EB})^{\Delta M}\cos\theta_{EB}$ angular dependence in the coupling strengths for these even crossings, while the angular dependence for crossings with ΔM odd is simply $(\sin\theta_{EB})^{\Delta M}$. Perturbation theory begins to fail, however, at relatively small E-fields (much smaller than the polarizing E-field at zero B-field) because of the strength of the electric dipole coupling and the fact that the Zeeman crossings are gapless at zero E-field. Therefore, for all calculations described in this chapter we diagonalize the full 8×8 ground state fine-structure Hamiltonian of OH described in section §2.3 and also in [67].

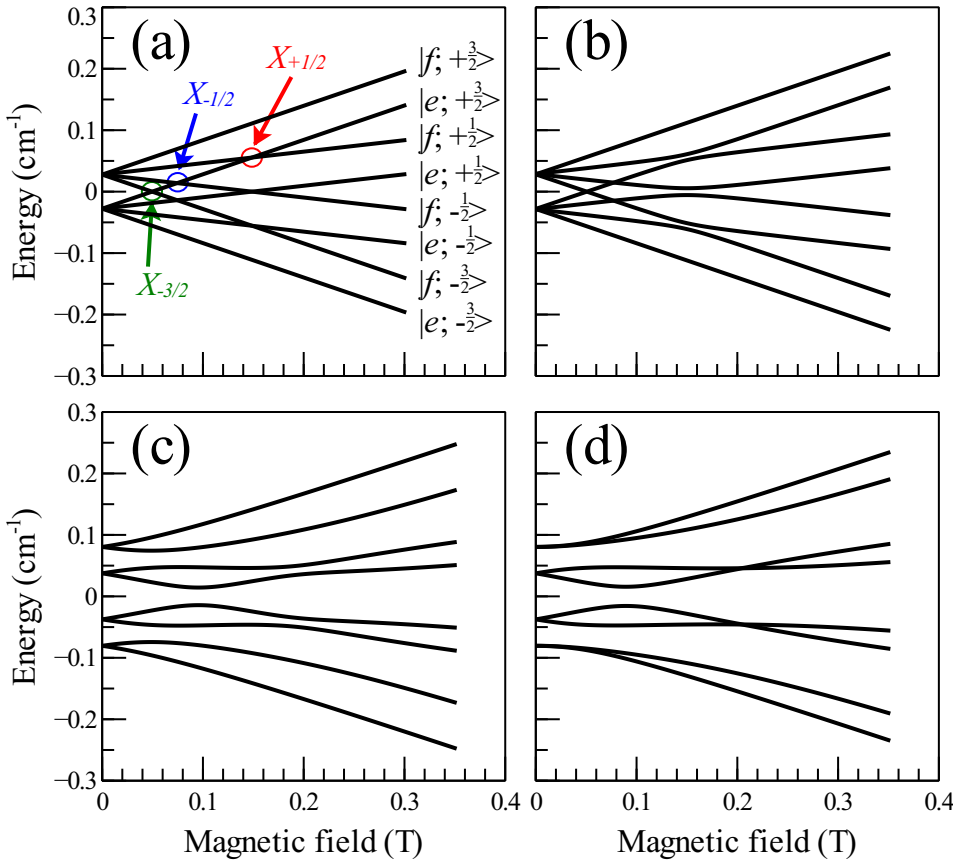

Figure 5.1: **The Zeeman structure of OH with bias electric fields**. (a) 0 V/cm, (b) 500 V/cm at a 90° magnetic-to-electric field angle θ_{EB}, (c) 5000 V/cm at 65°, and (d) 5000 V/cm at 90°. The crossings X_M of the $\left|e;+\frac{3}{2}\right\rangle$ state with the three $\left|f;M=\{-\frac{3}{2},-\frac{1}{2},+\frac{1}{2}\}\right\rangle$ states are labeled in (a).

We observe these avoided crossings by their dynamical effects on a sample of magnetically trapped OH molecules. Our Stark deceleration and magnetic trapping system has been described elsewhere [61]. Briefly, OH molecules are created in an electric discharge through water vapor in a supersonic expansion and then Stark decelerated and brought to rest in a permanent magnetic quadrupole trap (Fig. 5.2(a)) at a temperature of ~ 70 mK, in their $\left|f;+\frac{3}{2}\right\rangle$ state. By applying chirped microwave fields to the trap magnet surfaces, we can then transfer the trapped molecules to the $\left|e;+\frac{3}{2}\right\rangle$ state, wherein we can probe the three crossings labeled in Fig. 5.1(a); application of a DC voltage to the magnets results in a bias E-field with the distribution shown in Fig. 5.2(b). The spatial loci of the three crossings in the actual field gradient of our trap are shown in Fig. 5.2(c). The multiple-well structure is a result of our use of permanent magnets: the hole in the center of the magnets allows flux to exit both inside and outside the magnet ring, yielding a toroidal field minimum between the faces of the magnet, as well as the central quadrupole trap. The distribution of θ_{EB} angles generated by charging the magnets is plotted in Fig. 5.2(d).

5.2 Trap losses from Landau-Zener transitions

As our trapped molecules are moving at velocities $\lesssim 10$ m/s, only a very small energy gap ($\delta \sim 10^{-5}$ cm^{-1}) is needed for each molecule to have some chance of following the adiabats rather than the diabats of the potential surfaces. As can be seen in Fig. 5.1, the adiabats of all the levels below the "doubly-stretched" $\left|f;+\frac{3}{2}\right\rangle$ state are substantially less trapped than the $\left|e;+\frac{3}{2}\right\rangle$ diabat – or in some cases, are outright antitrapped. Thus, if molecules are transferred to the $\left|e;+\frac{3}{2}\right\rangle$ diabat in zero field and then a bias field is applied, some fraction of the molecules will leak out of the trap as they follow the adiabats rather than Landau-Zener hopping [80] to follow the trap diabat. At low fields, the Landau-Zener hopping probability is still substantial, and so it takes multiple trap oscillations for a molecule to leak out. At higher fields, however, effectively all molecules follow the adiabats and so the loss rate is simply limited by the trap dynamical time $\tau_{dyn} = \frac{1}{4}\nu_{trap}^{-1}$ where ν_{trap} is the trap oscillation frequency.

In order to transfer population from $\left|f;+\frac{3}{2}\right\rangle$ to $\left|e;+\frac{3}{2}\right\rangle$, we use an Adiabatic Rapid Passage (ARP) technique [81] via microwave fields applied directly to the trap magnets. As the magnets also experience ± 14 kV potentials as part of the trap loading sequence, the microwave system is AC-coupled to the trap by a pair of in-vacuum high voltage capacitors as described in section §5.3. This capacitive coupling stage isolates the microwave system by roughly 40 dBV from the ± 14 kV magnet bias; two 1.2 GHz high-pass filters further block both the residual (few-volt) near-DC

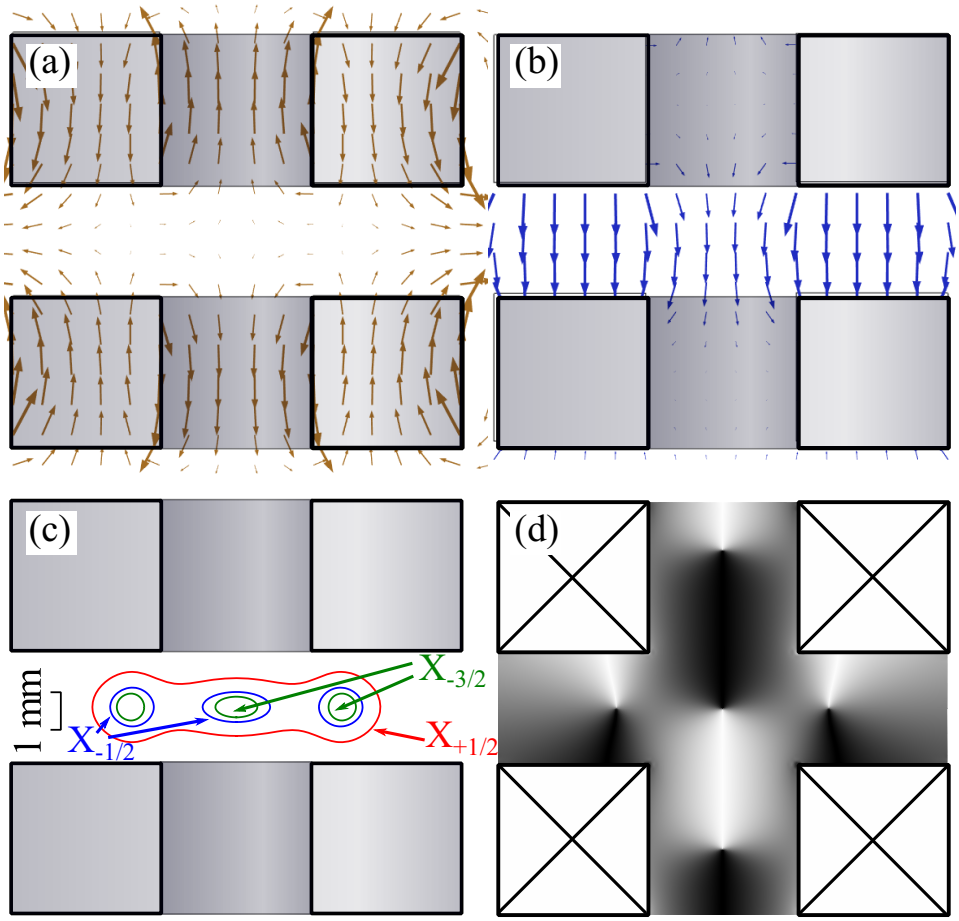

Figure 5.2: **Magnetic trap geometry relevant to microwave control of OH.** To scale. (a) The magnetic field distribution in the permanent magnet quadrupole trap. (b). The electric field distribution created by applying a potential difference to the trap magnets. (c) The spatial location of the avoided crossings X_M. (d) The relative angle θ_{EB} between electric and magnetic fields in the trap. White denotes 0° while black denotes 180°, implying that the avoided crossings are widest in the gray regions.

bias and the switching transients from the microwave. By chirping our microwave frequency through the entire range of differential Zeeman shifts [82] in our trap over a period $\tau_{ARP} \ll \tau_{dyn}$, we are able to achieve transfer of $\sim 75\,\%$ of the observable trap population. (Since the transfer is a π transition, only the fraction of $\vec{E}_{RF} \parallel \vec{B}$ is useful. Thus, molecules in the gray regions of Fig. 5.2(d) see much smaller effective intensities than molecules in the white or black regions.)

In addition to causing dynamical trap loss, the avoided crossings X_M also reduce the efficiency of our ARP pulses: in the vicinity of the avoided crossings, not only are the states shifted away from the nominal 1.667 GHz transition frequency, but also the two parity states are mixed by the electric field. The net result of this mixing is that molecules transferred near said crossings may not in fact be transferred to the $\left|e;+\frac{3}{2}\right\rangle$ diabat but rather may end up on the $|f;M\rangle$ diabat and thus be invisible to our state-selective detection. Figure 5.3 displays the $\left|e;+\frac{3}{2}\right\rangle$ population as a function of the DC bias field applied during the ARP. The bias field leads to a rapid drop in transferred population as the $\left|f;+\frac{3}{2}\right\rangle \rightarrow \left|e;+\frac{3}{2}\right\rangle$ transition is Stark-shifted out of resonance; the bias field required for this shift increases with the frequency width of the ARP pulse. We have performed simulations using a numerical solution of the optical Bloch equations to calculate a position dependent ARP transfer probability with zero electric field. We then calculate the position-dependent Stark-Zeeman shift by diagonalizing the OH Hamiltonian and convolve the resulting frequency distribution with the ARP bandwidth to determine the total fraction transferred. The simulation results shown in Fig. 5.3 give a good match to the population measurements, showing that the ARP process is well-understood; a more detailed description of the simulation code is given in section §5.4. The simulations suggest the presence of a stray E-field in the trap region on the order of 100–150 $\mathrm{V/cm}$.

Applied E-fields also have a profound effect on trap dynamics. A loss of $\sim 40\%$ of the e-state population over τ_{dyn} is observed immediately after the ARP pulse (Fig. 5.3 inset), almost certainly due to prompt loss of molecules following an adiabat through the $X_{+1/2}$ crossing (which is fully avoided in just the observed stray E-field) and exiting the trap. At larger bias fields, loss rates up to τ_{dyn}^{-1} are observed with critical fields again on the order of 200-300 V/cm, corresponding to a unit probability of loss through either $X_{-1/2}$ or $X_{-3/2}$. The observed loss rates (Fig. 5.4(a)) are well-fit by a probabilistic model

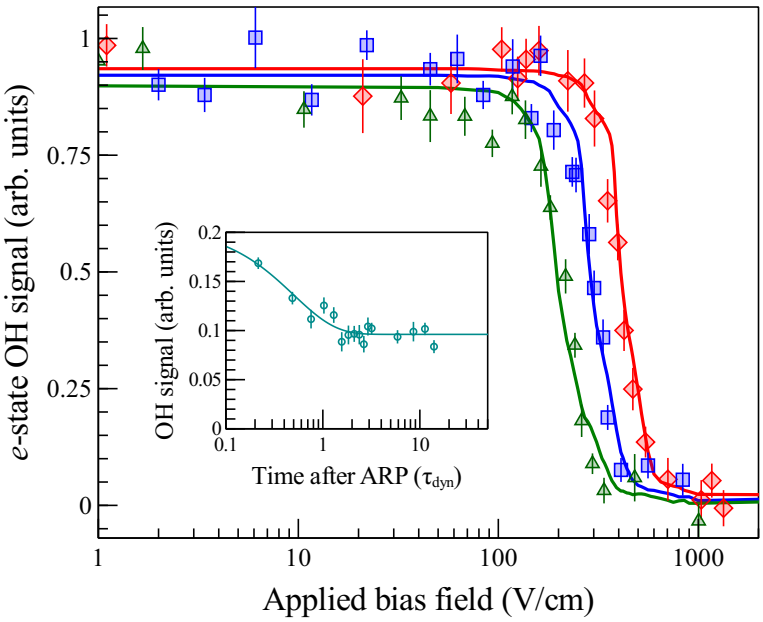

Figure 5.3: **Post-ARP *e*-state population versus applied bias field**. ARP chirp widths of 10 (green triangles), 20 (blue squares), and 40 MHz (red diamond). Solid lines are Monte-Carlo simulations of the population transfer using realistic bias and RF field distributions from finite-element calculations, a semiclassical treatment of the Stark detunings, and a homogeneous stray field as a free parameter. (inset) Time-of-flight of *e*-state population immediately after ARP, with no applied bias field. The rapid loss through the $X_{+1/2}$ crossing is clearly visible: the solid line is a fit to a single-exponential loss at a rate of τ_{dyn}^{-1}.

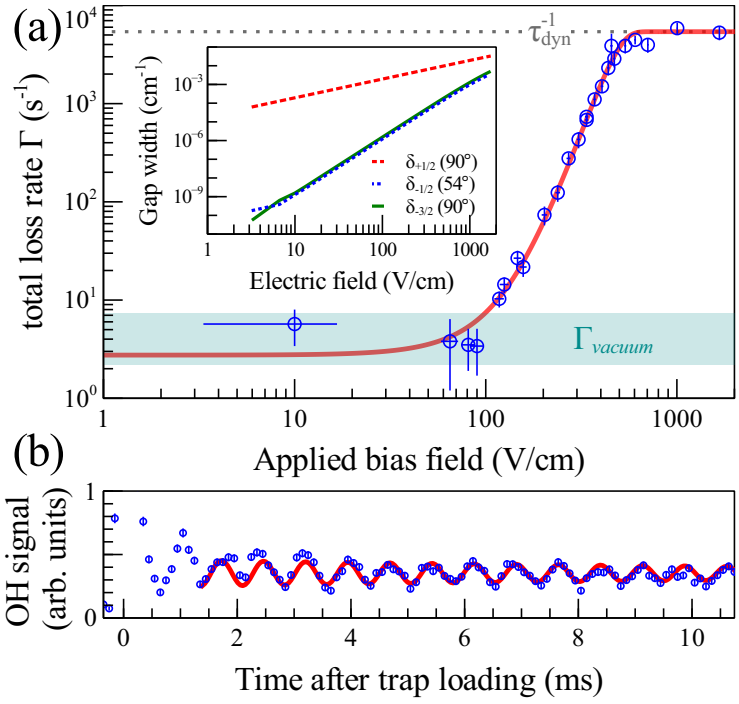

Figure 5.4: **Landau-Zener loss dynamics of magnetically trapped $\left|\mathbf{e};\mathbf{M}=+\frac{3}{2}\right\rangle$ OH molecules.** (a) Loss rate of $\left|e;M=+\frac{3}{2}\right\rangle$ molecules versus applied electric field. The solid red line is a fit to a simple Landau-Zener model; the green shaded stripe denotes the range of observed loss rates for $\left|f;+\frac{3}{2}\right\rangle$ molecules. The bias field is turned on 5 ms after the ARP pulse is completed, and thus well after the prompt loss seen in the inset of Fig. 5.3 is completed. (inset) Widths δ_M of the avoided crossings between $\left|e;+\frac{3}{2}\right\rangle$ and $|f;M\rangle$ versus applied electric field, at their respectively maximizing values of θ_{EB}. $\delta_{+1/2}$ is linear with field, while $\delta_{-1/2}$ and $\delta_{-3/2}$ are cubic. (b) Time-of-flight trace of trap oscillations, observed by loading the trap with a non-zero center-of-mass velocity. The solid red fit yields a trap frequency $\nu_{trap} = 1350$ Hz.

$$\Gamma \quad = \quad \Gamma_{vacuum} + \tau_{dyn}^{-1} \times \left(1 - \prod_{M \in \{-\frac{3}{2}, -\frac{1}{2}\}} \mathscr{P}_{LZ}^{(M)} \right)$$

where Γ_{vacuum} is the background vacuum loss rate and

$$\mathscr{P}_{LZ}^{(M)} \quad = \quad \exp\left(-\frac{2\pi\xi \left\langle \delta_M^2 \left(E_{eff} \right) \right\rangle}{\hbar \left(\Delta\mu_{eff}(M) \right) \left\langle \frac{dB}{dt} \right\rangle} \right)$$

is the Landau-Zener probability that the molecule stays on the $\left| e; +\frac{3}{2} \right\rangle$ diabat through the crossing X_M. Angle brackets denote population averages: $\left\langle \frac{dB}{dt} \right\rangle = \left\langle \vec{\nabla} B \cdot \vec{v} \right\rangle$ is the rate of change of the magnetic field and $\left\langle \delta_M \left(E_{eff} \right) \right\rangle = \left\langle \delta_M \left(\sqrt{E^2 + E_{stray}^2} \right) \right\rangle$ is the width of the crossing X_M as a function of applied electric field E and stray field E_{stray}, while $\Delta\mu_{eff}(M) = \left(\frac{3/2 \cdot 3/2}{3/2 \cdot 5/2} - \frac{3/2 \cdot M}{3/2 \cdot 5/2} \right) \cdot 2\mu_B$ is the difference between the effective magnetic moments of the $\left| f; +\frac{3}{2} \right\rangle$ and $|e; M\rangle$ states. The model contains only 3 free parameters: Γ_{vacuum}, E_{stray}, and $\xi \approx 0.17$, which incorporates the errors in our estimates of the population-averaged parameters. (While we can estimate $\left\langle \frac{dB}{dt} \right\rangle$ reasonably well from Monte-Carlo trap dynamics simulations, $\left\langle \delta_M \left(E_{eff} \right) \right\rangle$ has a very fast variation with $\langle \theta_{EB} \rangle$ and so is hard to accurately calculate or population-average. It is therefore responsible for most of ξ's deviation from unity.) Although we happened to observe experimental agreement between the visible trap oscillation frequency ν_{trap} and $4\tau_{dyn}^{-1}$ (Fig. 5.4(b)), our magnetic quadrupole trap's coupling of oscillation magnitude and frequency means that these two quantities would not necessarily have to be equal in every experimental realization. Γ_{vacuum} can be independently observed from the f-state lifetime, while E_{stray} can be derived from Fig. 5.3; both of these independent measurements are consistent with the fit. As both $\delta_{-1/2}$ and $\delta_{-3/2}$ are third-order in E, the most striking feature of the Landau-Zener model is that it explains the extremely steep rise in Γ: $\Gamma \sim 1 - \exp\left(-\alpha E^6\right)$ where α represents the Landau-Zener parameters.

The success of this model prompts two conclusions. The first is that magnetic trapping of the lower parity doublet in any molecule is fraught with difficulties: in OH, even just the fields from stray charge accumulating on the trap mounts is enough to cause unity loss through the $X_{+1/2}$ channel. (We are currently implementing a new trap mount design to minimize the patch charges in our future work.) In general, if one wishes to explore polar radicals in mixed fields in any states except the doubly-stretched ones, either optical trapping or an Ioffe-Pritchard trap with a sufficiently large offset B-field as to be above all the crossings is necessary; this implies that polar radicals in their lower parity doublet are extremely challenging candidates for slowing with a magnetic coilgun [83, 84]. More broadly, in precision measurement applications it is imperative to take a close look [85] at the exact Stark-Zeeman spectrum

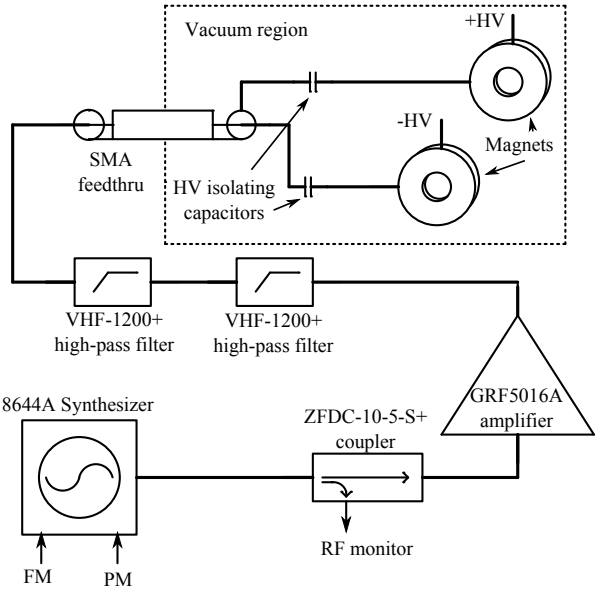

Figure 5.5: **A schematic of the microwave system use to transfer OH between Λ-doublet levels.**

of the system of interest, as the spectral distortions from the avoided crossings can persist over very large ranges in magnetic field.

5.3 Microwave coupling circuit design

In order to couple microwave power on to our trap magnets while protecting the microwave system from the ± 14 kV applied to the magnets during the trap loading sequence, we use a pair of custom in-vacuum capacitors to block the DC high voltage plus two more high-pass filters (Mini-Circuits VHF-1200+[1]) to block the AC transients generated by the magnet switching.

The microwave system layout is depicted in figure 5.5. Tunable microwave power is generated by an HP 8644A synthesizer, which is programmed to form the ARP pulse by voltages supplied to its frequency and pulse modulation inputs. A Mini-Circuits ZFDC-10-5-S+ directional coupler allows monitoring of the microwave signal before it is amplified by a GTC GRF5016A power amplifier. The microwaves are then coupled through the protection filters and into the vacuum system via an SMA feedthrough. Typical power levels are 30.4–35.4 dBm (1–3 W) at the feedthrough. As the ARP chirp time τ_{ARP} must be much shorter than τ_{dyn}, τ_{ARP} is generally between 20 and 80 μs.

[1] Manufacturer and part names are listed for completeness only and do not constitute an endorsement by NIST.

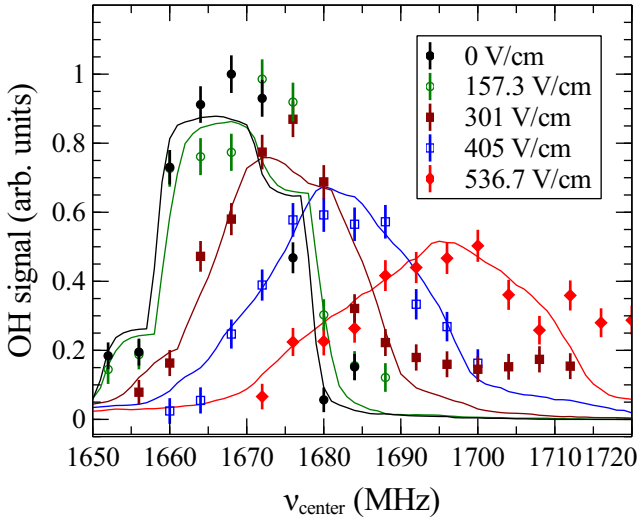

Figure 5.6: **ARP spectra at several different bias *E*-fields.** Points are data while solid lines are simulation results. The Stark-Zeeman broadening due to the avoided crossings is clearly visible.

5.4 Numerical simulations of ARP

As mentioned in section §5.2, we have performed numerical simulations of the ARP population dynamics. The simulation code works as follows:

(1) For each molecule in a Monte Carlo distribution, the optical Bloch equations are solved using the local magnitude of the microwave field (the microwave field is assumed to follow the DC field distribution generated by charging the magnet surfaces) and its angle against the local magnetic field. Both field distributions were calculated using a finite-element package. The final probability of the molecule transferring to the lower Λ-doublet state is then recorded.

(2) For each molecule, the local static *E*-field is calculated and then combined with the local *B*-field to find the total Stark-Zeeman detuning. This yields a transfer probability density as a function of microwave frequency.

(3) The probability density function is then integrated over the range of frequencies the ARP chirp sweeps through to get a final transfer probability.

Figure 5.6 shows several ARP spectra at different bias *E*-fields. The agreement between data (points) and simulation (solid lines) is good; in particular, the simulations capture the Stark-Zeeman broadening visible at larger fields. In

a homogeneous field and the absence of avoided crossings, the application of an E-field would merely push the two Λ-doublet states apart without broadening the transition. The field in the trap region is not fully homogeneous, which contributes some broadening, while the curvature of the $\left|e; M = +\frac{3}{2}\right\rangle$ state near its avoided crossings further increases the Stark-Zeeman broadening. In order to fit the simulations to the data, a background stray E-field on the order of 120 V/cm was required, consistent with the field required for the Landau-Zener model.

Chapter 6

OH–OH inelastic collisions

6.1 Two-body loss of $|f\rangle$-state molecules

With the recognition that $|e;\frac{3}{2}\rangle$ molecules cannot be magnetically trapped in the presence of an electric field, our goal of observing mixed-parity OH–ND_3 collisions turned towards using $|f;\frac{3}{2}\rangle$molecules and somehow parity-flipping the ND_3 molecules as they fly into the magnetic trap. What we observed, however, was that in the presence of a DC electric field, even $|f;\frac{3}{2}\rangle$ molecules experienced loss from the trap. We had seen this previously, while doing the original OH–ND_3 experiment, but as the loss terminated after some tens of milliseconds, we simply conducted the collision experiment after the trap population had time to resettle after the application of the polarizing field.

Now, however, we undertook to more closely examine the phenomenon and realized that it appeared to have a two-body loss profile. In the presence of a pure two-body loss rate, the total number $\mathcal{N}$ obeys a differential equation

$$\frac{d\mathcal{N}}{dt} = -\beta\mathcal{N}^2$$

which has the solution

$$\mathcal{N}(t) = \frac{\mathcal{N}_0}{1+\beta\mathcal{N}_0 t}$$

where $\mathcal{N}_0 = \mathcal{N}(0)$ is the initial number. For two-body losses which are fast compared to any other loss rates, this form is sufficient. When, however, the timescale $\beta\mathcal{N}_0$ is comparable to the one-body loss rate Γ it becomes necessary to use a combined one- and two-body loss model

$$\frac{d\mathcal{N}}{dt} = -\beta\mathcal{N}^2 - \Gamma\mathcal{N}$$

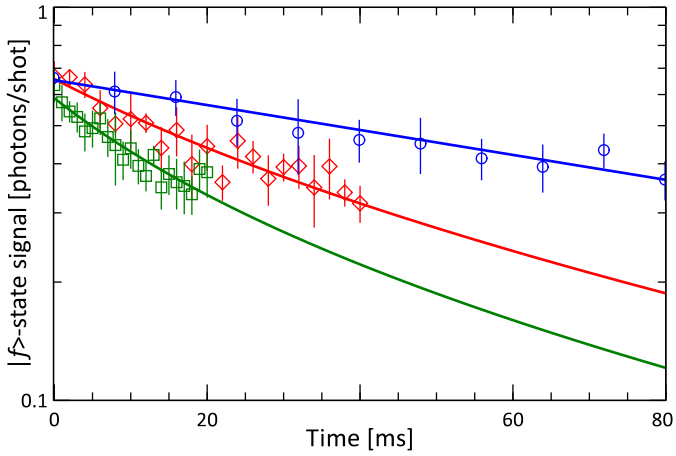

Figure 6.1: **Two-body loss of magnetically trapped OH molecules.** A comparison of pure one-body loss with zero electric field (blue circles), and two different two-body rates with 1500 V/cm (red diamonds) and 3000 V/cm (green squares) applied fields. The solid lines are fits to the data: pure one-body loss for the zero-field curve, and combined one- and two-body loss (using the zero-field one-body rate) for the two non-zero-field curves. Error bars are one statistical standard error.

or

$$\mathscr{N}(t) = \frac{\Gamma \mathscr{N}_0}{(\Gamma + \beta \mathscr{N}_0)\, e^{\Gamma t} - \beta \mathscr{N}_0}$$

.

Of course, the above only holds true in the case of a flat density distribution: if the density is spatially-varying, the local density $n(\vec{x},t)$ must be substituted for $\mathscr{N}(t)$. At the simplest level, this implies that two-body loss will selectively remove particles from the region of maximum density. However, if the sample is in thermal equilibrium and β is independent of collision-energy, the density distribution will remain self-similar. In this case, the use of $\mathscr{N}$ to describe the entire distribution will remain approximately correct, although the resulting β will be an effective averaged value rather than the true microscopic loss rate constant.

Figure 6.1 shows some representative results of our two-body loss experiments. OH molecules are magnetically trapped, allowed to settle for a few milliseconds, and then a DC bias electric field is applied between the trap magnets. The bias field of strengths of $\lesssim 10$ kV/cm are not enough to substantially distort the effective trap potential: loading the magnetic trap involves fields of over 60 kV/cm. It is clear from the figure, however, that applying an electric field has a profound effect upon the evolution of the trapped molecules. Moreover, the curvature of the number-vs.-time curve is inconsistent with one-body loss.

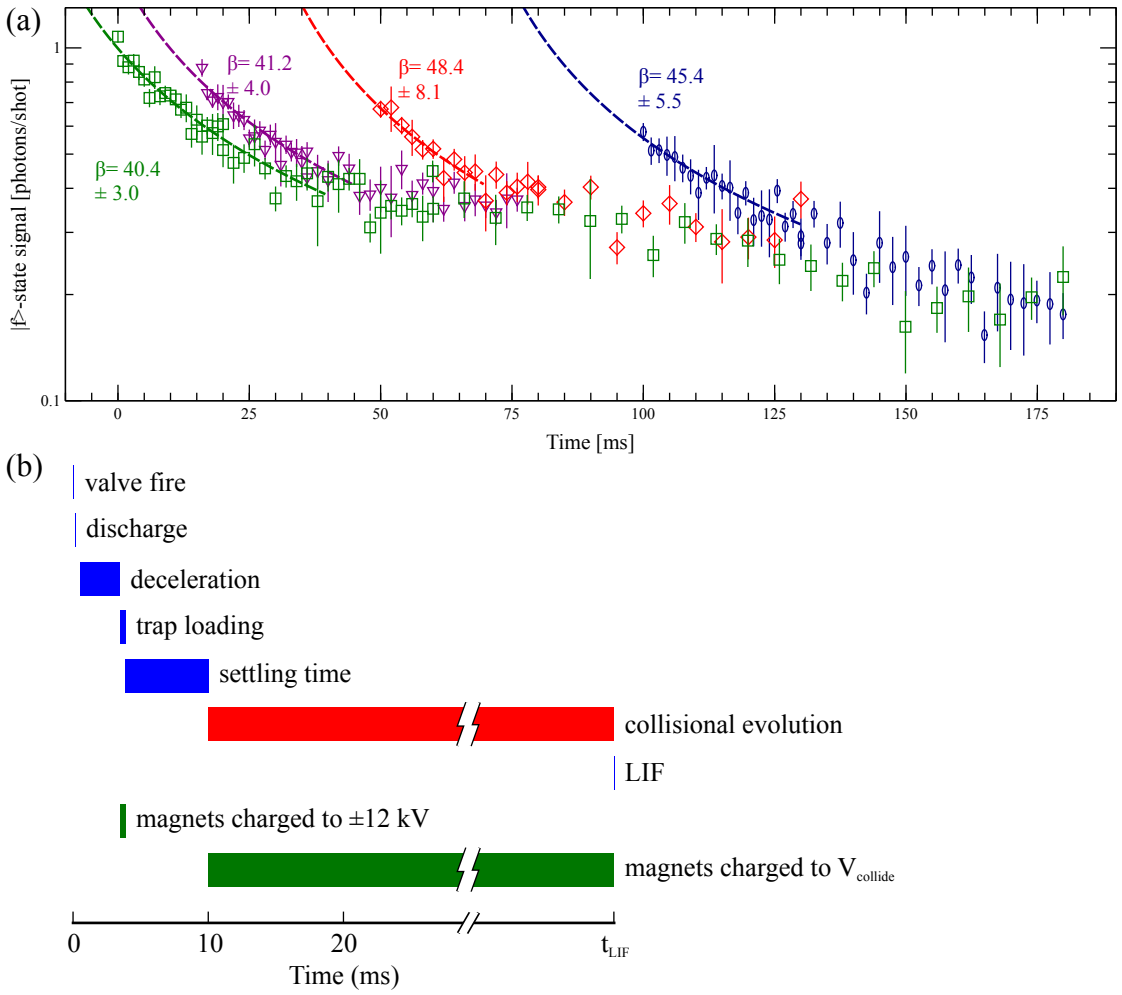

Figure 6.2: **Testing two-body loss by varying the starting density.** (a) Four sets of number-versus-time measurements, with different initial densities due to one-body losses before beginning the measurement. A 3000 V/cm DC electric field was turned on at $t = t_0^i$, where t_0^i is the time of the first point for each series. All four measurements yield statistically consistent two-body rate constants. Error bars are one statistical standard error. (b) A schematic timeline of the experiments.

A second, more formal test of the two-body nature of the losses is shown in figure 6.2. By delaying the turn-on time of the DC bias field, the initial density at the onset of two-body losses is varied. For four different densities over a factor of two in total number we observe statistically consistent values of β while the slopes on a semi-logarithmic plot are clearly different.

By independently measuring the zero-electric-field one-body loss rate (due to collisions with background gas), it is possible in principle to use the combined one- and two-body loss equation to measure two-body rates almost as low as the one-body loss rate. However, as will be described in the following section, vacuum loss is not the only one-body loss rate in the problem.

6.2 Electric-field dependence of the loss rate

In order to attain an understanding of the inelastic collision phenomena, the most obvious parameter to vary is the electric field strength. A large set of measurements were taken over three distinct epochs of data, separated by vacuum breaks and realignments of the LIF optics. The changed optics alignments cause the starting signal level to be different between the three eras, and therefore the β value; to combine the three data sets, the 3040 V/cm points were taken as a fixed reference, and two of the three data sets were linearly scaled so that their 3040 V/cm points matched the third data set. 3040 V/cm is an ideal matching point, because β is large enough to have good statistical uncertainty but the field is small enough that E-field-induced one-body losses are still (hopefully) fractionally small. The combined data are plotted in figure 6.3

It is also possible to plot β as a function of the induced dipole moment,

$$\mu = \frac{d^2\varepsilon}{\sqrt{(d\varepsilon)^2 + (\frac{\Delta}{2})^2}}$$

where $d = 1.67$ D is the total dipole moment of OH, ε is the electric field strength, and Δ is the Λ-doublet splitting. The result of this scaling is shown in figure 6.4. With this scaling, there is a clear change in behavior as the dipole moment saturates: at $\mu \lesssim 0.9$ D, β scales roughly as μ^2, while at higher μ the slope rapidly steepens.

This abrupt change in character around $\mu \approx 0.9$ D ($E \approx 3500$ V/cm) suggests that two-body loss may not be the whole story: the loss rate continues to increase with electric field, even though the dipole moment is saturating. Theory suggests that the two-body rate should be a pure (although potentially complex) function of the dipole moment—

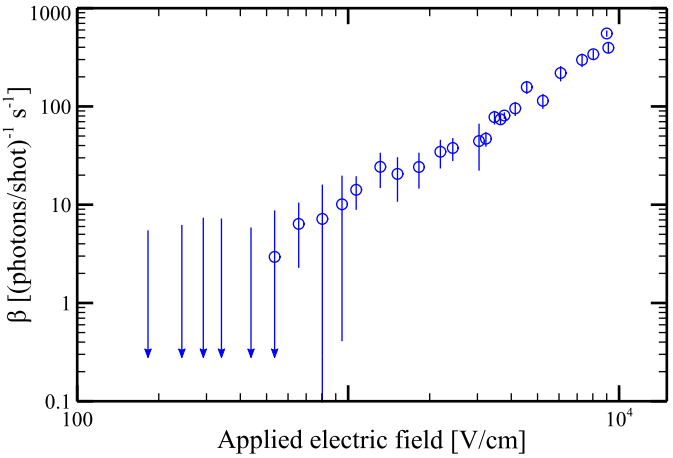

Figure 6.3: **Variation of the fitted two-body rate constant β with applied electric field.** Arrows indicate that the error bars are consistent with a zero rate constant; error bars without points indicate upper bounds. Error bars are one standard error.

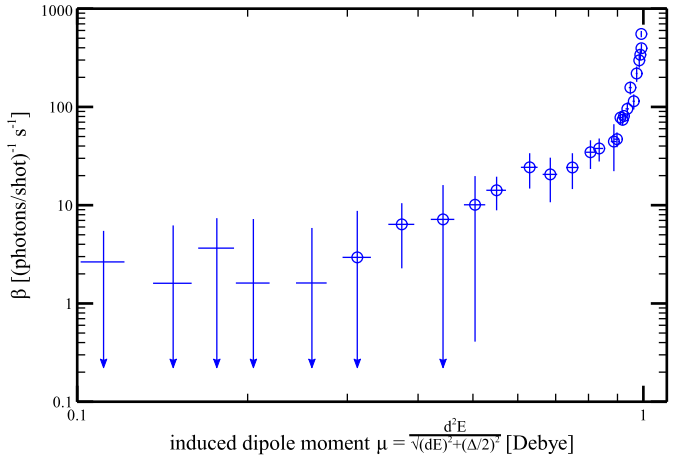

Figure 6.4: **Variation of the fitted two-body loss rate constant β with induced dipole moment.** This is the same data as figure 6.3, but with the electric field parametrized as the effective dipole moment μ given the maximum available dipole moment d, the electric field E, and the Λ-doublet splitting Δ. Arrows indicate that the error bars are consistent with a zero rate constant; the five points of lowest μ are presented as upper bounds rather than specific points. The point of highest μ is at a field of 9200 V/cm. Error bars are one standard error.

perhaps there is another one-body loss rate contaminating the fits?

An examination of the two highest potential surfaces of OH molecules in a uniform electric field superimposed over a quadrupole magnetic field (figure 6.5) reveals a fascinating structure. At large values of E, there is a very narrow avoided crossing between the surfaces at $\vec{B} \perp \vec{E}$ and small B. Just as changes in the direction of $\vec{B}$ can cause Majorana loss in very small magnetic fields, here small changes in θ_{EB} can allow molecules to Landau-Zener hop from the upper-most, trapped state to the lower, untrapped state. We can apply the Landau-Zener formula $P_{LZ}(r) = e^{-2\pi\Gamma(r)}$ with

$$\Gamma(r) = \frac{\delta(E, B(r), \theta_{EB} = \frac{\pi}{2})^2}{\hbar(\frac{1}{r} v_\vartheta)(d\delta/d\theta_{EB}|_{r,\frac{\pi}{2}})}$$

where $\delta(E, B(r), \theta_{EB})$ is the splitting between the two surfaces at the radial coordinate r and v_ϑ is the azimuthal velocity of the molecule. To determine an absolute loss rate γ, we can then integrate the probability function P_{LZ} over the molecular Boltzmann distribution:

$$\gamma_{\mathrm{LZ}} = \int_0^\infty 4\pi r^2 n_{\mathrm{r}}(r)\, dr \int_0^\infty \frac{1}{\pi}\frac{v_\vartheta}{r} \cdot e^{-2\pi\Gamma(r)} \cdot \frac{1}{Z} e^{-\frac{mv_\vartheta^2}{2k_B T}}\, dv_\vartheta$$

where $n_{\mathrm{r}}(r)$ is the 3-dimensional relative density, $Z = \int_0^\infty e^{-\frac{mv_\vartheta^2}{2k_B T}}\, dv_\vartheta$ is the partition function, m is the molecular mass, k_B is Boltzmann's constant, and T is the temperature. The factor $\frac{1}{\pi}\frac{v_\vartheta}{r}$ occurs because each molecule encounters $\theta_{EB} = \frac{\pi}{2} + n\pi$ twice per orbit. For a quadrupole magnetic trap of gradient B' in the $\hat{r}$ direction,

$$n_{\mathrm{r}}(r) = \frac{1}{Z_n} e^{-\frac{\mu_m B' r}{k_B T}}$$

with

$$Z_n = \int_0^\infty 4\pi r^2 e^{-\frac{\mu_m B' r}{k_B T}}\, dr$$

.

Given a calculable Landau-Zener loss rate, the collision data can then be refitted to deconvolve the added one-body loss rate. By numerically integrating over a 45 mK thermal distribution and assuming a 1 T/cm gradient in the direction parallel to the plane $\theta_{EB} = 90°$, I calculate the Landau-Zener rates shown in figure 6.6.

Unfortunately, while the integral is not difficult, it is difficult to assign a systematic confidence interval to this sort of simplistic theory. For this work, I take an uncertainty factor rather than an absolute range: I assume that the calculation is correct to within a factor of two in either direction. Deconvolution of the calculated Landau-Zener loss

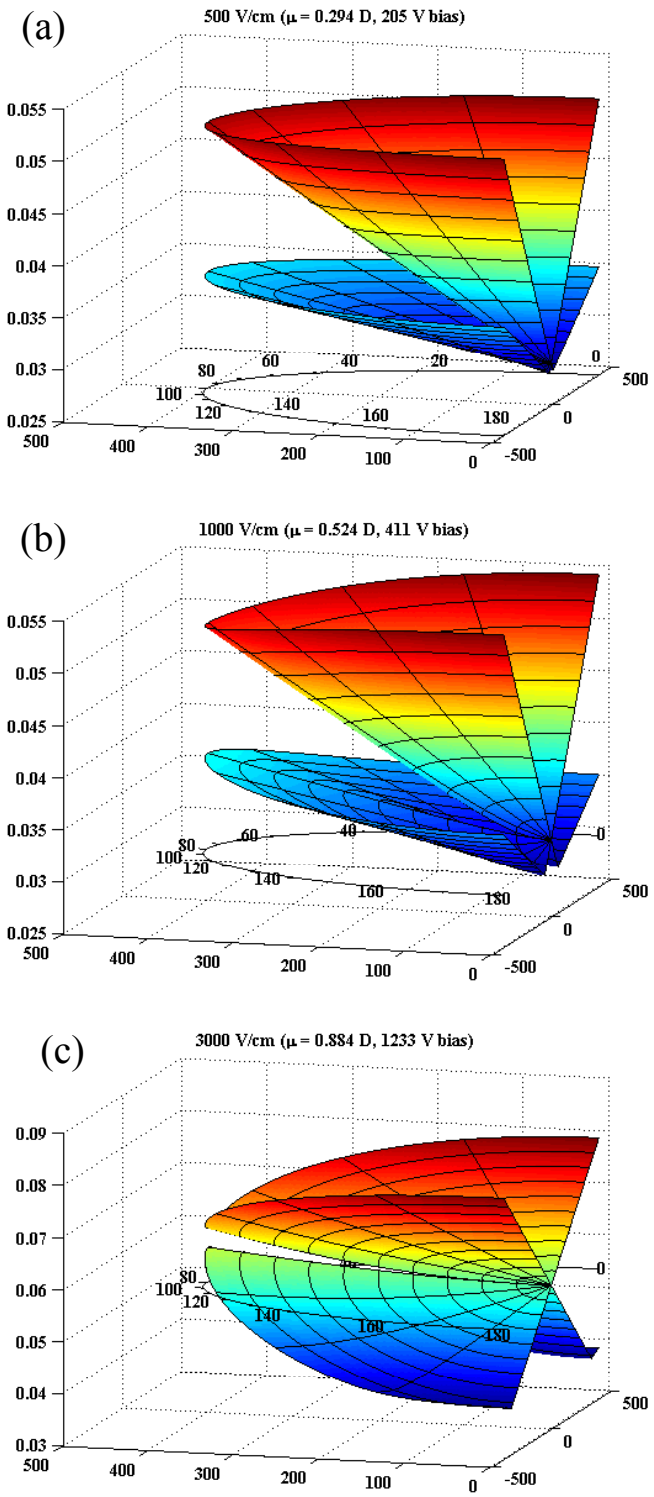

Figure 6.5: **The two uppermost potential surfaces of OH in mixed E and B fields.** The radial coordinate is the magnetic field strength in Gauss, and the angular coordinate is θ_{EB}, the angle between $\vec{E}$ and $\vec{B}$. Electric field strengths are (a) 500 V/cm, (b) 1000 V/cm, and (c) 3000 V/cm. Note the classical Landau-Zener shape near 90° at the larger electric field strengths.

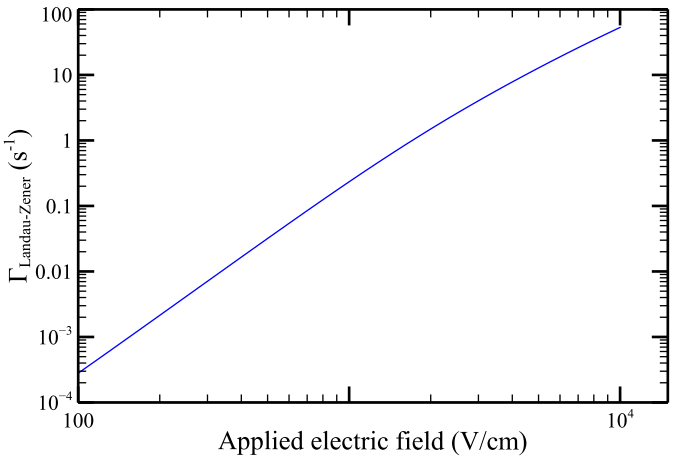

Figure 6.6: $|f\rangle$**-state Landau-Zener loss rates versus electric field.**

rate — that is, using the combination of one-body loss rates

$$\Gamma = \gamma_{\mathrm{LZ}} + \gamma_{\mathrm{vacuum}}$$

yields the two-body rates shown in figure 6.7. The upturn at high induced dipole moment μ is much less pronounced when the Landau-Zener losses are removed. In fact, if one supposes that the calculation underestimates the Landau-Zener rate by a factor of two (the lower limit of the shaded blue regions in figure 6.7), the fitted β actually levels off at high electric fields and fits a single, rather than broken, power law.

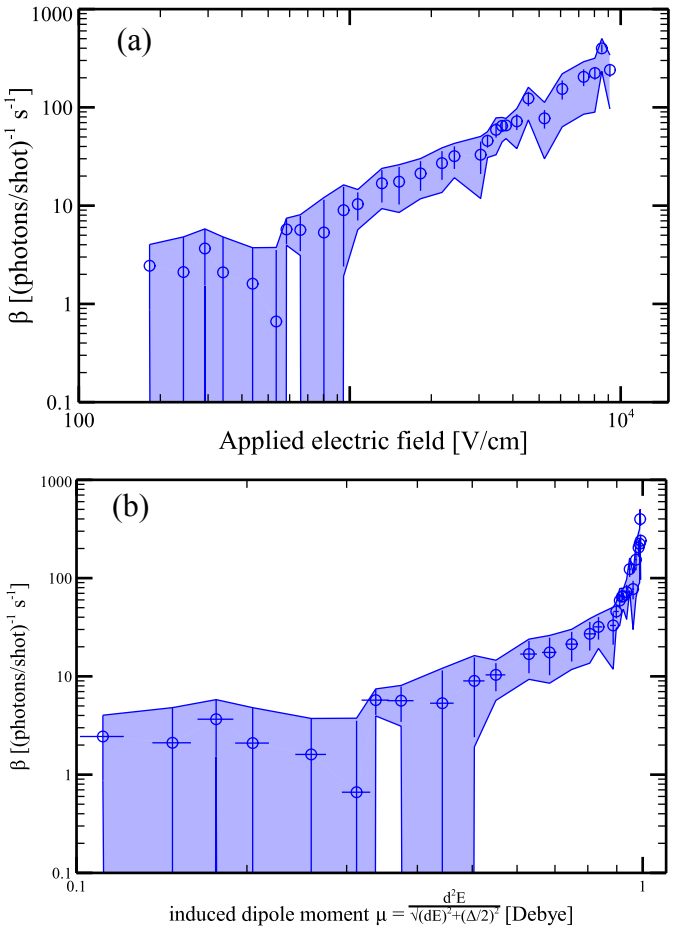

Figure 6.7: **Variation of the two-body loss constant β after deconvolution of the Landau-Zener losses.** (a) Variation with electric field. (b) Variation with induced dipole moment. Blue shaded regions indicate the values of β found by varying the Landau-Zener loss rate by a factor of 2 up or down. Smaller values of the Landau-Zener rate produce larger values of β.

Chapter 7

Evaporative cooling of OH

Atomic physics was revolutionized by the development of forced evaporative cooling: it led directly to the observation of Bose-Einstein condensation[4, 5], quantum-degenerate Fermi gases[86], and ultracold optical lattice simulations of condensed matter phenomena[87]. However, until the work reported in this chapter, evaporative cooling of molecules had not yet been achieved, due to unfavorable elastic-to-inelastic ratios[88] and the impractically slow thermalization rates in the available trapped species. In this chapter I report the observation of microwave-forced evaporative cooling of hydroxyl (OH) molecules loaded from a Stark-decelerated beam into an extremely high-gradient magnetic quadrupole trap. We demonstrated cooling by at least an order of magnitude in temperature and three orders in phase-space density, limited only by the low-temperature sensitivity of our spectroscopic thermometry technique. With evaporative cooling and sufficiently large initial populations, much colder temperatures are possible, and even a quantum-degenerate gas of this dipolar radical – or anything else it can sympathetically cool – may now be in reach.

7.1 Forced evaporation

Evaporative cooling of a thermal distribution[89] is, in principle, very simple: by selectively removing particles with much greater than the average total energy per particle, the temperature decreases. In the presence of elastic collisions, the high-energy tail is repopulated and so may **repeatedly** be selectively trimmed, allowing the removal of a great deal of energy at low cost in particle number. This process may be started as soon as the thermalization rate is fast enough to be practical and continued until its cooling power is balanced by the heating rate from inelastic collisions. It generally yields temperatures deep into the quantum-degenerate regime (far below the recoil limit of optical cooling), and in a few cases has reached quantum degeneracy without requiring optical pre-cooling[90, 91].

The key metric for evaporation is therefore the ratio of two timescales. The first is the rate of elastic collisions, which rethermalize the distribution, while the second is the rate at which particles are lost from the trap for reasons other than their being deliberately removed, e. g. the rates of inelastic scattering and background gas collisions. For a long time, both theoretical[92, 93, 94] and experimental work[95, 88, 96] seemed to show a generically poor value of this ratio across multiple molecular systems; this has led to a general belief that evaporative cooling is unfavorable in molecules[97]. As no trapped molecular system has achieved sufficiently rapid thermalization, there has been a lack of experiments to test this expectation—although some recent theoretical results have challenged it[98, 99].

Hydroxyl would not, at first glance, seem to be a promising candidate for evaporative cooling. Its open-shell $^2\Pi_{3/2}$ ground state and its propensity towards hydrogen bonding create a large anisotropy in the OH–OH interaction potential, which would intuitively motivate a large inelastic scattering rate. Chemical reactions are also possible, via the OH+OH$\rightarrow$H$_2$O+O pathway; it is unclear whether this reaction has an activation energy barrier[100, 101]. It is thus perhaps surprising that the elastic collision rate actually exceeds the inelastic rate, allowing evaporative cooling. However, our experimental observation is unambiguous, and is further supported by quantum scattering calculations based on the long range dipole-dipole interaction between the molecules[69, 34] considering all of the fine-structure states of the rotational ground state. This analysis considers only elastic collision or inelastic relaxation to lower energy states, as the long-range interactions appear to fully dominate over short-range effects such as chemical reactions.

In its ground state, OH has a $^2\Pi_{3/2}$ electronic character, with the lowest rotational level having total non-nuclear angular momentum $J = \frac{3}{2}$. The electronic orbital angular momentum couples to the rotational angular momentum to split the two opposite-parity states within $J = \frac{3}{2}$ by a Λ-doubling of ~ 1.667 GHz; the upper parity state is labeled $|f\rangle$ and the lower $|e\rangle$. Hydroxyl is both paramagnetic, with a molecule-fixed moment of $2\mu_B$ (μ_B is the Bohr magneton), and electrically polar with a dipole moment of 1.67 Debye (5.57×10^{-30} C·m). The Zeeman spectrum of OH is shown in Fig. 7.1a. Our magnetic trap[61] is loaded with molecules in the uppermost $|f; M_J = +\frac{3}{2}\rangle$ state, where M_J is the laboratory projection of J.

The results of our scattering calculations for $\left|f; \frac{3}{2}\right\rangle$ molecules are shown in Fig. 7.1b. The elastic cross section dominates the inelastic one for low energies: at a collision energy of $E_c = 50$ mK, the ratio of elastic over inelastic is $R = 5$ in a 50 mT magnetic field (B) and $R = 18$ in 150 mT, while at lower energy $E_c = 5$ mK the ratio increases to $R = 23$ and 137 respectively. Because the collisions occur in a quadrupole magnetic trap where B is inhomogeneous,

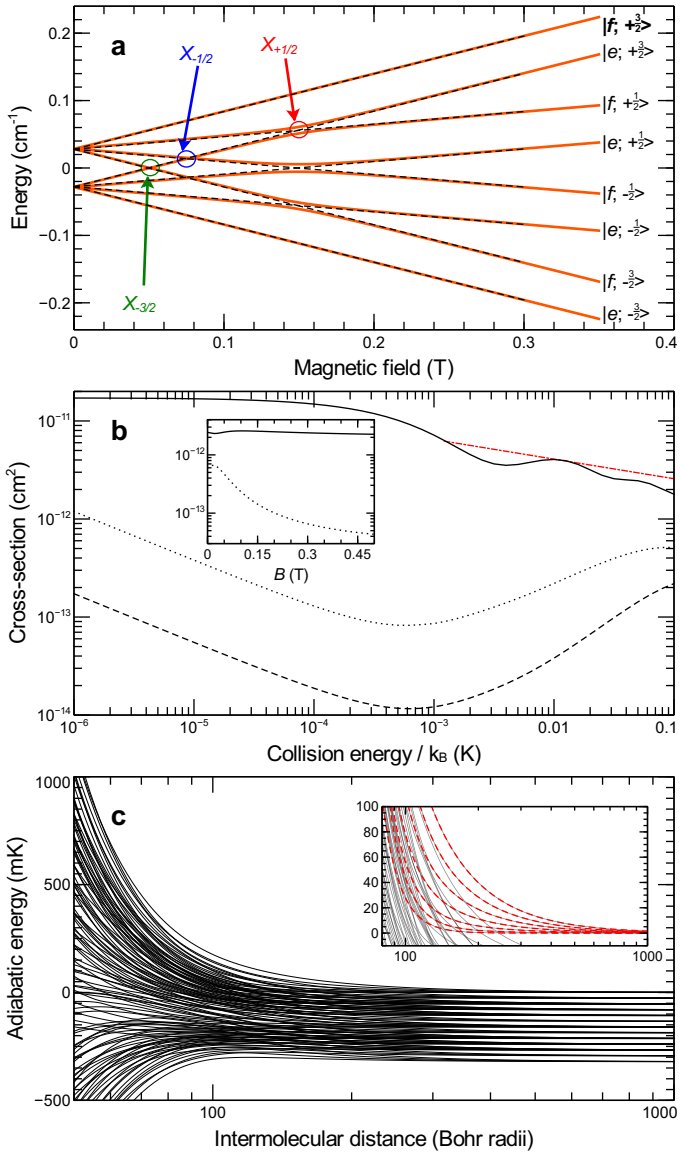

Figure 7.1: **Ground-state structure and scattering theory of OH.** (a) The ground-state Λ-doublet and Zeeman structure of OH. Dashed black lines are energy levels in the absence of any electric field. In the presence of an electric field, the level crossings become avoided (solid orange lines demonstrate a 500 V/cm field orthogonal to the magnetic field). X_i label the crossings of the $|e; \frac{3}{2}\rangle$ state with the $|f; M_J = i\rangle$ states; these crossings allow $|e; \frac{3}{2}\rangle$ molecules to escape the trap in the presence of an electric field. Molecules are loaded into the magnetic trap in the bolded $|f; \frac{3}{2}\rangle$ state. (b), Zero electric field cross sections as a function of collision energy: elastic cross section in a 50 mT magnetic field (solid), inelastic in 50 mT (dotted), and inelastic in 150 mT (dashed). The red dash-dotted line is a semi-classical expression given by Eq. (7.2). Inset: elastic (solid) and inelastic (dotted) cross sections as a function of magnetic field at $E_c = 50$ mK. (c), Adiabatic energies as a function of the inter-molecular distance at $B = 50$ mT for the $M_\ell = 0$ components of the $\ell = 2 \cdot \{0 \text{ to } 6\}$ partial waves for every combination of initial states. The inset zooms in on the repulsive van der Waals interaction for the experimentally relevant case of two colliding $|f; \frac{3}{2}\rangle$ molecules (red lines).

the inset of Fig. 7.1b shows the cross sections as a function of B at $E_c = 50\,\mathrm{mK}$. This demonstrates that inelastic processes are even further suppressed at $B > 50\,\mathrm{mT}$, in agreement with previous analysis [34].

These scattering results can be interpreted by the emergence of an effective **repulsive** van der Waals interaction between the two molecules. In zero electric field, the effective interaction in a scattering channel m can be evaluated in second-order perturbation theory by

$$V_{\mathrm{vdW}}(r) = \sum_n \frac{|\langle m|V_{dd}(r)|n\rangle|^2}{E_m - E_n} \sim \frac{C_6}{r^6}, \tag{7.1}$$

where V_{dd} is the electric dipole-dipole interaction between different scattering channels, and is non-vanishing only between molecular states of distinct parity; and E_m and E_n are the asymptotic energies of the relevant scattering channels. For the initial molecule-molecule channel of interest $\left|f;\tfrac{3}{2}\right\rangle\left|f;\tfrac{3}{2}\right\rangle$, the other fine-structure channels are lower in energy ($E_n < E_m$) and repel this energy upward. Thus, the C_6 coefficient is positive, as illustrated in Fig. 7.1c for $B = 50\,\mathrm{mT}$, for the highest energy channel. The contribution from the next rotational state $J = \frac{5}{2}$ of the $^2\Pi_{3/2}$ manifold is too high in energy ($E_m - E_{J=5/2} \approx -100\,\mathrm{K}$) to give an appreciable attractive contribution at long-range. Hence, for low collision energies, the scattering of OH molecules is dominated by the long-range interaction rather than the short-range structure of the potential surface.

Given an effective, repulsive C_6 coefficient in the incident channel, the elastic cross section can be approximated semi-classically at energies above the threshold regime[102], as

$$\sigma^{\mathrm{el}} = \frac{\pi^{11/5}\left(\Gamma(5/2)/\Gamma(3)\right)^{2/5}}{\sin(\pi/5)\,\Gamma(2/5)}\left(\frac{\bar{C}_6}{\hbar}\right)^{2/5}\left(\frac{2E_c}{m_{\mathrm{red}}}\right)^{-1/5} \tag{7.2}$$

where $m_{\mathrm{red}} = 15497$ atomic units (a. u.) is the reduced mass of two OH molecules and $\bar{C}_6 \approx 9\times10^4$ a. u. is the calculated isotropic C_6. (We contrast this $\bar{C}_6$ with values of 2–8$\times10^3$ a. u. for the alkali metal atoms[103].) Equation (7.2), plotted as a red dash-dotted line on Fig. 7.1b, only slightly overestimates the numerical results for the elastic cross section but gives a proper trend in $E_c^{-1/5}$.

We observed inelastic scattering in the presence of a large electric field (Fig. 7.2b), demonstrating the presence of two-body collisions in our trapped sample. Motivated by the prediction of a favorable R, we then undertook an experiment to implement microwave-forced evaporative cooling. The $\left|f;\tfrac{3}{2}\right\rangle \rightarrow \left|e;\tfrac{3}{2}\right\rangle$ microwave transition has a small but nonzero differential Zeeman shift[82], red-shifting by 26.6 kHz/mT. In the presence of a small electric field, $\left|e;\tfrac{3}{2}\right\rangle$ molecules can escape the trap through the avoided crossings labeled X_i in Fig. 7.1a[104], while inelastic losses

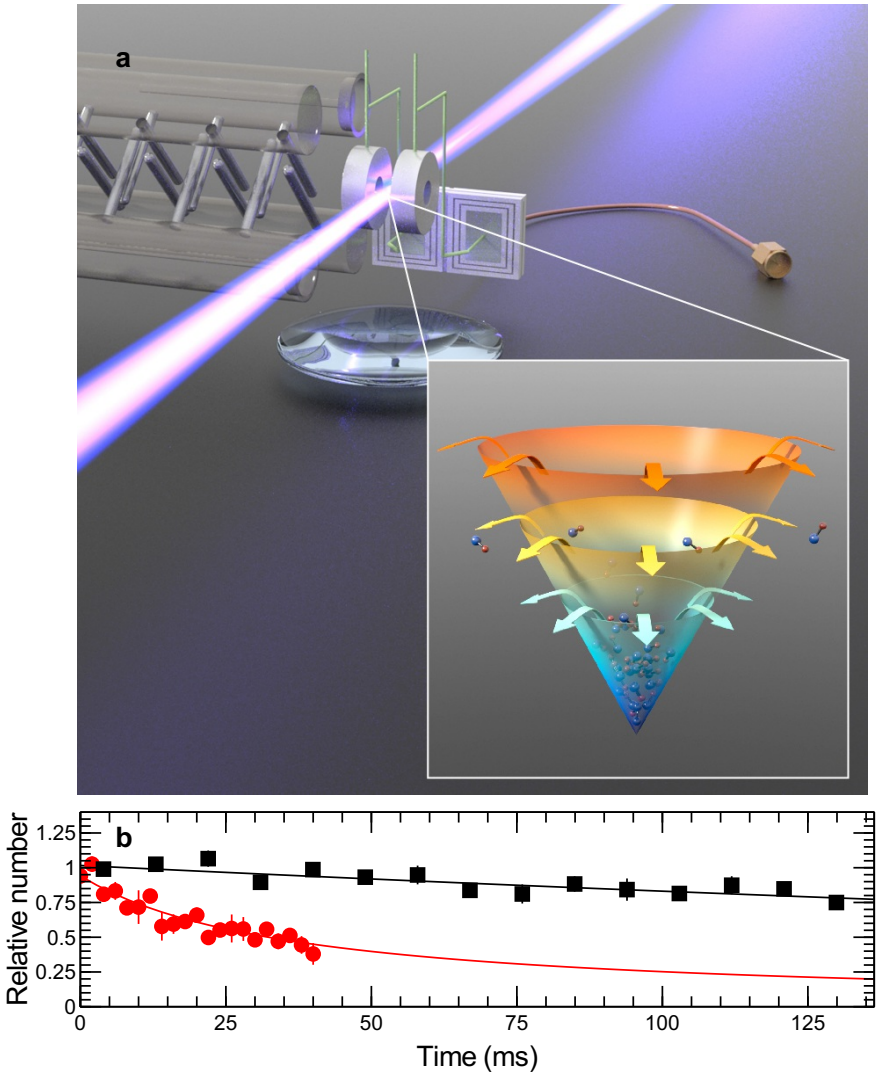

Figure 7.2: **Trap system and inelastic collisions.** (a) Schematic of the Stark decelerator[47] (left) and magnetic trap (center rings) system. The DC-blocking capacitor (rear) decouples the high voltage used for trap loading from the microwave system used for spectroscopy and evaporation, while the laser and lens provide fluorescence detection of the trapped molecules. Inset: an artist's impression of evaporative cooling. As the trap depth is successively lowered by the RF knife, the hottest molecules escape and the remainder rethermalize to a colder temperature. (b) Relative molecule number versus trap hold time, demonstrating electric field-induced collisions at 45 mK. Black squares, consistent with pure one-body loss, are with no applied electric field; red circles are well-fit by pure two-body inelastic loss induced by a large applied electric field of 3040 V/cm. (The field used in the RF knife is only 240 V/cm, for comparison.) Error bars are one standard error.

of $|f\rangle$ molecules remain unmeasurably slow. A brief microwave pulse to selectively transfer $\left|f;\frac{3}{2}\right\rangle$-state molecules to $\left|e;\frac{3}{2}\right\rangle$, followed by a longer period with an electric field present to eject $\left|e;\frac{3}{2}\right\rangle$ molecules from the trap, is therefore a field- (position-) selective method to remove molecules from the magnetic trap (see Methods). This yields what is commonly called an RF knife (Fig. 7.2a). A Zeeman depletion spectrum can be acquired by using the knife to remove molecules at a set of fixed frequencies and measuring the fractional depletion ζ; this yields a histogram of relative molecule number versus B. We fit this spectrum with a modified thermal distribution

$$\zeta(B)dB = \zeta_0 B^2 dB \times \exp[-\frac{\mu B}{k_B T}] \times \times \begin{cases} 1, & \text{if } B > 49.6 \text{ mT} \\ \exp\{-\frac{\mu[(49.6\text{ mT})-B]}{k_B T}\}, & \text{otherwise} \end{cases} \tag{7.3}$$

where ζ_0 is a fitting coefficient, $B^2 dB \propto r^2 dr$ is the volume element for a 3-D quadrupole trap, $\mu = 1.2\,\mu_B$ is the magnetic moment of the $\left|f;\frac{3}{2}\right\rangle$ state, B is the magnetic field strength implied by the microwave frequency, k_B is Boltzmann's constant, and T is the fitted temperature. The first term in the product is the simple Boltzmann expression for the molecule number as a function of B, while the second is a correction for the fact that $\left|e;\frac{3}{2}\right\rangle$ molecules only disappear when they go through one of the X_i crossings. Specifically, while molecules transferred at fields above 49.6 mT (the known location of $X_{-3/2}$) are always energetically able to reach one of the X_i crossings and thus disappear, of the molecules transferred at lower fields only those with enough kinetic energy to fly up the trap potential to $X_{-3/2}$ can escape the trap. This implies an additional Boltzmann factor $\exp[-\mu\Delta B/k_B T]$ in the probability of those molecules' disappearance.

With a B-selective technique for removing molecules, we easily implement forced evaporation by moving the edge of the RF knife from some large initial value of B towards zero, at a rate slow enough that the distribution remains in thermal equilibrium. Six different Zeeman spectra are shown in Fig. 7.3, demonstrating both forced evaporation and forced **anti**-evaporation, where for the latter the knife is held fixed at some low B_{knife} ($\mu B_{\text{knife}} < k_B T$). The trap is initially loaded with a temperature of 51 mK; left unperturbed, it free-evaporates down to 45 mK. We have forced evaporative cooling by an order of magnitude down to 5.1 mK, while forced anti-evaporation can overcome the free evaporation and increase the temperature to 54 mK. The limit of 5.1 mK is attained approximately when the RF knife edge reaches $X_{-3/2}$: while further reductions in temperature are possible, the exponential suppression of the

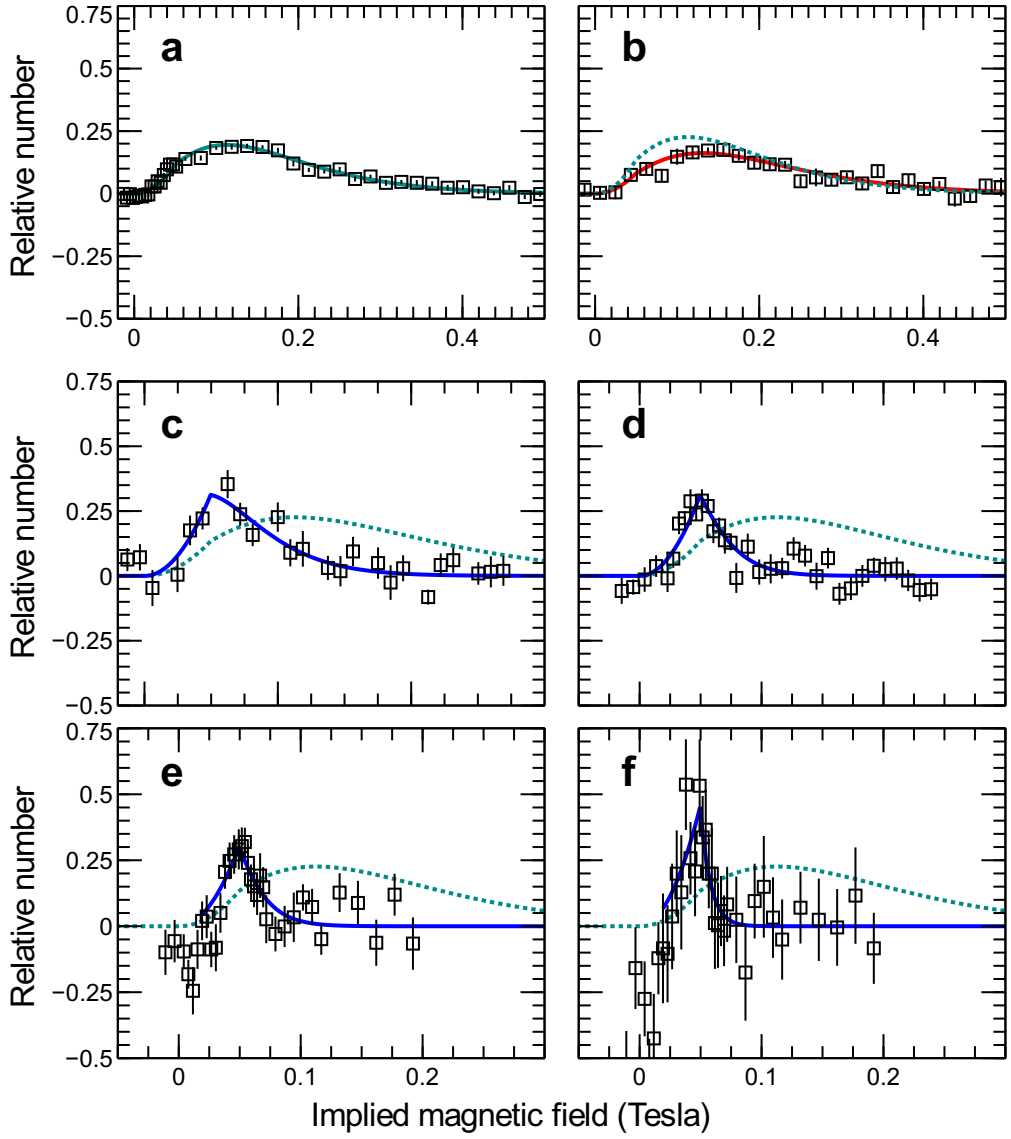

Figure 7.3: **Microwave spectra illustrating six different final temperatures.** Black squares are data (error bars are 1 standard error), and solid lines are fits to the sensitivity-corrected Boltzmann form of Eq. (7.3): (a) the unperturbed 45 mK distribution, (b) **anti**-evaporation to 54 mK, (c)**-**(f) forward evaporation to (c) 18 mK, (d) 12 mK, (e) 9.8 mK, and (f) 5.1 mK. Dotted lines reproduce the fit from **(a)**, shown for comparison. Note that the x-axis scale differs between (a)-(b) and (c)-(f); all curves have been shifted vertically to have a zero baseline.

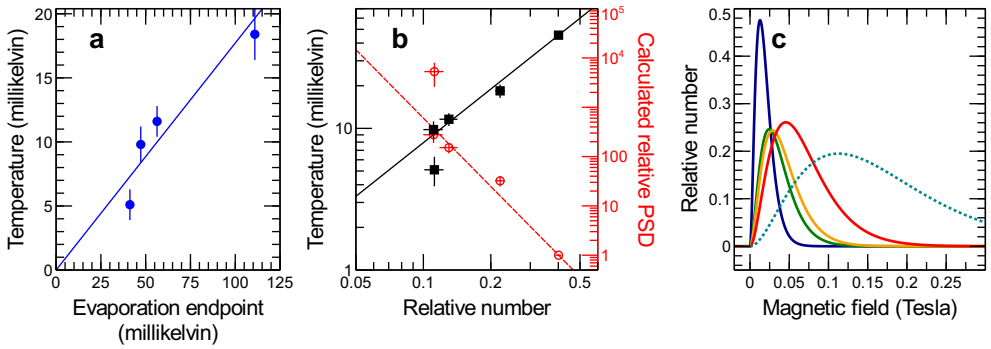

Figure 7.4: **Scaling relations observed in the evaporative cooling of OH.** (a) Final observed temperature versus effective trap depth at evaporation ramp end. (b) Final temperature (solid black, left axis) and calculated relative phase-space density (dashed red, right axis) versus remaining relative molecule number. Error bars are 1 standard error; phase space density is calculated assuming a 3-D quadrupole trap geometry. (c) Molecular Boltzmann distributions implied by the fit curves of Fig. 7.3(a) and (c)-(f) (right to left). Distributions are normalized so that the area under each curve is proportional to the total $|f\rangle$-state fluorescence observed at that temperature.

spectroscopic signal below $X_{-3/2}$ renders our current system unable to **measure** temperatures lower than this. The plots of Fig. 7.3 are all normalized so that the area under the spectroscopic curve is proportional to the total $|f\rangle$-state fluorescence signal. Thus, the increase in signal height at low B in Fig. 7.3c-f is direct evidence of increasing phase-space density.

The apparent **negative** signal in Fig. 7.3e-f can be fully fitted by assuming the presence of accumulated, trapped $|e\rangle$-state molecules in thermal equilibrium with the visible $|f\rangle$-state ones. Since $\left|e;\frac{3}{2}\right\rangle$ molecules are totally trapped if they do not have enough kinetic energy to reach $X_{-3/2}$, they will **appear**, rather than disappear, during the microwave spectroscopy and contribute to the total depletion signal with a negative sign. Fitting the curves in this fashion gives even colder temperatures of 6.8 and 3.5 mK for Figs. 7.3e and f, respectively. As the appearance of low-energy, trapped $|e\rangle$-state molecules would also constitute direct evidence of evaporation, we undertook a direct search and indeed detected them in laser-induced fluorescence.

We make several comments on the observed evaporation. The first is on the evaporation timescale: it is **fast**. In comparison to typical cooling rates of $d(\log T)/dt \sim 0.5\,\mathrm{s}^{-1}$, we cool by an order of magnitude in only 70 ms, for a rate of $33\,\mathrm{s}^{-1}$. This implies elastic collision rates on the order of 100–1000 s^{-1}, comparable to our trap frequency[104] of $\sim 1400\,\mathrm{s}^{-1}$. As we are able to set a bound on the inelastic loss rate of $< 2\,\mathrm{s}^{-1}$ (as shown in Fig. 7.2b), this implies a distribution-averaged $R \gtrsim$ 50-500, consistent with the B-field dependence of R shown in Fig. 7.1b.

We quantify the behavior of the evaporation by a set of power-law scaling relations[89], three of which are

plotted in Fig. 7.4. The average energy removed per molecule, $\eta \equiv (\text{trap depth})/k_B T$, is the first metric of interest: we observe a ratio $\eta = 5.6$, as shown in Fig. 7.4a. (For scale, η =5–10 is considered reasonable in atomic evaporation[89].) Such a relatively low value of η is unsurprising, given both the possible low (< 1000) value of the elastic-to-inelastic ratio R and the fact that molecules are only actually lost when they cross the spatial regions corresponding to the X_i crossings. This reduces the selectivity of the RF knife, as molecules transferred to the $|e\rangle$-state may recollide and rethermalize before they find their way to a crossing. The other metrics are the behavior of temperature and relative phase-space density (PSD) as function of remaining molecule number, shown in Fig. 7.4b. The efficiency of evaporation is determined by the number of molecules remaining at a given temperature and PSD, that is by $\alpha \equiv d(\log T)/d(\log N)$ and $\gamma \equiv -d(\log \text{PSD})/d(\log N)$. We measure $\alpha = 1.26$ and so using the fact that density scales as $\frac{1}{T^3}$ for our 3-D quadrupole trap we find $\gamma = 4.7$. Since R is worse at 10 mK than any other temperature down to 1 μK, linear extrapolation suggests that it would take roughly a factor of 200 reduction in number to increase PSD by 10^{10}, while the repulsive s-wave barrier would serve to stabilize the cloud.

We calculate both α and γ assuming that our fluorescence signal is linear with total molecule number, justified by the optical power broadening being larger than the Zeeman broadening of the trap. It is very difficult to determine the sensitivity of pulsed-laser-induced fluorescence *in situ*, so we use the observed collision rate to estimate a lower bound on the density in our trap: assuming a unitarity-limited scattering rate β_{u} with a maximum collisional angular momentum of $12\hbar$ (and the elastic scattering rate in Fig. 7.1b is only a factor of 3 below this value), an elastic collision rate of $\beta_{\text{u}} n_0 = 300\,\text{s}^{-1}$ implies a peak density $n_0 \approx 5 \times 10^{10}\,\text{cm}^{-3}$. (Integration of a Boltzmann distribution with this peak density over the trap suggests a total number of $\sim 10^6$ molecules in the free-evaporated trap sample and an initial peak PSD of 3×10^{-10}.) This density is high enough to permit the use of absorption imaging techniques to directly visualize the trap distribution in the future. Since imaging allows direct, non-spectroscopic measurement of both density and temperature, it will enable us to quantify further reductions in temperature. With the addition of a mechanism to prevent Majorana loss[89], the favorability of R down to microkelvin temperatures indicates that even Bose-Einstein condensation of OH may be feasible.

7.2 Methods

7.2.1 Stark deceleration and magnetic trapping

Our Stark decelerator and permanent magnet trap have been described elsewhere[47, 61] and are illustrated both in Fig. 7.2a and with more technical detail in figure 7.5. The molecular beam is formed by a supersonic expansion of a saturated mixture of water vapor in 150 kPa of krypton through a pulsed valve; a fraction of the water is cracked by a 1250 V electric discharge (seeded by a hot-cathode ionization gauge) to produce OH. The gas packet is skimmed, focused by an electrostatic hexapole, and Stark-decelerated to 34 m/s. The slowed packet is then stopped at the center of the magnetic quadrupole trap by a high-voltage field applied between the permanent magnets; turning off that field leaves the molecules with zero center-of-mass velocity and confined by the magnetic trap. The magnetic trap field is created by a pair of NdFeB permanent magnets (grade N42SH), each of which is a (4 mm ID)×(12 mm OD)×(4 mm thick) ring; this yields a maximum gradient of ~ 2 T/cm in the strongly-confining direction. The high voltage for loading the trap, the low voltage DC bias for ejecting $|e\rangle$-state molecules, and the microwave fields are all directly applied to the surface plating of the permanent magnets.

7.2.2 Detection

We observe the presence of OH molecules through pulsed-laser induced fluorescence (LIF). The molecules are excited on the $A^2\Sigma_{1/2}(v=1) \leftarrow X^2\Pi_{3/2}(v=0)$ transition at 282 nm, and subsequently decay with $\sim$70% efficiency by $A^2\Sigma_{1/2}(v=1) \rightarrow X^2\Pi_{3/2}(v=1)$ around 313 nm. This large Stokes shift enables strong rejection of the excitation light by an optical filter stack on the photomultiplier tube (PMT) detector. The fluorescence is collected in-vacuum by a single collimating lens located one focal length from the trap center, and is subsequently focused onto the PMT. Unfortunately, neither the fluorescence collection efficiency nor the laser excitation efficiency are easily calculable, so LIF yields only a relative number measurement rather than an absolute one. LIF is parity-state selective, since the upper $A^2\Sigma_{1/2}$ state does not have a parity doublet: the $|e\rangle$ and $|f\rangle$ ground states must couple to different, spectroscopically resolvable excited rotational levels.

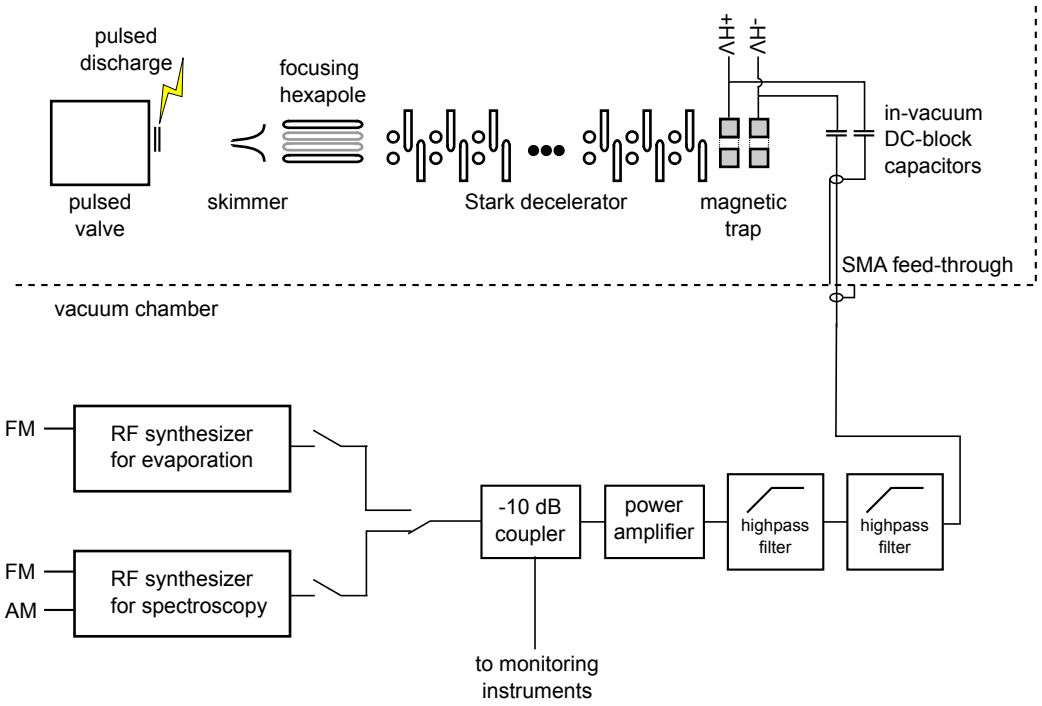

Figure 7.5: **Technical sketch of the trapping and evaporation apparatus.** The evaporation synthesizer is an SRS SG384 broadband synthesizer, chosen for its ability to perform octave-spanning frequency sweeps at rates of up to 100 Hz. The spectroscopy synthesizer is an HP 8644A.

7.2.3 Spectroscopic thermometry

In order to determine the temperature of the trapped distribution, we use a microwave depletion spectroscopy technique. A series of adiabatic rapid passage (ARP)[104] pulses are repeated over a single narrow (50-500 kHz) band to transfer Zeeman-selected molecules from $\left|f;\frac{3}{2}\right\rangle$ to $\left|e;\frac{3}{2}\right\rangle$, alternated with longer DC bias pulses (390 V/cm; $V_{\text{spectroscopy}} = 160\,\text{V}$) to eject the transferred $|e\rangle$-state molecules from the trap. The ARP pulse duration is generally 40 μs, while the DC bias pulses vary from 200 to 1000 μs over a typical 10 ms, 17-repetition sequence. Multiple ARP pulses are used to enhance the contrast of the depletion, as a single ARP with +10 dBm peak power at the vacuum feed-through (limited by the maximum acceptable power-broadening of the microwave transition) yields less than 10% peak depletion. Since the ARPs are all at a single, fixed center frequency, there is virtually no net evaporation or anti-evaporation from the repetitions; the only effect is to enhance the contrast.

In order to accumulate a full spectrum, many repetitions of the experiment are required: each instantiation involves a new packet, which is slowed, trapped, and evaporated, then spectroscopically depleted and finally detected by LIF, which destroys the sample. Each data point in the plots of Fig. 3 is an average of many repetitions of the experiment, normalized by many repetitions which omitted the spectroscopic depletion step. Specifically, the relative depletion D_{rel} is given by

$$D_{\text{rel}} = 1 - \frac{\text{molecules with depletion ON}}{\text{molecules with depletion OFF}}$$

7.2.4 Evaporation

Once trapped, the molecules are allowed to settle briefly (on the order of 5 ms) before evaporation begins. The evaporation sequence consists of alternating microwave (80 μs with 0 dBm at the vacuum feed-through) and DC bias field ($\sim$650 μs at 240 V/cm; $V_{\text{evaporation}} = 100\,\text{V}$) pulses, though in this case with no substantial frequency chirp withing any single pulse. The microwave frequency is ramped along an exponential curve towards zero trap depth, truncated at the desired final depth. The entire evaporation sequence was completed in 70 ms for all of Fig. 3c-f, so the effective ramp rate varies between the different final temperatures. An illustration of the complete evaporation and spectroscopy sequence is shown in figure 7.6.

It is common in atomic experiments to use a magnetic-dipole transition to directly couple magnetically trapped

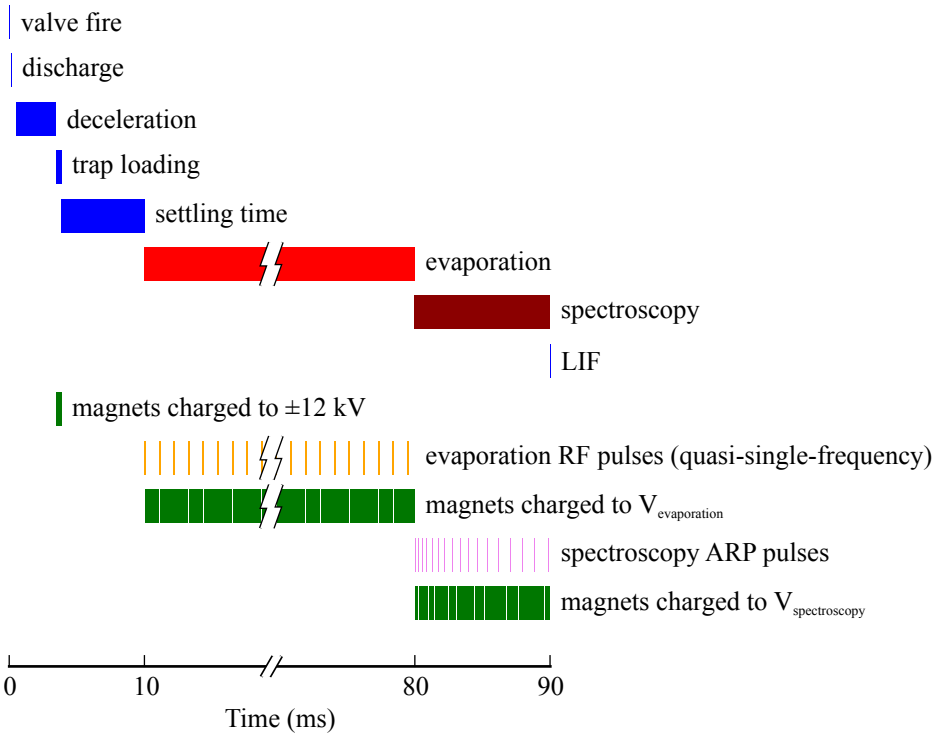

Figure 7.6: **Experimental sequence for evaporation and spectroscopic thermometry.**

states to untrapped ones, but that is not an option at the initial high temperatures in our trap. At 50 mK, hot molecules sample magnetic fields of over 300 mT, implying that the differential Zeeman shift between the $\left|f;\frac{3}{2}\right\rangle$ and the $|f;+\frac{1}{2}\rangle$ states is over 3.3 GHz as can be seen in Fig 7.1a. Since this is much larger than the Λ-doublet splitting, attempts to use drive this transition will also drive $|f\rangle \rightarrow |e\rangle$ transitions at other locations in the trap, removing the specificity of the RF knife. The $\left|f;\frac{3}{2}\right\rangle \rightarrow \left|e;\frac{3}{2}\right\rangle$ electric-dipole transition, by contrast, can be driven with low enough power as to make parasitic magnetic-dipole transitions a non-issue. Once the sample is cold enough that the RF knife has passed through $X_{+3/2}$ and the magnetic-dipole transition is far red-detuned from any electric-dipole line, it should be possible to switch to direct pumping to untrapped $|f\rangle$ states. We have not implemented this yet, due to the technical complexity of doing so.

Chapter 8

Laser cooling molecules: from off-beat dream to experimental reality

8.1 A modest proposal

When we wrote our original proposal on laser-cooling molecules with a technically reasonable number of lasers[105], the only ultracold molecules available at substantial density were RbK[106] — and four years later, that is still true! Incoherent photo-association techniques could reach the $X^1\Sigma$ ($v = 0$) ground state at 100 μK[107], but with very low densities — and did nothing to increase the chemical diversity of the available molecular species. Arbitrary species could be cooled to the kelvin regime through buffer-gas cooling[108, 109], while Stark deceleration[110, 60] reached the tens of millikelvin level for selected light molecules. However, there was no demonstrated technique to further compress and cool the lukewarm molecular clouds resulting from either technique. Cavity-mediated schemes for molecular laser cooling[111, 112, 113, 114], while in the abstract highly attractive methods for cooling a broad, chemically interesting set of molecules, even now remain unable to cool these lukewarm samples, due to the schemes' low scattering rates[113], small cavity mode volumes[112], and requirement of multiparticle collective effects[111, 114].

8.1.1 How to achieve optical cycling

Direct, free-space laser cooling and trapping would be the ideal method for producing ultracold molecules, just as it is for atoms. Unfortunately, atoms are in general much easier to laser cool than molecules, due to the latter's glaring lack of cycling transitions. Laser cooling generally requires electronic transitions, as vibrational and rotational transitions have impractically long excited state lifetimes unless a cavity is used[Andre2006]. Unfortunately, these "electronic" transitions are never purely electronic. Rather, they are rovibronic, and decay into various rotational,

vibrational, or hyperfine excited states, as well as the original ground state[115].

The branching ratios of these rovibronic decays, however, are governed by the molecular structure and the dipole selection rules. This implies that a clever choice of molecule can greatly reduce the number of possible decays. Decays into excited hyperfine states are impossible in molecules with zero nuclear spin, as these molecules have no hyperfine structure. The Franck-Condon ratios for decay back to the ground vibrational level can be quite good (99+% for selected molecules[116]). However, the only constraint on decays to rotationally excited levels is that all decays satisfy the total angular momentum selection rule $\Delta J = 0, \pm 1$[110]. Thus, even without hyperfine structure, it may take up to three lasers per vibrational level to repump the three possible rotational decays. However, if the ground state angular momentum J'' is greater than the excited state angular momentum J', two of these three decays are forbidden. In this case, the molecule **must** follow the angular momentum cycle $J'' \rightarrow J' = J'' - 1 \rightarrow J''$, and so only one laser is required per relevant vibrational level — making laser cooling of these molecules truly practical.

Thus, by combining these various transition closure criteria, we can identify a class of molecules that are exceptionally good candidates for laser cooling: they have no net nuclear spin, good Franck-Condon overlaps, and their ground or lowest metastable state has a higher angular momentum than the first accessible electronically excited state. For non-singlet molecules, the excited electronic level must also not be a Σ state, as the lack of spin-orbit splitting in Σ states means that the excited state can decay across the spin-orbit ladder.

We have identified a number of molecules that satisfy all of the above requirements. TiO and TiS are both satisfactory in their absolute ground states. Metastable FeC, ZrO, HfO, ThO, SeO, and the like are also promising[118]. We expect that some other, as-yet uncharacterized metal oxides, sulfides, and carbides should also have the necessary electronic structure. If one is willing to accept some hyperfine structure as the price of chemical diversity, some metal hydrides and metal halides may also be suitable candidates.

8.1.2 TiO

Of these candidates, we chose to focus on TiO, due to its viability in its absolute ground state and the breadth of spectroscopy and theory available in the literature[119, 120, 117, 121, 122, 123, 124, 125, 126]. A simplified level structure of TiO is shown in Fig. 8.1. The lowest ground state of TiO is the $X^3\Delta_1$, with spin-orbit constant $A^{(X^3\Delta)} = 50.61\,\mathrm{cm}^{-1}$ and rotational constant $B^{(X^3\Delta)} = 0.534\,\mathrm{cm}^{-1}$[126]. The lowest excited state is the $E^3\Pi_0$ with

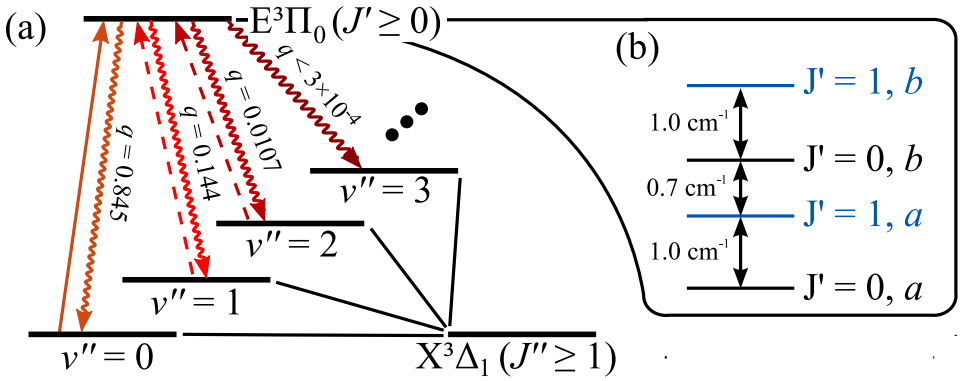

Figure 8.1: **Level structure of TiO.** (a) The electronic level structure of TiO and the transitions of interest for laser cooling. The $X^3\Delta$ ground state is split by the spin-orbit interaction into the three $X^3\Delta_{1-3}$ sublevels, of which the $X^3\Delta_1$ level is the lowest. Each sublevel contains a vibrational ladder, while each vibrational level contains a ladder of rotationally excited states (not shown). $^{48}Ti^{16}O$ has zero nuclear spin and thus there is no hyperfine structure. The ground-state $\Lambda-$doublet (not shown) is much less than the natural linewidth of the $E^3\Pi \leftarrow X^3\Delta$ transition. The solid arrow denotes the $v' = 0 \leftarrow v'' = 0$ P(1)-branch cooling laser, and the dashed arrows denote the $v' = 0 \leftarrow v'' = 1$ and $v' = 0 \leftarrow v'' = 2$ P(1)-branch repump lasers. The squiggly lines depict the dipole-allowed decays, with the associated Franck-Condon factor q[117] next to each decay. (b) The rotational and $\Lambda-$doublet structure of the $E^3\Pi_0$ electronic excited state. The states are interleaved, as the rotational splitting is smaller than the $\Lambda-$doublet splitting; a and b denote the parity states. Both the cooling and repump lasers address the $J' = 0$, a state. Not to scale.

Table 8.1: The wavelengths, Franck-Condon factors, and saturation intensities of the cooling and repump transitions of TiO.

v''	$\lambda_{0,v''}$ [nm]	Franck-Condon factor $q_{0v''}$[1]	estimated $I_{\mathrm{sat}}\,[\mu\mathrm{W/cm^2}]$[2]
0	844.7227 [121]	0.845; 0.872 [119]	8
1	923[3]	0.144	48
2	1017[c]	0.0107	645

$A^{(\mathrm{E}^3\Pi)} = 86.82\,\mathrm{cm}^{-1}$ and $B^{(\mathrm{E}^3\Pi)} = 0.515\,\mathrm{cm}^{-1}$[121]. (While the $\mathrm{d}^1\Sigma^+$ and $\mathrm{a}^1\Delta$ level are energetically below the $\mathrm{E}^3\Pi$ level, the inter-system branching ratio is expected to be very small.) As Fig. 8.1 shows, the Franck-Condon factors[117, 119] for the $\mathrm{E}^3\Pi - \mathrm{X}^3\Delta$ band are quite favorable, yielding a population leak of $3\times10^{-4}\,\mathrm{scatter}^{-1}$ (or a mean of ~ 3300 scatters before going into a dark state) with two repump lasers. The laser wavelengths, saturation intensities (I_{sat}), and Franck-Condon factors for the cooling and repump lines are summarized in Table 8.1. Note that these transitions are all accessible with diode lasers. The saturation intensities are extremely low, as the natural linewidth γ of the $\mathrm{E}^3\Pi - \mathrm{X}^3\Delta$ transition is on the order of $2\pi\times$32-40 kHz[122, 123]. This is about 5 times weaker than the intercombination line used to build a Yb magneto-optical trap (MOT) in[127]. However, with the use of a cryogenic buffer-gas-cooled TiO source (similar to [128]), the scattering rate is still large enough to work with.

8.1.3 State remixing in a $J' = J'' - 1$ MOT

The prospect of building a TiO MOT is tantalizing, given this quasi-closed transition. Traditional MOTs work using a $J' = J'' + 1$ transition and a magnetic field to break the degeneracy between the excited-state magnetic sublevels. The MOT beams are polarized so that the local orientation and strength of the quadrupole magnetic field causes the atom to preferentially scatter from the laser beam providing a position-dependent restoring force and a velocity-dependent damping force. The fact that $J' > J''$ means that the atom can always scatter from the correct beam, as shown in Fig. 8.2(a). The standard MOT will therefore not work for molecules using the aforementioned $J' = J'' - 1$ transition [Fig. 8.2(b)]. While a magnetic field can break the degeneracy of the ground-state magnetic sublevels and thus provide beam selectivity, the $|m_{J''}| = J''$ stretched states are effectively dark states, as they can only interact with one of the laser beams, not both[129].

What is needed, then, is a way to continually remix the ground-state sublevels so that all the molecules spend

some fraction of their time in bright states. Fortunately, polar molecules provide just the handle needed to accomplish this: the effective magnetic (B) and electric (E) moments of a polar molecule depend in different ways on m_J. Thus, applying a sudden (i.e. nonadiabatic) electric field orthogonal (or at least nonparallel) to the local magnetic field reprojects the total angular momentum against a new axis, randomizing m_J (and the $\Lambda-$doublet state) by coupling the two $\Lambda-$doublet manifolds together. At high remix rates and high laser saturations, the molecules' time is equally divided across the $2(2J''+1)$ ground and $2J'+1$ excited states (the factor of 2 in the ground state is due to the electrostatic mixing of the $\Lambda-$doublet), but they can only decay while they are in an excited state. Thus, while the molecules are effectively always bright, the maximum photon scattering rate is only $\frac{2J'+1}{2(2J''+1)+(2J'+1)}\gamma$. Such remixing of the ground-state magnetic sublevels allows the building of a new kind of trap, the electrostatically remixed magneto-optical trap (ER-MOT). The ER-MOT operation is shown in Fig. 8.2(b). Note that, as the local direction of the quadrupole B-field spans all of 4π steradians over the MOT volume, a single E-field pulse will be parallel to the local B-field in some region and therefore ineffective at remixing the m_J's there. This hole can, however, easily be closed by applying a second E-field pulse, nonparallel to the first. A basic ER-MOT design is shown in Fig. 8.2(c).

To build an ER-MOT with TiO, there is a minor technical complication. To leading order, the molecular magnetic moment can be written as $\mu = \mu_B m_J \left(g_L\Lambda + g_S\Sigma\right)\frac{\Omega}{J(J+1)}$ Since $g_L \approx 1$ and $g_S \approx 2$, the magnetic moment of the $X^3\Delta_1$ ($\Lambda = 2$ and $\Sigma = -1$) state is small, likely on the order of $\alpha\mu_B$, or the fine-structure constant times the Bohr magneton. In contrast, while $\Omega = 0$ in the $E^3\Pi_0$ state, the large $\Lambda-$doublet splitting indicates strong mixing with higher electronic excited states, and so by analogy with the $B^3\Pi_0$ optical Zeeman measurements of [130], we estimate the magnetic moment to be ~ 10 times that of the $X^3\Delta_1$. This, combined with the narrowness of the $E^3\Pi \leftrightarrow X^3\Delta$ transition, implies that the dynamics of a TiO ER-MOT will have more in common with narrow-line alkaline-earth MOTs [131] than normal alkali metal MOTs. Given these predicted magnetic moments, the magnetic gradient in a TiO ER-MOT must be $\lesssim 100\,\mathrm{G/cm}$. This gradient can be easily achieved with water-cooled electromagnets [60] or rare-earth permanent magnets [61]. In contrast, the large (≈ 3 Debye[125]) electric dipole moment of TiO and its extremely small ground-state $\Lambda-$doublet spacing[124] mean that electric fields of only $1\,\mathrm{V/cm}$ will give Stark shifts of about 50γ — far more than the Zeeman shift within the ER-MOT and thus sufficient to reproject m_J. These small fields can easily be switched with rise times on the order of 10 ns (a frequency of 2800γ and 56 times the Larmor frequency due to the electric field), and thus nonadiabaticity is assured.

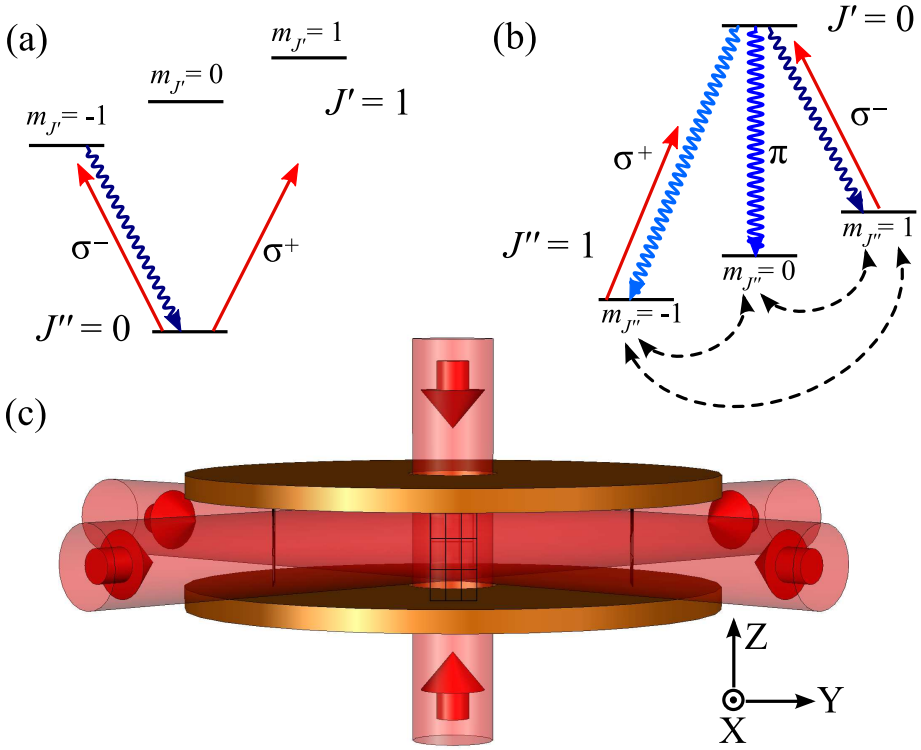

Figure 8.2: **Comparison of a traditional MOT with an ER-MOT.** (a) The level structure of a traditional MOT. The local magnetic field strength and orientation combined with the Doppler shift enhance the scattering from the laser beam that provides the damping and restoring forces and suppresses scattering from the counter-propagating beam. Since $J' > J''$, the ground state(s) are always able to scatter from every beam. (b) The level structure of the ER-MOT. The local magnetic field still governs which laser is preferentially scattered, but angular momentum conservation forbids some ground states from interacting with the preferred beam. To overcome this, the ground-state magnetic sublevel populations are remixed by pulsed electric fields, as represented by the dashed lines. (c) A sample ER-MOT design. A pair of electromagnet coils are aligned in anti-Helmholtz fashion to produce a quadrupole field. Six beams of the cooling laser are converged on the center with their polarizations oriented as usual for a MOT, but a set of four open-mesh grids are added. The grids are pulsed in pairs (e. g., first the X-axis pair and then the Y-axis pair) to produce the dipole electric fields needed to remix the magnetic sublevels. The center is also illuminated by the repump lasers (not shown).

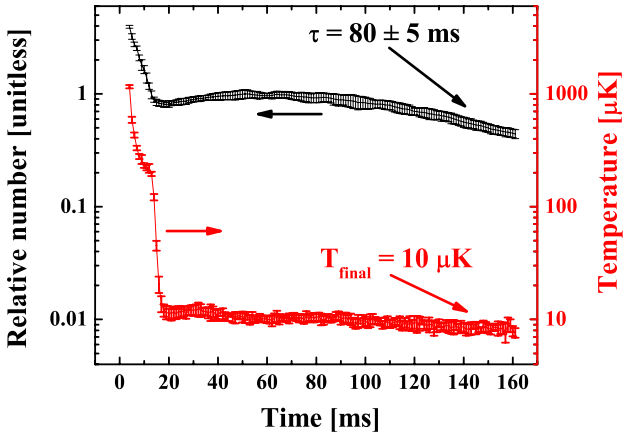

Figure 8.3: **Number (upper, black) and temperature (lower, red) time-of-flight plots for the loading of a molecular packet into a simulated TiO ER-MOT.** The initial spike on the number plot is the molecular packet flying through the ER-MOT volume; the broad hump is the actual captured molecules. The decay of the molecule number is due to radiation pumping of the captured population into excited $v'' \geq 3$ states, and yields an ER-MOT lifetime of 80 ± 5 ms. Error bars represent statistics over multiple simulation runs.

A final concern regarding the viability of the TiO ER-MOT is that either the electrostatic or magnetic fields might somehow cause population loss by mixing in rotationally excited $J' > 0$ states, which could then decay to $J'' > 1$ states and be lost. Fortunately, this loss is inhibited by the $\sim 1\,\mathrm{cm}^{-1}$ rotational splitting [Fig. 8.1(b)]. Neither the Zeeman or Stark shifts within the ER-MOT are anticipated to be larger than ~ 100 MHz, and so the perturbative probability to leave the desired $J' = 0$ state is $\left(\frac{100\,\mathrm{MHz}}{30\,\mathrm{GHz}}\right)^2 \approx 10^{-5}$. This is much smaller than the 3×10^{-4} scatter^{-1} loss rate from decays to $v'' \geq 3$ and so is of no importance.

8.1.4 Monte-Carlo simulations

To verify the feasibility of building an ER-MOT with TiO, we performed a set of 3-D semiclassical Monte-Carlo simulations. We conservatively assumed a natural linewidth of $\gamma = 2\pi \times 32$ kHz, a magnetic dipole moment of $\alpha\mu_B$, and an electric dipole moment of 3 D. We used a $1/e^2$ laser waist diameter of 6 cm. Our code treated photon scattering and molecule kinematics semiclassically and approximated the electrostatic remixing as a sudden reprojection of the diagonalized Zeeman Hamiltonian wavefunction against a new Stark + Zeeman Hamiltonian. In addition, the simulations used a set of 60 additional red-detuned frequency components (4.1γ spacing, 7.8 MHz total bandwidth) within the cooling beams to increase the capture velocity of the ER-MOT, similar to the approach used in the Yb MOT of [127]. For ease of simulation, we used a discrete molecular packet rather than a continuous source. The packet was

a 3 mm sphere initially centered at -4.2 cm on the X-axis in the coordinate system of Fig. 8.2(c). It had a flat velocity distribution of 8 ± 3.5 m/s centered in orientation around $\hat{\mathrm{x}}$, with an opening half-angle of 0.3 rad. The magnetic field gradient was 51 G/cm and the electric field was pulsed to 4 V/cm for 100 ns at a rate of 50 kHz. The cooling laser was detuned by 3.5γ to the red, with a saturation parameter of $s_{\mathrm{cool}} = 10.5$ per frequency component. The repump lasers had saturations $s_{\mathrm{repump}} = 6.1$.

These simulation parameters yield the loading and temperature curves shown in Fig. 8.3(a) and 8.3(b), respectively. The final temperature was approximately $10\,\mu$K. The ER-MOT lifetime was limited to about 80 ms by radiation pumping into vibrationally-excited dark states. The estimated capture velocity was 5.7 m/s, which when taking the rotational distribution into account allows the capture of about 0.02% of a 4.2 K thermal distribution. If one assumes a 4.2 K source flux of $10^{10}\,\mathrm{s}^{-1}$ [128], the calculated capture velocity, lifetime, and ER-MOT radius predict an ER-MOT number of 10^5 and a density of $10^9\,\mathrm{cm}^{-3}$.

In addition, we studied the importance of the electrostatic remixing to the ER-MOT operation. Figure 8.4 plots the molecule number after 160 ms against the electrostatic remix frequency Γ_{remix}. The plot clearly shows the importance of the electrostatic remixing. At $\Gamma_{\mathrm{remix}} \ll \frac{\gamma}{2\pi}$, no molecules are captured, since the molecules are optically pumped out of the bright state much faster than they are remixed back into it. For $\Gamma_{\mathrm{remix}} \lesssim \frac{\gamma}{2\pi}$ the capture efficiency rises with increasing Γ_{remix}, and then the efficiency saturates around $\Gamma_{\mathrm{remix}} = \frac{\gamma}{2\pi}$, as the molecules become evenly divided among the various ground sublevels. As additional validation checks on the simulation code, we verified that turning off the repump lasers does indeed inhibit the formation of an ER-MOT by pumping the entire population into vibrationally excited states. We also verified that we could reproduce the experimental Yb MOT of [127] by modifying the code to simulate a $J' = J'' + 1$ setup with the correct atomic parameters.

In summary, we have shown that molecules whose lowest ground- or metastable level-intersecting electronic transition has $J' = J'' - 1$ constitute good candidates for direct laser cooling. We have found several molecules that satisfy this requirement and have no hyperfine structure. We have proposed a method to use the electric dipole moment of these molecules to remove dark states in the ground and thus build an electrostatically remixed magneto-optical trap. We have validated these ideas through Monte-Carlo simulation for a specific molecule, TiO, and verified the necessity and efficacy of the electrostatic remixing.

We thank M. Yeo, E. Hudson, and D. DeMille for valuable discussions and thank NIST, DOE, and NSF for

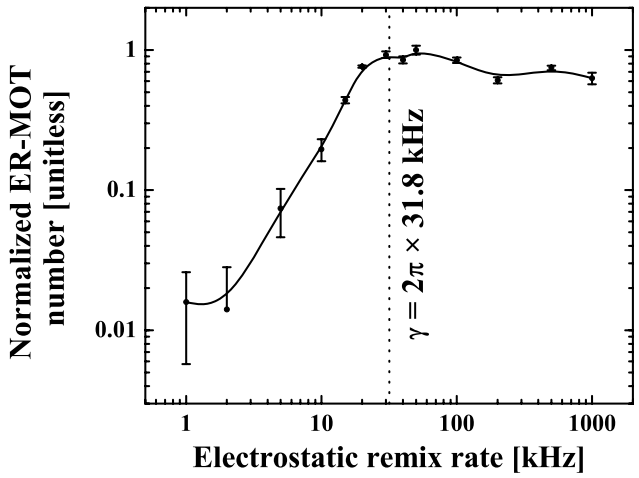

Figure 8.4: **Fractional capture vs electrostatic remix rate after 160 ms of simulation time for the TiO ER-MOT.** Error bars represent statistics over multiple simulation runs. The curve is only a guide to the eye.

support.

8.2 An experimental implementation, YO!

There are almost alwayssubstantial changes between a neat idea and its implementation; molecular laser cooling has been no exception. Instead of using TiO, we expanded and reevaluated our list of candidate molecules and chose yttrium (II) oxide (YO) instead. TiO's exceedingly narrow transition would only make the low scattering rates found in molecules (due to the large number of ground states) even worse. YO has an excited-state lifetime of only 33 ns; it also actually has superior Franck-Condon factors to TiO[132, 133, 134, 135, 136]. Only two vibrational repump lasers on $v'' = 1$ and 2 (in addition to the main cooling laser) are required to close the vibrational ladder to the order of 10^{-6}. YO is also even more polar than TiO, with a dipole moment of 4.5 D[125]. However, YO possess a small parasitic leak through its low-lying, metastable $A'^2\Delta$ level on the order of 10^{-4}.

8.2.1 An introduction to YO

The level structure of YO is shown in figure 8.5. While the proposal in the previous section achieved rotational closure through the use of an $\Omega'' > \Omega'$ electronic structure, YO follows a slightly different method. The $^2\Sigma$ ground state of YO does not have a parity doublet: every rotational level has a distinct parity. The $\left|J' = \frac{3}{2}, +\right\rangle$ excited state is then constrained against decays to $N'' \geq 3$ by angular momentum selection rules, and against decays to $N'' = 0, 2$ by parity. (This is the same scheme used in SrF[52].)

The hyperfine structure of YO is more complex than that of TiO[137, 138]. ^{16}O possesses no nuclear spin, but ^{89}Y (the only stable isotope of yttrium) has $I = \frac{1}{2}$. Since the valance, unpaired electron is in a σ orbital largely centered on the ^{89}Y nucleus, there is a strong Fermi-contact interaction of approximately 750 MHz. Since there is no spin-orbit interaction (due to the $^2\Sigma$ state) and the spin-rotation interaction is much smaller than the Fermi contact, YO has a somewhat unusual Hund's case b_β level structure. The electronic spin $\mathbf{S}$ is coupled first to $\mathbf{I}$ to yield an intermediate quantum number $\mathbf{G} = \mathbf{S} + \mathbf{I}$; $\mathbf{G}$ only then couples to the rotational angular momentum $\mathbf{N}$ to give $\mathbf{F}$. The rotational-hyperfine structure of YO is shown schematically in figure 8.5(b). Each rotational manifold N is split into a $G = 0$ singlet and $G = 1$ pseudo-triplet state. The $G = 1$ state is then slightly split into three states $F = N-1, N, N+1$; for $N'' = 1$, the $F'' = 0$ state is roughly 20 MHz above the unresolvable $F'' = 1, 2$ states.

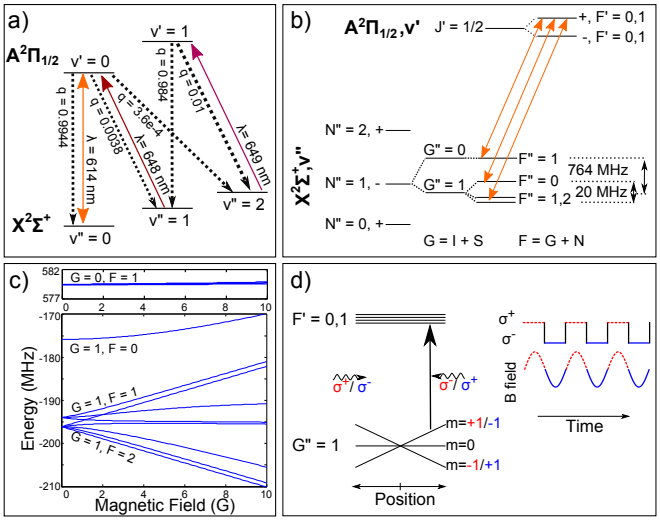

Figure 8.5: **Level structure of YO and operation of the RF-MOT.** (a) The vibronic states relevant to laser cooling, with Franck-Condon factors q listed for each relevant transition. (b) The rotational and hyperfine structure of the $X^2\Sigma$ and $A^2\Pi$ states. (c) The Zeeman spectrum of the $X^2\Sigma$ ground state. The $A^2\Pi_{1/2}$ excited state has nearly zero magnetic moment. (d) Operation of the YO RF-MOT. As the laser polarization is switched to eliminate dark states, the direction of the magnetic field must also be flipped.

The strong Fermi contact and weak spin-rotation couplings also mean that YO has a simple Zeeman structure, shown in figure 8.5(c). The singlet $G = 0$ state has almost zero magnetic moment, while the $G = 1$ state acts like a simple triplet at magnetic fields down to ~ 1 G. This structure leads to a conceptually simple MOT operation, with much smaller fields and gradients than would be required for TiO.

8.2.2 Polarization modulation and the RF-MOT

Like any molecule, a YO MOT would be a so-called Type II MOT with its cycling transition requiring $J' = J'' - 1$. Since the ground state has a higher degeneracy than the excited state, for any single laser polarization there are always two Zeeman sublevels which are not coupled to any excited state. To prevent optical pumping into these dark states from quenching the optical cycling, either the populations must be remixed between the states (e. g. electrostatically as in the TiO proposal or with a skewed magnetic field as in [139]) or the laser polarization must be varied[140]. Since the $G'' = 0, F'' = 1$ level is approximately magnetically insensitive, magnetic remixing is infeasible — as well as incompatible with the goal of a MOT. The fact that optical cycling in YO requires parity to remain a good quantum number prohibits the use of electrostatic remixing. The remaining option is then to vary the laser polarization: this is accomplished with the use of a Pockels cell (a electro-optical polarization modulator) switched at a rate comparable to the natural linewidth. A demonstration of the importance of this polarization modulation is shown in figure 8.6.

8.2.3 Experimental apparatus

The apparatus used for this experiment is illustrated in figure 8.7(a). YO molecules were produced by laser ablation of sintered Y_2O_3 tablets with ~ 3 mJ of 532 nm light from a frequency-doubled nanosecond Nd:YAG laser. (Y_2O_3 tablets are commercially available, as the material is commonly used in optical coatings.) The ablation targets are inside a 4.5 K liquid-helium-cooled buffer-gas cell. A gas flow of ~ 6 sccm and a 3 mm cell aperture produce a molecular beam with a mean forward velocity of ~ 120 m/s and a FWHM width of 40 m/s (determined by Doppler spectroscopy), corresponding to a longitudinal temperature of ~ 3.3 K.

The molecular beam is collimated by an aperture to a transverse temperature of 25 mK before crossing the cooling lasers. The laser cooling is accomplished over a 10 cm region crossed by 11 round-trip passes of the 3 mm

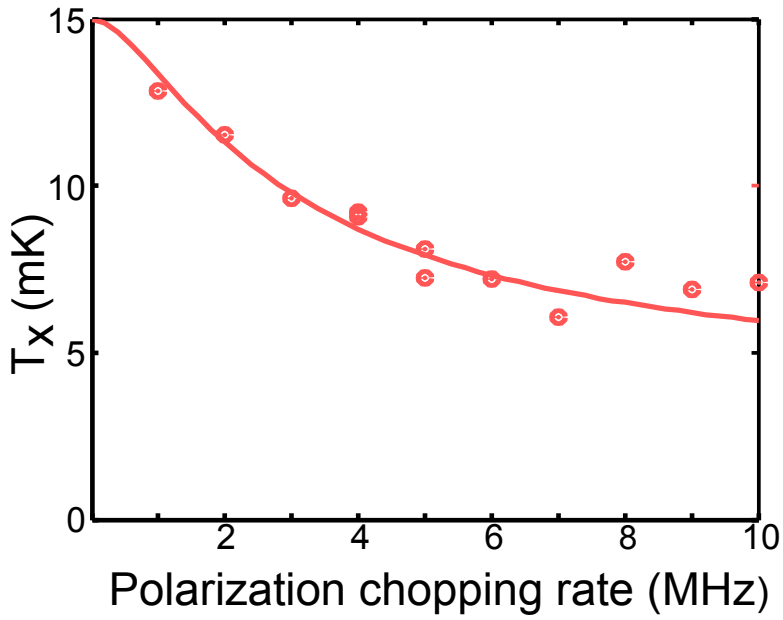

Figure 8.6: **Variation of the Doppler-cooled YO beam temperature with the polarization chopping rate.** Since the final temperature is limited purely by the number of photons scattered during the molecules' transit of the cooling region, lower temperatures directly imply higher scattering rates.

($1/e^2$ diameter) cooling beams. For 2-D Doppler cooling, a second orthogonal multipass is applied. The molecular beam is also on the axis of the magnet coil which produces the 2-D quadrupole field used for magneto-optical trapping. After the cooling region, the beam is allowed to ballistically expand over a 30 cm free-flight region. It then passes through a "clean-up" laser multipass, which optically pumps the molecules in $v'' = 1$ and 2 back into $v'' = 0$ before the molecular beam is illuminated by a single retro-reflected probe beam and imaged in fluorescence by a CCD camera.

Optical cycling in YO requires six laser frequencies, produced by three lasers and three acousto-optical modulators (AOMs). While the details of the laser system are out of the scope of this thesis (and will be in the thesis of Mark Yeo), a schematic of the system is shown in figure 8.7(b). The cooling light at 613.7 nm is produced by a dye laser, pumped by a frequency-doubled, diode-pumped Nd:YAG laser. The repump colors at 648 and 649 nm are produced by two identical diode laser systems. In each system, a grating-stabilized master oscillator injection-locks a high-power diode to produce one hyperfine component. A few milliwatts of the amplified light is frequency-shifted by an AOM and used to injection-lock a second high-power diode. The two hyperfine components of each repump are combined on a polarizing beam splitter; the two repump colors are then combined on a non-polarizing beamsplitter. Both of the combined repump beams are used: one is combined with the cooling light on a dichroic mirror, while the other becomes the clean-up beam. The dye laser and the two master diodes are frequency-stabilized through direct optical heterodyne beats with a frequency-doubled, self-referenced, octave-spanning Er:fiber frequency comb.

8.2.4 Doppler cooling

The first major experiment of the YO system was 1-D Doppler cooling. The small spacings between the $|G'' = 1, F'' = 0, 1, 2\rangle$ states lead to spectral confusion and complex dependence of the cooling rate on the laser detunings. Some typical results from the Doppler cooling experiment are shown in figure 8.8(a). Each curve shows the transverse (parallel to the cooling laser beams) spatial distribution of the YO beam after the free-flight region for a distinct set of laser parameters. The black curve (i) shows the initial, unperturbed beam with the entire cooling region dark. The green curve (ii) has the $v'' = 0$ cooling light turned on, but the $v'' = 1, 2$ repump lasers off. The cooling light efficiently optically pumps the entire beam into $v'' > 0$ over a wide band of detunings. The red (iii) and blue (iv) curves show Doppler cooling and heating, respectively. The former was taken at a detuning of $\delta = -5$ MHz, while the latter was taken with $\delta = +5$ MHz. Both curves were taken with three hyperfine components in the cooling

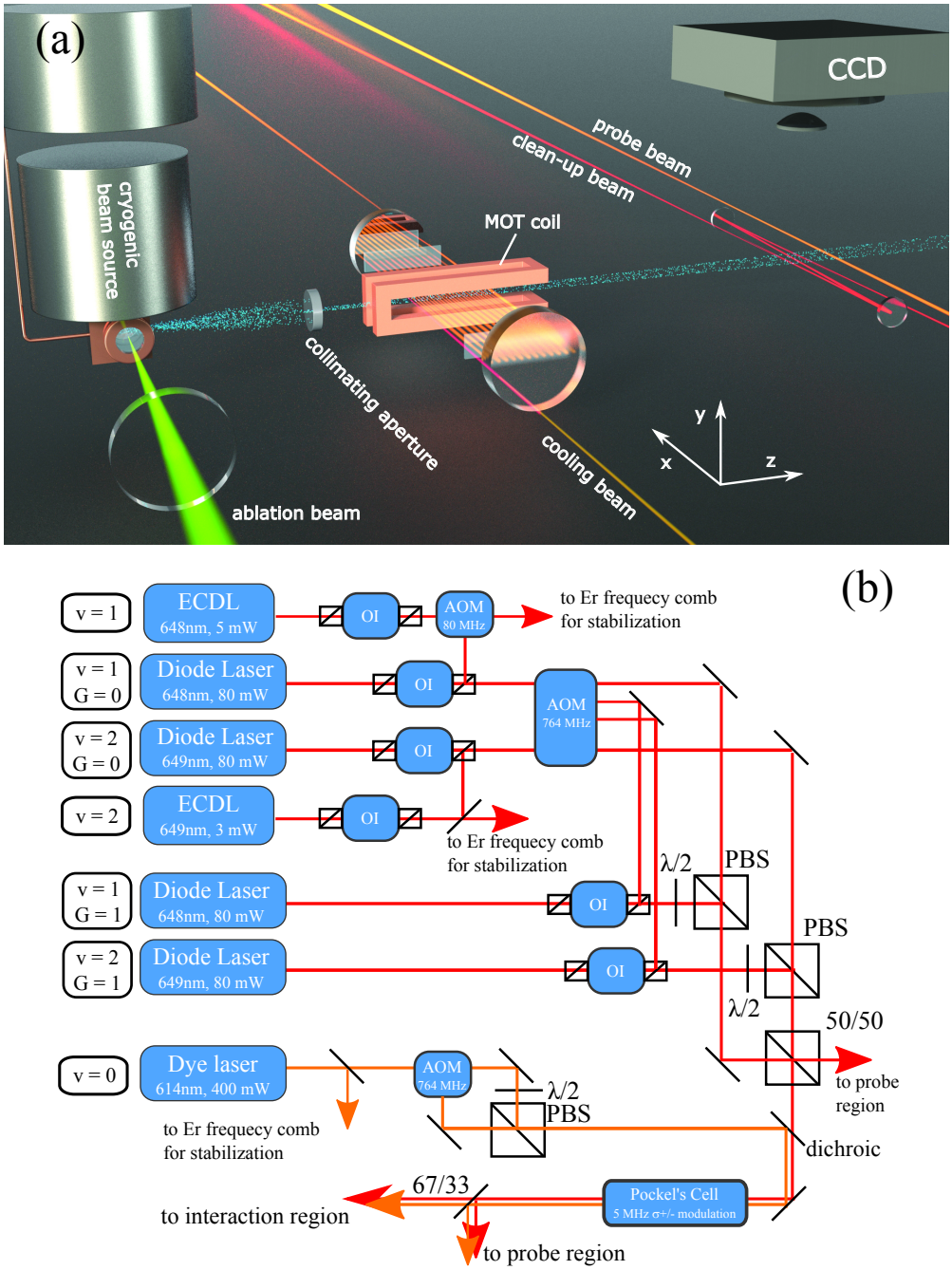

Figure 8.7: **Experimental setup for a 2-D YO MOT.** (a) A general layout of the experimental system, shown with only one dimension of cooling for clarity. YO molecules (light blue) are produced by laser ablation of sintered Y_2O_3 pellets by the green 532 nm ablation laser. The molecules are buffer-gas cooled by 4 K helium gas before escaping the buffer-gas cell (left) as a molecular beam. The beam is then collimated and passes through the MOT region inside the RF magnetic quadrupole coil (orange rectangles). The molecular beam is cooled and compressed by the multipass laser light, before being repumped out of excited vibrational states (red laser) and imaged by its resonance fluorescence in the final orange beam. (b) The laser system used to produce the 614 nm cooling light and the 648 and 649 nm repump light. The $v = 0$ cooling light is produced by a dye laser, while the $v = 1$ and 2 repumps are created using grating-stabilized external-cavity diode lasers. Each master diode injection-locks two high-power slave diodes to produce sufficient optical power in each hyperfine component. All three master oscillators are locked to a self-referenced, octave-spanning Er:fiber frequency comb.

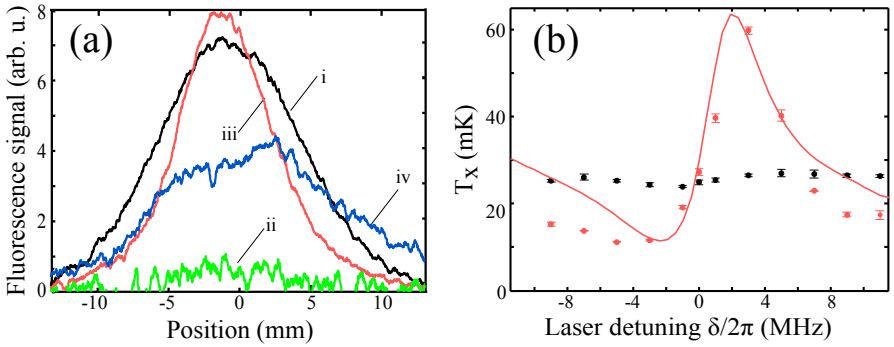

Figure 8.8: **Doppler cooling results from the YO experiment.** (a) CCD beam profiles of the YO beam for four cases: (i) the unperturbed beam, (i) the beam with only $v = 0$ light applied, which fully pumps the molecules into $v = 1$ and 2, (iii) a Doppler-heated beam, and (iv) a Doppler-cooled beam. (b) The detuning dependence of the final beam x-temperature for a uniform detuning δ of all three hyperfine components of the cooling light. The asymmetry is due to the close level spacings of the $G = 1$ manifold. Black points are the unperturbed beam temperature, as imaged using light of the give detuning and red points are Doppler-cooled or heated. The red line is a fit using a multi-state rate equation to determine the optical forces and a Monte-Carlo molecular simulation to determine the final temperature achieved.

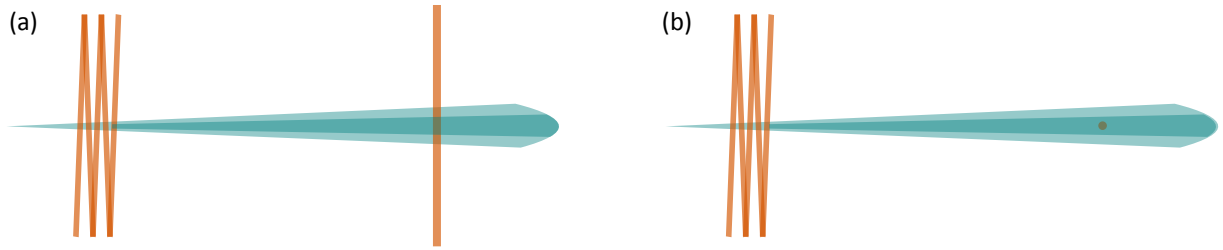

Figure 8.9: **Comparison of in- versus out-of-plane cooling.** (a) When the cooling lasers are in the same plane as the illumination for fluorescence imaging, the width of the image is reduced. (b) When the cooling lasers are transverse to the illumination, the image width does not change, but the entire image is intensified due to the increase in on-axis density from the cooling.

laser: one detuned by δ from the $|G''=0, F''=1\rangle$ line, one detuned by δ from $|G''=1, F''=0\rangle$, and one detuned by δ from the unresolved $|G''=1, F''=1,2\rangle$ manifold. A detuning (temperature-versus-δ) spectrum is shown in figure 8.8(b). The strong asymmetry is due to the fact that the gap between $|G''=1, F''=0\rangle$ and $|G''=1, F''=1,2\rangle$ is only 20 MHz. When the $|G''=1, F''=0\rangle$ laser is blue-detuned by 8 MHz from $|G''=1, F''=0\rangle$, it is also red-detuned from $|G''=1, F''=1,2\rangle$ by only 12 MHz. The red curve is a fit to a model using multi-level rate-equations to calculate the optical forces and a Monte-Carlo particle-tracking simulation to determine the resulting final temperature.

The extension from one to two-dimensional Doppler cooling is relatively simple. The laser polarization modulation retains its effectiveness in two (or, presumably, three) dimensions; the only technical change is to add a laser multipass along the second dimension. Since our imaging remains purely one-dimensional, the effectiveness of the second dimension cannot be directly judged. However, with the 2-D cooling active we observe a reduction in the one-dimensional cooling rate by a factor of two and an increase in the total (integrated) molecular number. Both of these effects are expected: the addition of the second dimension means that only half of the total photons scattered come out of the imaging dimension lasers and contribute to visible cooling, while the (invisible) cooling in the crossed dimension reduces the divergence perpendicular to the imaging direction and therefore increases the total number of molecules in the image. These effects are illustrated in figure 8.9.

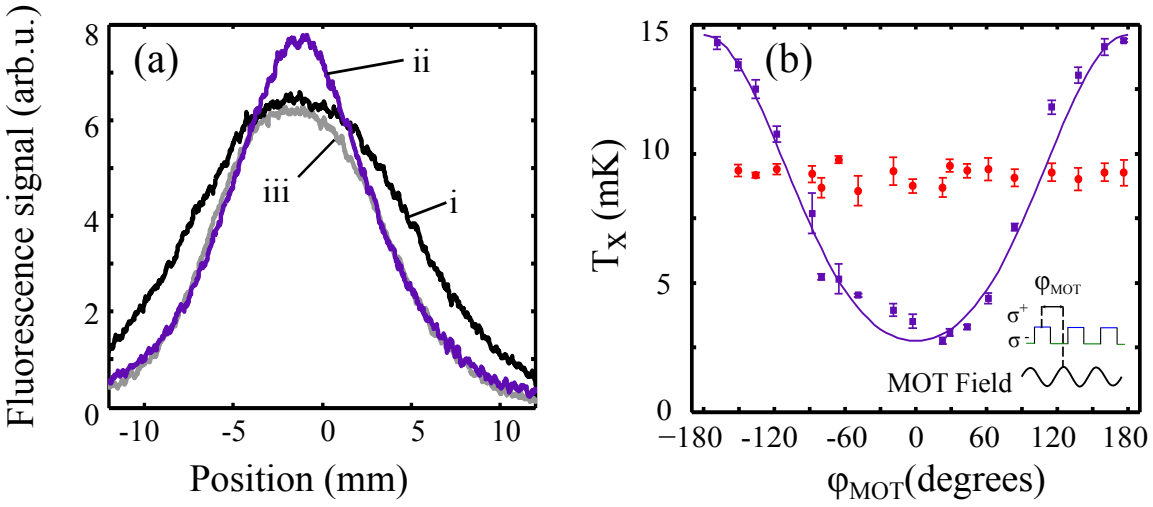

Figure 8.10: **1-D MOT results from the YO experiment.** (a) 1-D fluorescence images showing the effects of the MOT for three cases: (i) the unperturbed beam, (ii) the magnetic field in phase with the optical polarization modulation ($\varphi_{MOT} = 0°$), and (iii) the magnetic field anti-phase to the polarization modulation ($\varphi_{MOT} = 180°$). (b) The variation of the final beam temperature with φ_{MOT}. The red points are the temperature with the magnet coils turned off, and are insensitive to the absolute phase of the polarization modulation. The blue points have the magnetic field on, and demonstrate the oscillation between confining and anti-confining magneto-optical forces as φ_{MOT} varies. The solid blue curve is a pure cosinusoidal line to guide the eye.

8.2.5 Two-dimensional magneto-optical trapping

The addition of magneto-optical forces is technically non-trivial. While the use of a quadrupole magnetic field and circular laser polarization to induce a spatially-dependent scattering force is well known[3], the polarization modulation required to eliminate optical dark states complicates the picture. It has been shown that the magneto-optical force can be time-averaged, with the magnetic field direction and optical polarizations switched in unison at acoustic frequencies[141]. We, however, require the magnetic field to oscillate at radio frequencies, on the order of the transition linewidth.

To achieve magnetic field gradients on the order of 10 G/cm over a 1 cm scale, we used a "baseball" geometry 2-D quadrupole coil, illustrated in figure 8.7(a). The coil was wound using 25 turns of 350/46 gauge Litz wire (meaning 350 strands of AWG 46 wire; in Litz wire, each strand is individually insulated, and the wire is wound such that each strand spends on average the same amount of length in the center of the bundle as at the outside), so that it maintained high conductivity and current-carrying capacity at 2 MHz. The entire coil served as the inductor in an *LC*-resonator, tuned by a fixed, high-voltage RF capacitor. The resonator achieved a quality factor $Q \approx 75$. In order to achieve the ~ 1.5 A currents required to produce the requisite magnetic field gradients, 25 W of RF power were inductively coupled through a custom-wound impedance-matching transformer. These currents resulted in a peak voltage on the order of 4 kV across the coil, or about 200 V between each turn and 800 V between layers. The coil was wound as five layers of five turns each, with a coating of Q-dope (basically pure polystyrene dissolved in methyl ethyl ketone; dissolving polystyrene in acetone also works in a pinch) between layers for enhanced insulation.

The coil was wound on an aluminum form consisting of a center block matching the $\frac{3}{4} \times \frac{3}{4}$ inch inner spacing of the coil, and four more blocks in a cross pattern to create the form; the principle is that each of the four blocks can be detached and removed and then the center pulled out to extract the coil from the form. The form was sprayed with a Teflon-based mold-release agent before winding was begone. The coil was wound in a set of five layers. Each turn was tacked to the previous turns and layers using superglue (Loctite 401, activated by brushing the Litz wire with a damp Q-tip) thrice on each straight section and once on each end turn. Once a full layer was completed, it was coated with Q-dope. The cross-overs, where the wire wrapped from the outside of the previous layer to the inside of the next layer, were staggered around the coil and Q-doped both below and above the wire, since there is an 800 V potential

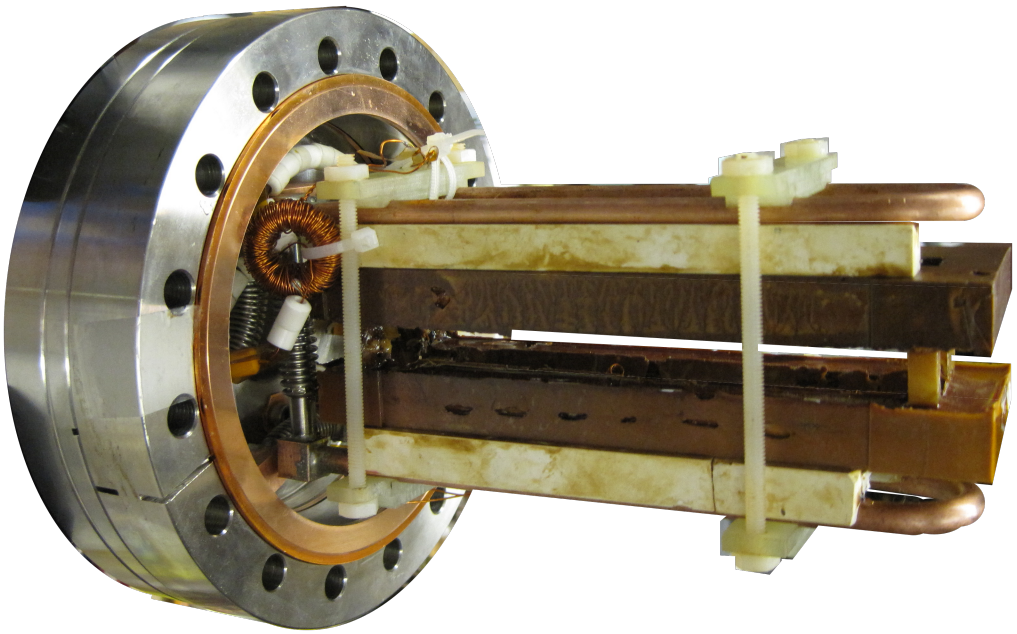

Figure 8.11: **A photograph of the completed RF magnetic quadrupole coil.** The large brown bars are the coil itself, embedded within its epoxy potting. The copper U-loops above and below the coil provide water cooling; the spacers between the U-loops and the coil are thermally conductive boron nitride. The toroidal coupling transformer can be seen near the upper-lefthand side of the coil, against the flange.

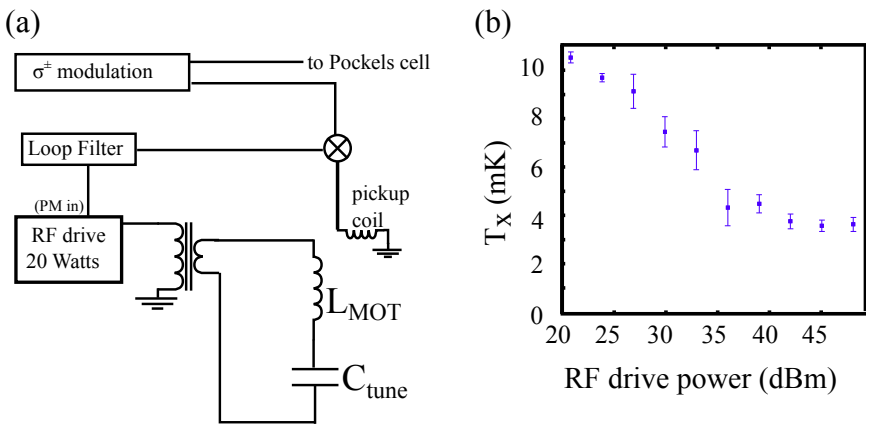

Figure 8.12: **Circuit used for stabilization of the YO MOT magnetic field phase.** (a) The servo loop layout. (b) The variation of the final beam temperature with the RF drive power applied to the coil. The saturation may be due to thermal detuning of the coil rather than true magneto-optical effects.

difference between the innermost and outermost wires.

Once wound, the coil was potted in Epo-Tek H70E epoxy, which is both thermally conductive (0.9 W/m·K) and meets NASA low-outgassing specifications. Copper cooling water lines were attached above and below the coil, using boron nitride (BN) standoffs. BN is thermally conductive but electrically insulating, and therefore does not have eddy current losses. If the copper tubes were places closer than $\sim$0.5 in. away from the coil, a measurable drop in Q was observed, presumably due to eddy currents. The resonator (secondary) side of the transformer was also wound using Litz wire, while the 50 Ω impedance (primary) winding used standard Kapton-insulated solid copper wire. The transformer, like the coil, was mounted in-vacuum to minimize the length of the leads between it and the resonator, and to allow the use of a 50 Ω coaxial feed-through. A photo of the complete, mounted coil is shown in figure 8.11.

In use, the coil reached temperatures of 32° C, leading to thermal drifts in the resonant frequency. For simplicity, the modulation frequency (and therefore the coil drive frequency) was held fixed; instead the magnetic phase was stabilized using an in-vacuum pick-up coil to servo the relative phase of the synthesizer, as illustrated in figure 8.12.

The final temperature of the beam was almost always limited by its $\sim$800 μs interaction time with the multipass cooling beam — that is, by the total number of photons scattered, and therefore by the maximum scattering rate achieved during the cooling process. This can be seen in the temperature-versus-power plots of figure 8.13. In the pure Doppler cooling case, the temperature actually reaches a minimum as the cooling laser intensity is increased and then begins to rise. This rise is not the power-broadened Doppler temperature, but indicates that the lines were being

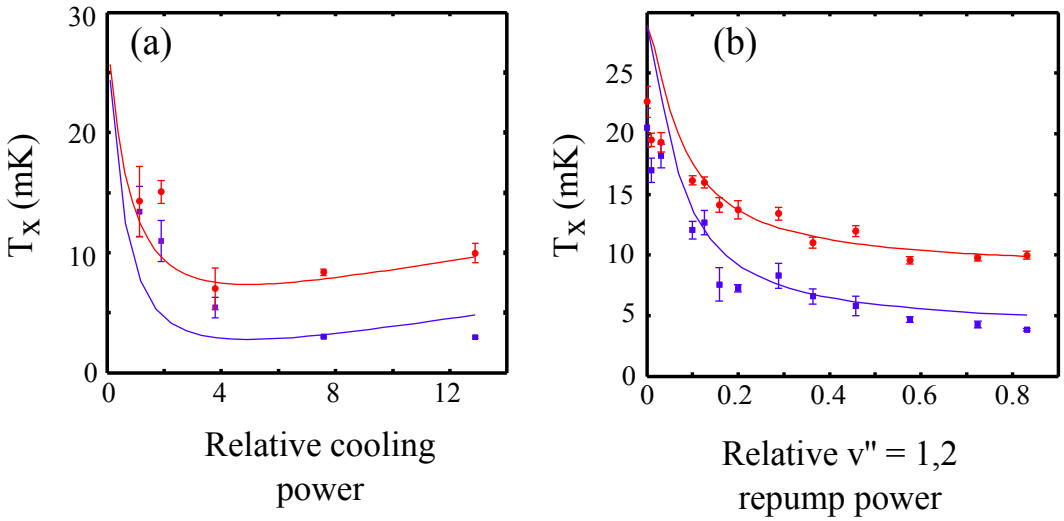

Figure 8.13: **Power dependencies of Doppler cooling and the 2-D MOT.** (a) Final temperature versus relative cooling laser (614 nm) optical intensity for Doppler cooling (red) and magneto-optical trapping (blue). (b) Final temperature versus relative repump (648 and 649 nm) laser intensity. Solid curves are fits to a multi-level rate-equation model.

sufficiently power-broadened as to produce spectral confusion in the $|G'' = 1, F''\rangle$ manifold and reduce the cooling effectiveness. This fact can be seen from the fact that in the MOT case there is no such increase in final temperature: the Zeeman-split $G'' = 1$ manifold has less spectral confusion. The importance of scattering rate is further emphasized by the continual reduction in final temperature with increasing $v'' = 1, 2$ repump power. Since less than 0.5% of the total photons scattered are from the repump lasers, their optical power contributes no direct cooling. The repump rate, however, is the major limitation on the effective time-averaged scattering rate.

These relatively low average scattering rates are entirely consistent with both the expectations of the previous section and also with the results of Shuman et al.[52]. YO possesses 12 states per vibrational level in the ground electronic configuration (two $F'' = 1$ Zeeman manifolds, and one each $F'' = 0, 2$) and 4 in the $\left|\mathrm{A}^2\Pi_{1/2}, v' = 0, F' = 0, 1\right\rangle$ levels. There are three ground vibrational levels in the total optical cycle, although the effective scattering rate is complicated by the fact that the $v'' = 2$ level is connected to the $\left|\mathrm{A}^2\Pi_{1/2}, v' = 1, F' = 0, 1\right\rangle$ level rather than $v' = 0$. If all three ground vibrational levels were connected to the same excited state, the long-term average scattering rate would saturate to

$$\frac{4}{3\times 12+4}\gamma = \frac{\gamma}{10} \approx 5\times 10^5\,\mathrm{s}^{-1}$$

, substantially lower than is typical in an atomic MOT. This result means that as a practical matter, it is worth a great deal of technical effort to maximize the scattering rate. For instance, while a 3-D MOT geometry formally does not have any dark Zeeman sublevels as there is always a transverse beam with a bright polarization component, it is still worth the effort of using an RF magnetic field and polarization modulation. In a DC MOT, the $M_G = 1$ state is always detuned by twice the local Zeeman shift of the molecule. Since an RF magnetic field swaps the $M_G = \pm 1$ states, the farthest detuned state in an RF MOT is the $M_G = 0$, with only a single power of the Zeeman shift. As scattering rate goes inversely as the square of detuning, the RF MOT will have on average a scattering rate four times higher than a DC MOT.

Chapter 9

Visions for the future

9.1 Towards a hydroxyl BEC (and maybe a Fermi gas?)

With the resounding success of evaporative cooling and its predicted applicability down to microkelvin temperatures, it seems appropriate to consider just what would be required to actually evaporate down to Bose-Einstein condensation.

9.1.1 Improved detection

The first major challenge is most certainly detection. While we have always known that LIF does not have single-molecule sensitivity, the density number implied by evaporation indicate that it is in fact spectacularly bad: probably three orders of magnitude worse than a naive estimate would suggest. If that is true, then direct absorption detection is not only possible, but should be substantially more sensitive than LIF.

9.1.2 Ballistic expansion

Continuing on the theme of detection, it should be considered just **how** one could detect the BEC state. The usual technique in atomic experiments is to turn off the trap, allow the cloud to undergo ballistic expansion, and then image its time-of-flight. The permanent magnet trap, however, would seem to render that impossible. (Since it is only the high gradient available from permanent magnets which makes evaporation possible at all, switching back to electromagnets is infeasible.)

If we cannot turn off the trap fields, can we turn off the molecules' Zeeman shift? As OH is bosonic, one natural idea is to somehow rapidly transfer the entire population to the $m_F = 0$ Zeeman level. However, in the large

magnetic fields found in our trap, the correct quantum number is J, not F. Since J is half-integer, there do not exist any states in the $X^2\Pi_{3/2}$ manifold which are field-insensitive over any substantial volume in our trap.

That is not the end of the story, however: there is also the $X^2\Pi_{1/2}$ spin-orbit-excited manifold. Since the magnetic moment for a Hund's case (a) molecule goes as $g_S\Sigma + g_L\Lambda$, the $X^2\Pi_{1/2}$ state has $g_S \cdot \frac{1}{2} + g_L \cdot (-1) \approx 0$ moment. ($g_L \approx 1$, $g_S \approx 2 + g_{\text{anom}}$ where $g_{\text{anom}} \approx 2 \times 10^{-3}$ is the anomalous part of the electron spin g-factor.) This suggests that trap-release could be accomplished by collective excitation of the entire population to this level. OH, however, is not a pure case (a) molecule: even at $J \geq \frac{3}{2}$, the $X^2\Pi_{1/2}$ manifold has substantial intermediate-case behavior[142]. Therefore, this near-zero moment exists only for the lowest $J = \frac{1}{2}$ state of the $X^2\Pi_{1/2}$ manifold. If the molecules are excited to the $\left|X^2\Pi_{1/2}, J = \frac{1}{2}, M = \frac{1}{2}\right\rangle$ level, they will have a moment of order

$$\mu = \mu_{\text{nonrotating}} \frac{M\Omega}{J(J+1)} \sim (.002\mu_B) \frac{\frac{1}{2} \cdot \frac{1}{2}}{\frac{1}{2} \cdot \frac{3}{2}} \approx 1.3\,\mu\text{K/mT}$$

which is small enough to let the expansion be quasi-ballistic over $10\,\mu$m scales at $1\,\mu$K.

How might the molecules be transferred up to the $X^2\Pi_{1/2}$ state? Using the data of Varberg and Evenson[143], we find that the $P_{12}(\frac{3}{2})$ transition is at approximately 3.786 THz (79.2 μm, 126.3 cm^{-1}) – a remarkably inconvenient wavelength, although quantum cascade lasers may be possible. If a direct light source is available, with sufficient power one could in principle use a simple adiabatic rapid passage (ARP) to transfer the entire population. However, polarization issues add a complexity: only the σ^- polarization connects the $\left|f; \frac{3}{2}\right\rangle$ trap state to the desired $\left|X^2\Pi_{1/2}, J = \frac{1}{2}, M = \frac{1}{2}\right\rangle$ excited state, and so illumination from multiple directions would be required in the context of a magnetic quadrupole trap.

Another possibility, which trades two UV light sources for one terahertz-band source, is stimulated Raman adiabatic passage (STIRAP). This technique's power and precision are well-demonstrated[51], and the long ($\sim$730 ns) lifetime of the $A^2\Sigma$ state in OH may make transfers through it feasible with low optical powers. The differential Zeeman broadening between the $^2\Pi_{3/2}$ and $^2\Pi_{1/2}$ levels may prevent the use of STIRAP, however.

A third possibility, which would use a single, high-power mid- or near-IR source would be to perform the spin-orbit transfer as part of a rovibrational transition to $v'' = 1$ or 2. The source would require a great deal of power, since the spin-orbit transition is forbidden in the $X^2\Pi_i$ ground state of OH—but it might still be easier to get a lot of power on the $v'' = 2 \leftarrow v' = 0$ vibrational overtone near 1.4 μm than a little power anywhere else. If enough power is

available, ARP could be used on this transition as well.

9.1.3 Magnetic dipole evaporation

At magnetic fields below 49.6 mT (the location of the $X_{-3/2}$ avoided crossing of chapters 5 and 7), the $\left|e;\frac{3}{2}\right\rangle$ state is totally trapped, and therefore no longer useful for evaporation. Therefore, it will be necessary to at some point cease using the electric-dipole-allowed $\left|f;\frac{3}{2}\right\rangle \rightarrow \left|e;\frac{3}{2}\right\rangle$ transition and switch to driving the magnetic-dipole $|f;M\rangle \rightarrow |f;M-1\rangle$ transitions. It is impossible to do this for magnetic field values above the location of $X_{+1/2}$: the microwave field will also be resonant with some electric-dipole-allowed transition, and will lose its magnetic field selectivity. The ideal procedure is probably to electric-dipole evaporate down to at least$\sim$90 mT below $X_{+1/2}$, so that the magnetic-dipole radiation will be detuned by O(100 MHz) from any electric-dipole transition.

Technically, there is a complication. The largest issue is that the magnetic trap has almost zero coupling for magnetic transitions: to a good approximation, the trap is a parallel-plate capacitor. The magnetic field due to the displacement current inside a circular capacitor of radius R goes as

$$B(t) = \mu_0 I(t) \frac{a}{2\pi R^2}$$

for a charging current $I(t)$ and a radial position a. Since the molecules are near the center of the magnets, they have $a \ll R$ and so see only a very small magnetic field. It will be necessary to add a coil outside the trap to couple to the magnetic transitions. Fortunately, both the steel and the NdFeB magnet material have relative permeabilities close to unity, so they should not present any screening issues. Applying the magnetic-dipole microwaves through an electrically isolated coil also removes any issues regarding high-voltage protection for the microwave system as the frequencies drop down towards DC.

9.1.4 Preventing Majorana losses

The largest issue on the path to lower temperatures is Majorana loss. Majorana loss occurs due to a loss of adiabaticity in a quadrupole trap when the molecules pass through the trap minimum. In order for the molecules to remain trapped, they must adiabatically follow the magnetic field direction, so that they remain in the magnetic weak-field-seeking state. Near the trap center, the Larmor frequency $\Omega_L = g\mu_B B' r/h$ (where g is the Lande g-factor and B'

is the magnetic field gradient) goes to zero with the the radial coordinate r. The rate of change of the magnetic field angle, however, does **not** go to zero. Since mean velocity is proportional to temperature,

$$\frac{d\theta_B}{dt} = \frac{v_\theta}{r} \sim \frac{\sqrt{T/m}}{r}$$

for particles of mass m. Therefore, there always exists some

$$r_{\text{death}} \sim \left(\frac{\sqrt{T/m}}{g\mu_B B'} \right)^{1/2}$$

for which $\Omega_L \leq \frac{d\theta_B}{dt}$; since the mean radius r_T of the cloud simply scales as T for a 3-D quadrupole trap,

$$\frac{r_{\text{death}}}{r_T} \sim T^{-3/4}$$

.

Semi-empirical scaling from atomic systems suggests that Majorana loss will become a major issue in OH around 1 mK—only a factor of 5 colder than was demonstrated in chapter 7. Therefore, it is critical to find a way to suppress this loss mechanism.

In atomic gases, the standard way to avoid Majorana loss in magnetic traps is to use a trap geometry which does not have a true magnetic field zero at its center: an Ioffe-Pritchard (IP) trap[144] or a time-orbiting potential (TOP) trap[145]. The former uses a large magnetic bias gradient to convert the linear quadrupole trap to a harmonic trap with a nonzero central magnetic field, while the latter uses an AC magnetic bias to shift the field zero of a quadrupole trap out from under the trapped atoms. If the zero describes a ring trajectory outside the trapped cloud, and does so faster than the dynamical timescale of the cloud, the cloud will remain trapped at the center since the time-averaged magnetic field is still lower there than over the trajectory of the field zero.

Both of these trap geometries work well, although the IP geometry's technical simplicity has lead to it being far more common than the TOP trap. In the context of OH, however, both traps present major technical challenges. The major issue is that the OH trap requires both immense depth, so that it can be loaded directly from the Stark decelerator, and very tight confinement—i. e. large magnetic gradients. Even with the use of permanent magnets, it appears that switching to an IP trap implies a factor of two reduction in the trap depth. Adding TOP coils to the current permanent magnet quadrupole entails on the order of 5000-10000 amp-turns of current, which present enormous thermal challenges.

There may be another option, however—at least for one to two orders of magnitude in temperature, at which point using optical dipole forces to plug the hole in the quadrupole trap becomes eminently reasonable. Since OH molecules are polar with a substantially Hund's case *a* level structure, an applied **electric** field should also preserve the molecules' spin projection. Specifically, the electric field maintains the laboratory projection M of the total angular momentum (excluding nuclear spin) $\mathbf{J}$, since the molecule will precess around the electric field vector with an (electric) Larmor frequency

$$\Omega_L^{(e)} = \frac{\mu E}{\hbar}$$

. This suggests that a homogenous DC electric field will act like the bias field in an IP trap and therefore will prevent Majorana loss.

However, there is a complication to this story: DC electric fields can also induce Landau-Zener loss, as described in section §6.2. Numerical simulations suggest that sufficiently small electric fields (a few V/cm) are safe down to $\sim 100\,\mu$K.

9.1.5 Fermionic OD?

While OH is bosonic, due to the $I_{\mathrm{H}} = \frac{1}{2}$ spin of the hydrogen's proton coupling with the unpaired valence electron, OD ($I_{\mathrm{D}} = 1$) is fermionic. OD can be made by an electric discharge through D_2O, and Stark deceleration and magnetic trapping would all proceed almost identically to OH. (There is a correction to the timing sequences required for OD's higher mass of 18 amu, but the net change needed is small, on the order of $50^\circ \times \left(\frac{18}{17} - 1\right) \approx 3^\circ$ degrees of phase angle.) The uncertainties only begin once the OD molecules are trapped. There are two questions whose theoretical investigation may be warranted before undertaking experimental efforts:

(1) What is the $|e\rangle$-to-$|f\rangle$ differential magnetic g-factor in OD? The electronic and hyperfine structure of OD have been studied experimentally[142, 146, 147], but the **differential** g-factor has not been measured in OD.

(2) What are the collisional properties of OD? Does the large change in reduced mass substantially change the elastic-to-inelastic ratio (e. g. through a shape resonance), or does the repulsive barrier continue to dominate in $\left|f;\frac{3}{2}\right\rangle\left|f;\frac{3}{2}\right\rangle$ collisions?

9.2 Enhanced 3-D magneto-optical trapping of YO, and what to do with it

9.2.1 Dark-spot trapping

While I believe that it will be possible to demonstrate a 3-D MOT of YO without closing the leak to the $A'^2\Delta$ level, such a MOT will have a very short lifetime, on the order of 1 ms, due to optical pumping through the leak into $N'' = 0, 2$. However, simply reducing the scattering rate for molecules that have already been cooled and trapped into the MOT will go a long way to improving the MOT lifetime. At a Doppler-limited temperature of 120 μK, a molecule takes on the order of 5 ms to traverse a 1 mm sphere. If that sphere is a hole in the $v = 1$ repump beam, the molecule will rapidly cease to scatter once it enters the sphere. At the most naive level, one might suppose that the molecule will scatter $\sim$200 photons every time it exits the the dark spot, i. e. that it will go dark as soon as it decays into $v = 1$, since the 200 photons will be plenty to push it back into the dark spot. If one assumes that it takes $\sim$2500 photons to scatter through the $A'^2\Delta$ level, the dark spot would extend the MOT lifetime from 1 ms to $5 \times 2500/200 \approx 62$ ms – a very substantial improvement!

9.2.2 Closing the $A'^2\Delta$ leak

The other avenue to improving the MOT lifetime is to close the leak through the $A'^2\Delta$ state[148] entirely. This can conceivably be done in at least 3 ways:

(1) Repumping out of the $N'' = 0, 2$ states through the $A'^2\Delta$ state: as a Δ state, the A' level presumably has a very small Λ-doublet – most likely on the MHz scale or smaller. If one assumes a 3 D dipole moment and a 50 MHz Λ-doublet (both likely to be conservative estimates), it only takes 33 V/cm to reach the transition into the linear Stark regime. If the goal is simply to give strength to the parity-forbidden $|A'^2\Delta, J = \frac{3}{2}, -\rangle \rightarrow |X^2\Sigma, N = 1, -\rangle$ transition, much smaller fields are possible. However, this state mixing also makes the $|A'^2\Delta, J = \frac{3}{2}, -\rangle \rightarrow |X^2\Sigma, N = 3, -\rangle$ transition allowed, which adds a requirement for a third laser.

(2) Repumping out of the $N'' = 0, 2$ states through a $X^2\Sigma$, $v > 0$ manifold: while direct microwave remixing of $|v'' = 0, N'' = 0, 2\rangle$ into $|v'' = 0, N'' = 1\rangle$ is undesirable due to the large reduction in scattering rate it entails, molecules spend little enough time in $v > 0$ that adding a bit more due to stimulated pumping between $|v'' = 0, N'' = 0, 2\rangle$ and some $|v' > 0, N' = 1\rangle$ is immaterial. The concern with this idea is acquiring light

sources – although at least a few, and possibly tens of milliwatts may be available from quantum cascade laser sources. (Repumping through $v' = 1$ requires light at near 867 cm^{-1}(11.5 μm), while the $v' = 2$ overtone transition is at a more accessible 1740 cm^{-1} (5.75 μm).) The scattering rates required are low — a mean scattering rate of only 2 kHz (and therefore in principle a $^2\Delta$ repump rate of 1 s^{-1} in a dark spot MOT) is enough to balance gravity. BaF_2 is still substantially transparent even out to 11.7 μm.

(3) Directly repumping out of the $A'^2\Delta_{3/2}, J' = \frac{3}{2}$ state before it decays: this can in principle be achieved by optical pumping to the $B^2\Sigma, N' = 0$ level with 1.6 μm light. The $B^2\Sigma$ level has a very strong propensity to decay directly to the $X^2\Sigma$ level, and has good Franck-Condon overlaps with it (95+% decay to $v'' = 0, 1, 2$). However, the 1.6 μm line has never been observed – and as an excited-to-excited transition, the spectroscopy may be quite challenging. Moreover, the preferential decay of the $B^2\Sigma$ necessarily implies that the repump line out of the $A'^2\Delta$ must be weak, and possibly **very** weak.

All three of these options have their drawbacks; the second one seems at the moment to be the best. Although it requires two lasers rather than the one needed for third option, the laser power is likely to be much easier to achieve. The laser control is also the easiest of the three: the spectroscopy can probably be done with in-cell absorption measurements, and the stabilization requirements can be met with an optical cavity. None of the three techniques offer an immediate solution to molecules which decay through the $A'^2\Delta$ to $v'' = 1+$, but if the lasers are sufficiently agile it may be possible to dither them at kilohertz rates between the repump lines for at least $v'' = 0$ and 1. Given the $\sim 90\%$ Franck-Condon overlap to $v'' = 0$ for decays from the $A'^2\Delta$, just repumping that level would give a ten-fold improvement in the number of available scatters for a total of 3×10^4.

9.2.3 Narrow-line cooling

The development of lasers addressing the A'–X transition offers another benefit: a narrow-line second-stage MOT for cooling. The estimated 15 μs lifetime of this transition gives a Doppler limit of 1.2 μK. Since the vibrational repumps contribute less than 10% of the total scatters, the repumps through the A–X transition may be used without their contributing substantial heating.

9.2.4 Collisions and evaporation?

At least thermodynamically, YO should be stable against chemical reactions: while yttrium's preferred oxidation state is +3, Y_2O_3 cannot be formed in a two-body YO–YO collision. Y_2O + O and YO_2 + Y are both energetically disfavored relative to 2YO. However, in the context of a laser-cooled MOT, the relevant issue is probably inelastic scattering rather than chemical loss. Since the MOT population is in the excited $N'' = 1$ state, it is free to collisionally de-excite, leading to the molecule going dark – and also releasing $2B \approx 0.78\,\mathrm{cm}^{-1}$ of energy. That comes out to 14 m/s, sufficient to eject the molecule from the MOT. Of course, collisions would be exciting to see in their own right, but if the ultimate goal is to reach a regime where evaporative cooling can be used to reach quantum degeneracy it is clear that the molecules must be transferred to the $N'' = 0$ level to accumulate. This may be possible using microwaves or one of the optical transfer methods of section 9.2.2; the ideal option would be to simply let decays through the A′–X transition accumulate narrow-line-cooled molecules into an optical dipole trap by applying a tiny electric field to allow decay to $N'' = 0, 2$ after scattering some hundreds of photons. However, if the MOT works well it seems likely that its density may be collision-limited even without narrow-line cooling, and so some more active accumulation method would be required. That said, a static DC electric field could be used to allow direct decays from the $A^2\Pi$ level to $N'' = 0, 2$ at any rate desired. Roughly 2 kV/cm is sufficient to enter the linear Stark regime, implying $> 25\%$ mixing of the excited-state Λ-doublet.

9.2.5 Fermionic $^{89}Y^{17}O$?

The vast majority (99.95%) of YO is bosonic, since yttrium has only one stable isotope and both ^{16}O and ^{18}O have $I = 0$. ^{17}O does exist, however. It is quite expensive, but if it is possible to resurface ablation targets rather than discard them after a single usage cycle there should be no major issues with producing an $^{89}Y^{17}O$ beam. Isotopically-enriched Y_2O_3 does not exist commercially, but combining yttrium metal with isotopically-enriched $^{17}O_2$ in a vacuum furnace should not pose any major difficulty. The larger concern actually lies with the laser system. ^{17}O has $I = \frac{5}{2}$, leading to five hyperfine levels $F'' = \frac{1}{2}, \frac{3}{2}, \frac{5}{2}, \frac{7}{2}, \frac{9}{2}$. Since the valance electron of the $^2\Sigma$ state has a low overlap with the oxygen nucleus, its Fermi contact interaction should be small. The magnetic moment of the ^{17}O nucleus is -1.8938 μ_N, and as an $I = \frac{5}{2}$ state it also possesses an electric quadrupole moment of -0.026 e-barns[149]. Without detailed structure calculations it is impossible to predict the actual hyperfine structure of $^{89}Y^{17}O$, although in the best

case it would preserve the $G'' = 0, 1$ structure of bosonic YO and only have small splittings due to the ^{17}O nucleus. Calculations of this hyperfine structure would be of great interest.

Bibliography

[1] Hänsch, T. & Schawlow, A. Cooling of gases by laser radiation. Opt. Comm. **13**, 68—69 (1975). URL http://www.sciencedirect.com/science/article/pii/0030401875901595.

[2] Wineland, D. J. & Dehmelt, H. Bull. Am. Phys. Soc. **20**, 637 (1975).

[3] Raab, E. L., Prentiss, M., Cable, A., Chu, S. & Pritchard, D. E. Trapping of neutral sodium atoms with radiation pressure. Phys. Rev. Lett. **59**, 2631–2634 (1987).

[4] Anderson, M. H., Ensher, J. R., Matthews, M. R., Wieman, C. E. & Cornell, E. A. Observation of Bose-Einstein condensation in a dilute atomic vapor. Science **269**, 198–201 (1995). URL http://www.sciencemag.org/content/269/5221/198.abstract. http://www.sciencemag.org/content/269/5221/198.full.pdf.

[5] Davis, K. B. et al. Bose-Einstein condensation in a gas of sodium atoms. Phys. Rev. Lett. **75**, 3969–3973 (1995). URL http://link.aps.org/doi/10.1103/PhysRevLett.75.3969.

[6] Regal, C. A., Greiner, M. & Jin, D. S. Observation of resonance condensation of fermionic atom pairs. Phys. Rev. Lett. **92**, 040403 (2004). URL http://link.aps.org/doi/10.1103/PhysRevLett.92.040403.

[7] Bartenstein, M. et al. Collective excitations of a degenerate gas at the BEC-BCS crossover. Phys. Rev. Lett. **92**, 203201 (2004). URL http://link.aps.org/doi/10.1103/PhysRevLett.92.203201.

[8] Perali, A., Pieri, P., Pisani, L. & Strinati, G. C. BCS-BEC crossover at finite temperature for superfluid trapped Fermi atoms. Phys. Rev. Lett. **92**, 220404 (2004). URL http://link.aps.org/doi/10.1103/PhysRevLett.92.220404.

[9] Bourdel, T. et al. Experimental study of the BEC-BCS crossover region in lithium 6. Phys. Rev. Lett. **93**, 050401 (2004). URL http://link.aps.org/doi/10.1103/PhysRevLett.93.050401.

[10] Hood, C. J., Lynn, T. W., Doherty, A. C., Parkins, A. S. & Kimble, H. J. The atom-cavity microscope: Single atoms bound in orbit by single photons. Science **287**, 1447–1453 (2000). URL http://www.sciencemag.org/content/287/5457/1447.abstract. http://www.sciencemag.org/content/287/5457/1447.full.pdf.

[11] Pinkse, P. W. H., Fischer, T., Maunz, P. & Rempe, G. Trapping an atom with single photons. Nature **404**, 365–368 (2000). URL http://dx.doi.org/10.1038/35006006.

[12] Gilbert, S. L. & Wieman, C. E. Atomic-beam measurement of parity nonconservation in cesium. Phys. Rev. A **34**, 792–803 (1986). URL http://link.aps.org/doi/10.1103/PhysRevA.34.792.

[13] Noecker, M. C., Masterson, B. P. & Wieman, C. E. Precision measurement of parity nonconservation in atomic cesium: A low-energy test of the electroweak theory. Phys. Rev. Lett. **61**, 310–313 (1988). URL http://link.aps.org/doi/10.1103/PhysRevLett.61.310.

[14] Takamoto, M., Hong, F.-L., Higashi, R. & Katori, H. An optical lattice clock. Nature **435**, 321–324 (2005). URL http://dx.doi.org/10.1038/nature03541.

[15] Hoyt, C. W. et al. Observation and absolute frequency measurements of the $^1S_0$-$^3P_0$ optical clock transition in neutral ytterbium. Phys. Rev. Lett. **95**, 083003 (2005). URL http://link.aps.org/doi/10.1103/PhysRevLett.95.083003.

[16] Taichenachev, A. V. et al. Magnetic field-induced spectroscopy of forbidden optical transitions with application to lattice-based optical atomic clocks. Phys. Rev. Lett. **96**, 083001 (2006). URL http://link.aps.org/doi/10.1103/PhysRevLett.96.083001.

[17] Ludlow, A. D. et al. Sr lattice clock at 1×10^{-16} fractional uncertainty by remote optical evaluation with a Ca clock. Science **319**, 1805–1808 (2008). URL http://www.sciencemag.org/content/319/5871/1805.abstract. http://www.sciencemag.org/content/319/5871/1805.full.pdf.

[18] Rosenband, T. et al. Frequency ratio of Al+ and Hg+ single-ion optical clocks; metrology at the 17th decimal place. Science **319**, 1808–1812 (2008). URL http://www.sciencemag.org/content/319/5871/1808.abstract. http://www.sciencemag.org/content/319/5871/1808.full.pdf.

[19] Chou, C. W., Hume, D. B., Koelemeij, J. C. J., Wineland, D. J. & Rosenband, T. Frequency comparison of two high-accuracy Al^+ optical clocks. Phys. Rev. Lett. **104**, 070802 (2010). URL http://link.aps.org/doi/10.1103/PhysRevLett.104.070802.

[20] Hudson, E. R. et al. Production of cold formaldehyde molecules for study and control of chemical reaction dynamics with hydroxyl radicals. Phys. Rev. A **73**, 063404 (2006).

[21] Wallis, A. O. G., Gardiner, S. A. & Hutson, J. M. Conical intersections in laboratory coordinates with ultracold molecules. Phys. Rev. Lett. **103**, 083201 (2009).

[22] Meyer, E. R. & Bohn, J. L. Chemical pathways in ultracold reactions of SrF molecules. Phys. Rev. A **83**, 032714 (2011).

[23] Regan, B. C., Commins, E. D., Schmidt, C. J. & DeMille, D. New limit on the electron electric dipole moment. Phys. Rev. Lett. **88**, 071805 (2002). URL http://link.aps.org/doi/10.1103/PhysRevLett.88.071805.

[24] Hudson, J. J. et al. Improved measurement of the shape of the electron. Nature **473**, 493–496 (2011).

[25] Vutha, A. C. et al. Search for the electric dipole moment of the electron with thorium monoxide. J. Phys. B **43**, 074007 (2010). URL http://stacks.iop.org/0953-4075/43/i=7/a=074007.

[26] Leanhardt, A. et al. High-resolution spectroscopy on trapped molecular ions in rotating electric fields: A new approach for measuring the electron electric dipole moment. J. Mol. Spectrosc. **270**, 1 – 25 (2011). URL http://www.sciencedirect.com/science/article/pii/S0022285211001718.

[27] Lee, C. & Ostrovskaya, E. A. Quantum computation with diatomic bits in optical lattices. Phys. Rev. A **72**, 062321 (2005).

[28] Hudson, E. R., Lewandowski, H. J., Sawyer, B. C. & Ye, J. Cold molecule spectroscopy for constraining the evolution of the fine structure constant. Phys. Rev. Lett. **96**, 143004 (2006).

[29] Lev, B. L. et al. OH hyperfine ground state: From precision measurement to molecular qubits. Phys. Rev. A **74**, 061402 (2006).

[30] Robishaw, T., Quataert, E. & Heiles, C. Extragalactic zeeman detections in OH megamasers. Astrophys. J. **680**, 981 (2008). URL http://stacks.iop.org/0004-637X/680/i=2/a=981.

[31] Diamond, P. J., Lonsdale, C. J., Lonsdale, C. J. & Smith, H. E. Global VLBI observations of the compact OH megamaser emission from III Zw 35 and IRAS 17208-0014. Astrophys. J. **511**, 178 (1999). URL http://stacks.iop.org/0004-637X/511/i=1/a=178.

[32] DeMille, D., Cahn, S. B., Murphree, D., Rahmlow, D. A. & Kozlov, M. G. Using molecules to measure nuclear spin-dependent parity violation. Phys. Rev. Lett. **100**, 023003 (2008). URL http://link.aps.org/doi/10.1103/PhysRevLett.100.023003.

[33] Bohn, J. L. Inelastic collisions of ultracold polar molecules. Phys. Rev. A **63**, 052714 (2001).

[34] Ticknor, C. & Bohn, J. L. Long-range scattering resonances in strong-field-seeking states of polar molecules. Phys. Rev. A **72**, 032717 (2005).

[35] Ticknor, C. & Bohn, J. L. Influence of magnetic fields on cold collisions of polar molecules. Phys. Rev. A **71**, 022709 (2005). URL http://link.aps.org/doi/10.1103/PhysRevA.71.022709.

[36] Santos, L., Shlyapnikov, G. V., Zoller, P. & Lewenstein, M. Bose-Einstein condensation in trapped dipolar gases. Phys. Rev. Lett. **85**, 1791–1794 (2000).

[37] Baranov, M. A., Micheli, A., Ronen, S. & Zoller, P. Bilayer superfluidity of fermionic polar molecules: Many-body effects. Phys. Rev. A **83**, 043602 (2011). URL http://link.aps.org/doi/10.1103/PhysRevA.83.043602.

[38] Kuns, K. A., Rey, A. M. & Gorshkov, A. V. d-wave superfluidity in optical lattices of ultracold polar molecules. Phys. Rev. A **84**, 063639 (2011). URL http://link.aps.org/doi/10.1103/PhysRevA.84.063639.

[39] Zinner, N. T., Wunsch, B., Pekker, D. & Wang, D.-W. BCS-BEC crossover in bilayers of cold fermionic polar molecules. Phys. Rev. A **85**, 013603 (2012). URL http://link.aps.org/doi/10.1103/PhysRevA.85.013603.

[40] Micheli, A., Brennen, G. K. & Zoller, P. A toolbox for lattice-spin models with polar molecules. Nat. Phys. **2**, 341–347 (2006).

[41] Pupillo, G. et al. Cold atoms and molecules in self-assembled dipolar lattices. Phys. Rev. Lett. **100**, 050402 (2008).

[42] Levinsen, J., Cooper, N. R. & Shlyapnikov, G. V. Topological $p_x + ip_y$ superfluid phase of fermionic polar molecules. Phys. Rev. A **84**, 013603 (2011). URL http://link.aps.org/doi/10.1103/PhysRevA.84.013603.

[43] DeMille, D. Quantum computation with trapped polar molecules. Phys. Rev. Lett. **88**, 067901 (2002).

[44] King, J. G. In Proceedings of the 13th Annual Symposium on Frequency Control, Asbury Park, 603 (U.S. Army Signal Research and Development Laboratory, Fort Monmouth, 1959).

[45] Wolfgang, R. Sci. Am. **219**, 44 (1968).

[46] Bethlem, H., Berden, G. & Meijer, G. Decelerating neutral dipolar molecules. Phys. Rev. Lett. **83**, 1558 (1999).

[47] Bochinski, J. R., Hudson, E. R., Lewandowski, H. J., Meijer, G. & Ye, J. Phase space manipulation of cold free radical OH molecules. Phys. Rev. Lett. **91**, 243001 (2003).

[48] van de Meerakker, S. Y. T., Smeets, P. H. M., Vanhaecke, N., Jongma, R. T. & Meijer, G. Deceleration and electrostatic trapping of OH radicals. Phys. Rev. Lett. **94**, 023004 (2005).

[49] Sawyer, B. C., Stuhl, B. K., Lev, B. L., Ye, J. & Hudson, E. R. Mitigation of loss within a molecular Stark decelerator. Eur. Phys. J. D **48**, 197–209 (2008).

[50] Ospelkaus, S. et al. Efficient state transfer in an ultracold dense gas of heteronuclear molecules. Nat. Phys. **4**, 622–626 (2008).

[51] Ni, K.-K. et al. A high phase-space-density gas of polar molecules. Science **322**, 231–235 (2008). URL http://www.sciencemag.org/content/322/5899/231.abstract. http://www.sciencemag.org/content/322/5899/231.full.pdf.

[52] Shuman, E. S., Barry, J. F. & DeMille, D. Laser cooling of a diatomic molecule. Nature **467**, 820 (2010).

[53] Hummon, M. T. et al. Magneto-optical trapping of diatomic molecules. ArXiv e-prints (2012). 1209.4069.

[54] Bunker, P. R. The electronic isotope shift in diatomic molecules and the partial breakdown of the Born-Oppenheimer approximation. J. Mol. Spectrosc. **28**, 422 (1968).

[55] Brown, J. M. & Carrington, A. Rotational Spectroscopy of Diatomic Molecules (Cambridge University Press, 2003).

[56] Lefebvre-Brion, H. & Field, R. W. The Spectra and Dynamics of Diatomic Molecules (Elsevier Academic Press, 2004).

[57] Veseth, L. Hund's coupling case (c) in diatomic molecules. I. Theory . J. Phys. B **6**, 1473 (1973).

[58] Lara, M., Lev, B. L. & Bohn, J. L. Loss of molecules in magneto-electrostatic traps due to nonadiabatic transitions. Phys. Rev. A **78**, 033433 (2008). URL http://link.aps.org/doi/10.1103/PhysRevA.78.033433.

[59] Brink, D. M. & Satchler, G. R. Angular momentum (Clarendon Press, Oxford, 1968), 2nd ed. edn.

[60] Sawyer, B. C. et al. Magnetoelectrostatic trapping of ground state OH molecules. Phys. Rev. Lett. **98**, 253002 (2007).

[61] Sawyer, B. C., Stuhl, B. K., Wang, D., Yeo, M. & Ye, J. Molecular beam collisions with a magnetically trapped target. Phys. Rev. Lett. **101**, 203203 (2008).

[62] van de Meerakker, S., Vanhaecke, N., van der Loo, M., Groenenboom, G. & Meijer, G. Direct measurement of the radiative lifetime of vibrationally excited OH radicals. Phys. Rev. Lett. **95**, 013003 (2005).

[63] DeMille, D., Glenn, D. & Petricka, J. Microwave traps for cold polar molecules. Eur. Phys. J. D **31**, 375–384 (2004).

[64] Hudson, E. R. Experiments on Cold Molecules Produced via Stark Deceleration. Ph.D. thesis, University of Colorado (2006).

[65] Scoles, G. (ed.) Atomic and molecular beam methods (Oxford University Press, 1988).

[66] van de Meerakker, S. Y. T., Bethlem, H. L. & Meijer, G. Taming molecular beams. Nature Physics **4**, 595 – 602 (2008).

[67] Sawyer, B. C. Cold polar molecules for novel collision experiments at low energies. Ph.D. thesis, University of Colorado (2010).

[68] van de Meerakker, S. Y. T., Vanhaecke, N. & Meijer, G. Stark deceleration and trapping of OH radicals. Annu. Rev. Phys. Chem. **57**, 159 – 190 (2006).

[69] Avdeenkov, A. V. & Bohn, J. L. Collisional dynamics of ultracold OH molecules in an electrostatic field. Phys. Rev. A **66**, 052718 (2002). URL http://link.aps.org/doi/10.1103/PhysRevA.66.052718.

[70] K&j magnetics specifications sheet (2012). URL http://www.kjmagnetics.com/specs.asp.

[71] Latham, R. (ed.) High Voltage Vacuum Insulation (Academic Press, Harcourt Brace & Company, 1995).

[72] Air liquide gas encyclopedia (2012). URL http://encyclopedia.airliquide.com/.

[73] Tscherbul, T. V., Pavlovic, Z., Sadeghpour, H. R., Côté, R. & Dalgarno, A. Collisions of trapped molecules with slow beams. Phys. Rev. A **82**, 022704 (2010). URL http://link.aps.org/doi/10.1103/PhysRevA.82.022704.

[74] Elitzur, M. Physical characteristics of astronomical masers. Rev. Mod. Phys. **54**, 1225 (1982).

[75] Guibert, J., Rieu, N. Q. & Elitzur, M. OH excitation in interstellar clouds. Astron **66**, 395–405 (1978).

[76] Hagena, O. F. Pulsed valve for supersonic nozzle experiments at cryogenic temperatures. Rev. Sci. Instrum. **62**, 2038–2039 (1991). URL http://link.aip.org/link/?RSI/62/2038/1.

[77] Patterson, D. & Doyle, J. M. Bright, guided molecular beam with hydrodynamic enhancement. J. Chem. Phys. **126**, 154307 (2007).

[78] Patterson, D., Rasmussen, J. & Doyle, J. M. Intense atomic and molecular beams via neon buffer-gas cooling. New J. Phys. **11**, 055018 (2009).

[79] Sawyer, B. C. et al. Cold heteromolecular dipolar collisions. Phys. Chem. Chem. Phys. **13**, 19059–19066 (2011).

[80] Rubbmark, J. R., Kash, M. M., Littman, M. G. & Kleppner, D. Dynamical effects at avoided level crossings: A study of the Landau-Zener effect using Rydberg atoms. Phys. Rev. A **23**, 3107–3117 (1981).

[81] Feynman, R. P., Vernon, F. L. & Hellwarth, R. W. Geometrical representation of the schrodinger equation for solving maser problems. J. Appl. Phys. **28**, 49 (1957).

[82] Lev, B. L. et al. OH hyperfine ground state: From precision measurement to molecular qubits. Phys. Rev. A **74**, 061402 (2006). URL http://link.aps.org/doi/10.1103/PhysRevA.74.061402.

[83] Vanhaecke, N., Meier, U., Andrist, M., Meier, B. H. & Merkt, F. Multistage Zeeman deceleration of hydrogen atoms. Phys. Rev. A **75**, 031402 (2007).

[84] Narevicius, E. et al. Stopping supersonic oxygen with a series of pulsed electromagnetic coils: A molecular coilgun. Phys. Rev. A **77**, 051401 (2008).

[85] Bickman, S., Hamilton, P., Jiang, Y. & DeMille, D. Preparation and detection of states with simultaneous spin alignment and selectable molecular orientation in PbO. Phys. Rev. A **80**, 023418 (2009).

[86] DeMarco, B. & Jin, D. S. Onset of Fermi degeneracy in a trapped atomic gas. Science **285**, 1703–1706 (1999). URL http://www.sciencemag.org/content/285/5434/1703.abstract. http://www.sciencemag.org/content/285/5434/1703.full.pdf.

[87] Bakr, W. S. et al. Probing the superfluid-to-Mott insulator transition at the single-atom level. Science **329**, 547–550 (2010). URL http://www.sciencemag.org/content/329/5991/547.abstract. http://www.sciencemag.org/content/329/5991/547.full.pdf.

[88] Ni, K.-K. et al. Dipolar collisions of polar molecules in the quantum regime. Nature **464**, 1324–1328 (2010).

[89] Ketterle, W. & VanDruten, N. Evaporative cooling of trapped atoms. Adv. At. Mo. Opt. Phys. **37**, 181–236 (1996).

[90] Fried, D. et al. Bose-Einstein condensation of atomic hydrogen. Physical Review Letters **81**, 3811–3814 (1998).

[91] Doret, S., Connolly, C., Ketterle, W. & Doyle, J. Buffer-gas cooled Bose-Einstein condensate. Phys. Rev. Lett. **103**, 103005 (2009).

[92] Lara, M., Bohn, J. L., Potter, D. E., Soldan, P. & Hutson, J. M. Ultracold Rb–OH collisions and prospects for sympathetic cooling. Phys. Rev. Lett. **97**, 183201 (2006).

[93] Żuchowski, P. S. & Hutson, J. M. Low-energy collisions of NH_3 and ND_3 with ultracold Rb atoms. Phys. Rev. A **79**, 062708 (2009). URL http://link.aps.org/doi/10.1103/PhysRevA.79.062708.

[94] Quéméner, G. & Julienne, P. S. Ultracold molecules under control! Chemical Reviews (in press). URL http://pubs.acs.org/doi/abs/10.1021/cr300092g. http://pubs.acs.org/doi/pdf/10.1021/cr300092g.

[95] Campbell, W. et al. Mechanism of collisional spin relaxation in $^3\Sigma$ molecules. Phys. Rev. Lett. **102**, 13003 (2009).

[96] Parazzoli, L. P., Fitch, N. J., Żuchowski, P. S., Hutson, J. M. & Lewandowski, H. J. Large effects of electric fields on atom-molecule collisions at millikelvin temperatures. Phys. Rev. Lett. **106**, 193201 (2011). URL http://link.aps.org/doi/10.1103/PhysRevLett.106.193201.

[97] Carr, L. D., DeMille, D., Krems, R. V. & Ye, J. Cold and ultracold molecules: science, technology and applications. New J. Phys. **11**, 055049 (2009). URL http://stacks.iop.org/1367-2630/11/i=5/a=055049.

[98] Janssen, L. M. C., Żuchowski, P. S., van der Avoird, A., Groenenboom, G. C. & Hutson. Cold and ultracold NH-NH collisions in magnetic fields. Phys. Rev. A **83**, 022713 (2011).

[99] Suleimanov, Y. V., Tscherbul, T. V. & Krems, R. V. Efficient method for quantum calculations of molecule-molecule scattering properties in a magnetic field. J. Chem. Phys. **137**, 024103 (2012).

[100] Atkinson, R. et al. Evaluated kinetic and photochemical data for atmospheric chemistry: Volume I - gas phase reactions of O_x, HO_x, NO_x and SO_x species. Atmos. Chem. Phys. **4**, 1461–1738 (2004). URL http://www.atmos-chem-phys.net/4/1461/2004/.

[101] Bahng, M.-K. & Macdonald, R. G. Determination of the rate constant for the $OH(X^2\Pi)$ + $OH(X^2\Pi) \rightarrow O(^3P)$ + H_2O reaction over the temperature range 293–373 K. J. Phys. Chem. A **111**, 3850–3861 (2007). URL http://pubs.acs.org/doi/abs/10.1021/jp066359c. http://pubs.acs.org/doi/pdf/10.1021/jp066359c.

[102] Child, M. S. Molecular collision theory (Dover Publications, 1996).

[103] Derevianko, A., Johnson, W. R., Safronova, M. S. & Babb, J. F. High-precision calculations of dispersion coefficients, static dipole polarizabilities, and atom-wall interaction constants for alkali-metal atoms. Phys. Rev. Lett. **82**, 3589–3592 (1999). URL http://link.aps.org/doi/10.1103/PhysRevLett.82.3589.

[104] Stuhl, B. K., Yeo, M., Sawyer, B. C., Hummon, M. T. & Ye, J. Microwave state transfer and adiabatic dynamics of magnetically trapped polar molecules. Phys. Rev. A **85**, 033427 (2012). URL http://link.aps.org/doi/10.1103/PhysRevA.85.033427.

[105] Stuhl, B. K., Sawyer, B. C., Wang, D. & Ye, J. Magneto-optical trap for polar molecules. Phys. Rev. Lett. **101**, 243002 (2008).

[106] Ni, K. K. et al. A high phase-space-density gas of polar molecules. Science **322**, 231–235 (2008).

[107] Sage, J. M., Sainis, S., Bergeman, T. & DeMille, D. Optical production of ultracold polar molecules. Phys. Rev. Lett. **94**, 203001 (2005).

[108] Weinstein, J. D., deCarvalho, R., Guillet, T., Friedrich, B. & Doyle, J. M. Magnetic trapping of calcium monohydride molecules at millikelvin temperatures. Nature **395**, 148 – 150 (1998).

[109] Campbell, W. C., Tsikata, E., Lu, H.-I., van Buuren, L. D. & Doyle, J. M. Magnetic trapping and zeeman relaxation of NH ($X^3\Sigma_-$). Phys. Rev. Lett. **98**, 213001 (2007).

[110] Bethlem, H. & Meijer, G. Production and application of translationally cold molecules. Int. Rev. Phys. Chem. **22**, 73–128 (2003).

[111] Domokos, P. & Ritsch, H. Collective cooling and self-organization of atoms in a cavity. Phys. Rev. Lett. **89**, 253003 (2002).

[112] André, A. et al. A coherent all-electrical interface between polar molecules and mesoscopic superconducting resonators. Nat. Phys. **2**, 636 – 642 (2006).

[113] Morigi, G., Pinkse, P. W. H., Kowalewski, M. & de Vivie-Riedle, R. Cavity cooling of internal molecular motion. Phys. Rev. Lett. **99**, 073001 (2007).

[114] Lev, B. L. et al. Prospects for the cavity-assisted laser cooling of molecules. Phys. Rev. A **77**, 023402 (2008).

[115] Bahns, J. T., Stwalley, W. C. & Gould, P. L. Laser cooling of molecules: A sequential scheme for rotation, translation, and vibration. J. Chem. Phys. **104**, 9689 (1996).

[116] Di Rosa, M. Laser-cooling molecules – concept, candidates, and supporting hyperfine-resolved measurements of rotational lines in the A-X(0,0) band of CaH. Eur. Phys. J. D **31**, 395–402 (2004).

[117] Hedgecock, I. M., Naulin, C. & Costes, M. Measurements of the radiative lifetimes of TiO ($A^3\Phi$, $B^3\Pi$, $C^3\Delta$, $c^1\Phi$, $f^1\Delta$, $E^3\Pi$) states. Astron. Astrophys. **304**, 667 – 677 (1995).

[118] DeMille, D. private communication (2008).

[119] Dobrodey, N. V. Radiative transitions in TiO: Ab initio oscillator strengths and lifetimes for low-lying electronic states. Astron. Astrophys. **365**, 642–655 (2001).

[120] Gustavsson, T., Amiot, C. & Verges, J. Laser-induced fluorescence and fourier transform spectroscopy of TiO: An improved description of the $^3\Delta$ ground state. J. Mol. Spectrosc. **145**, 56 – 65 (1991).

[121] Kobayashi, K., Hall, G. E., Muckerman, J. T., Sears, T. J. & Merer, A. J. The $E^3\Pi$ - $X^3\Delta$ transition of jet-cooled TiO observed in absorption. J. Mol. Spectrosc. **212**, 133 – 141 (2002).

[122] Langhoff, S. R. Theoretical study of the spectroscopy of TiO. Astrophys. J. **481**, 1007 – 1015 (1997).

[123] Lundevall, C. Lifetime measurements of the $C^3\Delta$ state of TiS and the $E^3\Pi$ state of TiO. J. Mol. Spectrosc. **191**, 93 – 97 (1998).

[124] Namiki, K., Saito, S., Robinson, J. S. & Steimle, T. C. The pure rotational spectra of TiO($X^3\Delta$) and TiN($X^2\Sigma^+$). J. Mol. Spectrosc. **191**, 176 – 182 (1998).

[125] Steimle, T. C. & Virgo, W. The permanent electric dipole moments of the $X^3\Delta$; $E^3\Pi$; $A^3\Phi$ and $B^3\Pi$ states of titanium monoxide, TiO. Chem. Phys. Lett. **381**, 30 – 36 (2003).

[126] Amiot, C., Azaroual, E. M., Luc, P. & Vetter, R. High resolution rotational analysis of the $B^3\Pi$ - $X^3\Delta$ [1,0] band of titanium monoxide. J. Chem. Phys. **102**, 4375–4381 (1995).

[127] Kuwamoto, T., Honda, K., Takahashi, Y. & Yabuzaki, T. Magneto-optical trapping of Yb atoms using an intercombination transition. Phys. Rev. A. **60**, R745 – R748 (1999).

[128] Egorov, D., Lahaye, T., Schöllkopf, W., Friedrich, B. & Doyle, J. M. Buffer-gas cooling of atomic and molecular beams. Phys. Rev. A **66**, 043401 (2002).

[129] Metcalf, H. J. & van der Straten, P. Laser Cooling and Trapping (Springer-Verlag New York, Inc., New York, USA, 1999).

[130] Virgo, W., Steimle, T. C. & Brown, J. M. Optical Zeeman spectroscopy of the (0, 0) bands of the B $^3\Pi$-X $^3\Delta$ and A $^3\Phi$-X $^3\Delta$ transitions of titanium monoxide, TiO. Astrophys. J. **628**, 567–573 (2005).

[131] Mukaiyama, T., Katori, H., Ido, T., Li, Y. & Kuwata-Gonokami, M. Recoil-limited laser cooling of ^{87}Sr atoms near the Fermi temperature. Phys. Rev. Lett. **90**, 113002 (2003). URL http://link.aps.org/doi/10.1103/PhysRevLett.90.113002.

[132] Bernard, A., R., B. & Luc, P. Fourier transform spectroscopy: extensive analysis of the $A^2\Pi \rightarrow X^2\Sigma^+$ and $B^2\Sigma^+ \rightarrow X^2\Sigma^+$ systems of yttrium oxide. Astrophys. J. **227**, 338–348 (1979).

[133] Bernard, A. & Gravina, R. Further analysis of the $B^2\Sigma^+ \rightarrow X^2\Sigma^+$ system of the YO molecule. Astrophys. J. Supp. Ser. **44**, 223–239 (1980).

[134] Bernard, A. & Gravina, R. The emission spectrum of yttrium monoxide—New rotational and vibrational results on the $A^2\Pi$-$X^2\Sigma_+$ system. Astrophys. J. Supp. Ser. **52**, 443 (1983). URL http://adsabs.harvard.edu/full/1983ApJS...52..443B.

[135] Langhoff, S. Theoretical studies of the monoxides and monosulfides of Y, Zr, and Nb. J. Chem. Phys. **89**, 2160 (1988). URL http://link.aip.org/link/?JCPSA6/89/2160/1.

[136] Steimle, T. C. & Shirley, J. E. A molecular beam-optical Stark study of the $A^2\Pi$–$X^2\Sigma$ band system of YO. J. Chem. Phys. **92**, 3292 (1990).

[137] Steimle, T. C. & Al-Ramadin, Y. Fine and hyperfine structure in the $X^2\Sigma^+$ state of gas-phase yttrium monoxide. J. Mol. Spectrosc. **122**, 103–112 (1987).

[138] Childs, W. J., Poulsen, O. & Steimle, T. C. Fine and magnetic hyperfine structure in the $A^2\Pi$ and $X^2\Sigma_+$ states of yttrium monoxide. J. Chem. Phys.1 **88**, 598 (1988).

[139] Shuman, E. S., Barry, J. F., Glenn, D. R. & DeMille, D. Radiative force from optical cycling on a diatomic molecule. Physical Review Letters **103**, 223001 (2009). URL http://link.aps.org/abstract/PRL/v103/e223001.

[140] Berkeland, D. Destabilization of dark states and optical spectroscopy in Zeeman-degenerate atomic systems. Phys. Rev. A **65**, 033413 (2002).

[141] Harvey, M. & Murray, A. J. Cold atom trap with zero residual magnetic field: The ac magneto-optical trap. Phys. Rev. Lett. **101**, 173201 (2008).

[142] Dousmanis, G. C., Sanders, T. M. & Townes, C. H. Microwave spectra of the free radicals OH and OD. Phys. Rev. **100**, 1735–1754 (1955). URL http://link.aps.org/doi/10.1103/PhysRev.100.1735.

[143] Varberg, T. D. & Evenson, K. M. The rotational spectrum of OH in the v = 0–3 levels of its ground state. J. Mol. Spectrosc. **157**, 55–67 (1993).

[144] Pritchard, D. E. Cooling neutral atoms in a magnetic trap for precision spectroscopy. Phys. Rev. Lett. **51**, 1336–1339 (1983). URL http://link.aps.org/doi/10.1103/PhysRevLett.51.1336.

[145] Petrich, W., Anderson, M. H., Ensher, J. R. & Cornell, E. A. Stable, tightly confining magnetic trap for evaporative cooling of neutral atoms. Phys. Rev. Lett. **74**, 3352–3355 (1995). URL http://link.aps.org/doi/10.1103/PhysRevLett.74.3352.

[146] Clyne, M., Coxon, J. & Fat, A. W. The $A^2\Sigma^+$-$X^2\Pi_i$ electronic band system of the OD free radical: Spectroscopic data for the 0-0 sequence, and rotational term values for $A^2\Sigma^+$ and $X^2\Pi_i$. J. Mol. Spectrosc. **46**, 146 – 170 (1973). URL http://www.sciencedirect.com/science/article/pii/0022285273900313.

[147] Coxon, J. The $A^2\Sigma^+$-$X^2\Pi_i$ system of OD: Determination of molecular constants by the direct two-state fit approach. J. Mol. Spectrosc. **58**, 1 – 28 (1975). URL http://www.sciencedirect.com/science/article/pii/0022285275901538.

[148] Simard, B., James, A. M. & Hackett, P. A. On the A'$^2\Delta$-X$^2\Sigma_+$(0,0) band of YO. J. Mol. Spectrosc. **154**, 455–457 (1992).

[149] Haynes, W. M., Bruno, T. J. & Lide, D. R. (eds.) CRC Handbook of Chemistry and Physics (Taylor & Francis, 2012-2013), 93rd edition edn. URL http://www.hbcpnetbase.com/.